Activity report of the Italian CRG beamline at the European Synchrotron Radiation Facility (ESRF)

Special issue — June 2019

Grenoble, December 2019

71 Avenue des Martyrs, Grenoble, France

Responsabile editoriale: Francesco d'Acapito
(dacapito@iom.cnr.it)

LISA

2014 - 2019

Special Issue

Report

iom
Istituto Officina
dei Materiali

LISA Report 2014-2019

F. d'Acapito[1], G. O. Lepore[1], A. Puri[1], A. Balerna[2], C. Maurizio[3], A. Minguzzi[4]

[1] CNR-IOM-OGG c/o ESRF, LISA CRG Grenoble France

[2] INFN-LNF Frascati, Italy

[3] Physics Dept. Univ. Padova, Italy

[4] Chemistry Dept. Univ. Milano, Italy

Contents

1. Technical description of the beamline 6
  1.1 General aspects 6
  1.2 Layout of the beamline 6
  1.3 X-ray Optics 7
  1.4 Overall performance 12
    1.4.1. Energy resolution 12
    1.4.2. Flux 14
    1.4.3. Beam shape and size 15
    1.4.4. Energy stability 15
    1.4.5. Noise 16
  1.5 Experimental setup 17
    1.5.1. EH1 17
    1.5.2. EH2 18
    1.5.3. Detectors 18
    1.5.4. Sample Treatment 20
    1.5.5. Surface analysis 22
    1.5.6. Beamline Control 22
2. Organization 24
  2.1 General Aspects 24
  2.2 Beamline Staff 24
3. Beamline Statistical data 27
  3.1 Use of beamtime 27
  3.2 Publications 31
4. Perspectives 34
  4.1 Crystal analyser for X-ray Emission spectroscopy 34
  4.2 Microfocus station 35
5. Selection of five highlight publications 36
6. Recommendations of the previous Beamline Review Panel 38

7. Overview of the overall scientific activity 40
  7.1 Earth and Environmental Sciences 40
    7.1.1. Earth Science 40
    7.1.2. Geomaterials 42
    7.1.3. Contaminants in environmentally sensitive matrices 43
    7.1.4. Metals in particulate matter 45
    7.1.5. Bio- Geosphere interactions 46
  7.2 Magnetism and Superconductivity 48
    7.2.1. Thin films containing magnetic elements/layers 48
    7.2.2. Magnetic nanoparticles and nanostructured materials. 50
    7.2.3. Superconducting systems 52
  7.3 Glasses 55
    7.3.1. Glasses for microelectronics 55
    7.3.2. Luminescent materials 56
    7.3.3. Bulk Chalcogenide glasses 59
  7.4 Nano-Optics 61
    7.4.1. Metal clusters in zeolite 61
    7.4.2. Doped nanoparticles. 62
  7.5 Catalysis 64
    7.5.1. Bimetallic catalysts: AuAg/Al2O3, PdCu/PVPy, CoRu/SiO2, CoPt/SiO2 64
    7.5.2. Monometallic catalysts and substrates: Ag/CeO_2, Pt/CeO_2, Pd, Au, Cu 66
    7.5.3. Oxo-clusters, nano-oxides, oxides and oxides nanowires 69
  7.6 Materials for energy conversion and storage 72
    7.6.1. Electrocatalysis for energy conversion 72
    7.6.2. Sunlight harvesting 75
    7.6.3. Thermoelectric materials 77
    7.6.4. Batteries 77
  7.7 Nanostructures for optical and magnetic applications 80
    7.7.1. Few-atom metal clusters for Er^{3+} 1.54 μm emission. 80
    7.7.2. Thermally-induced modification of nanostructures. 82

7.7.3. Nanostructures of bulk immiscible alloys for magnetoplasmonics 84

7.8 Life Sciences 86

7.8.1. Nanoparticles for biological and medical applications. 86

7.8.2. Cu complexes in aqueous solutions 87

7.8.3. Metals (Zn, Cu) interaction with water and proteins 88

8. Bibliography 90

8.1 LISA specific bibliography 90

8.2 General Bibliography 104

9. Appendix 1 105

1. Technical description of the beamline

1.1 General aspects

After the successful operation of the GILDA project during two decades, the Italian Collaborating Research Group (CRG) beamline at the European Synchrotron Radiation Facility (ESRF) has been deeply renewed. Specifically, the X-ray optical scheme has been reviewed in order to open the possibility of new experimental techniques profiting from the considerable advancements occurred in the latest years, particularly in the mirrors technology. The new beamline has been named LISA (**L**inea **I**taliana per la **S**pettroscopia di **A**ssorbimento X, italian beamline for X-ray absorption spectroscopy) and it is dedicated to X-ray Absorption Spectroscopy (XAS) and related techniques. The main goal was to realize a beamline with an intense (i.e. above 10^{10} ph/s) and small (sub-mm) beam in order to carry out XAS experiments in peculiar conditions such as highly dilute samples, high-quality low-noise transmission mode, total reflection, pump-and-probe experiments, differential-mode. Other requirements were to have a wide energy range (≈ 4-70 keV) and an easy way to switch between high resolution and high luminosity. For all that, a focalized beam exhibiting a particularly stability (spatial and temporal) for the position and the energy scale as well as a high homogeneity was necessary. The central issue has been the choice of a focalization method ensuring a-chromaticity and ease of setup; to that end the adoption of toroidal mirrors has been decided. Hereafter a description of LISA in the final version is given as well as the results of the commissioning runs with the main parameters and performance of the instrument.

1.2 Layout of the beamline

LISA consists in 3 lead hutches: the Optical Hutch (OH) containing the main optical elements, the first experimental hutch (EH1) with the instrumentation for experiments with a non-focused beam and low energy harmonic rejection mirrors and finally, the second experimental hutch (EH2) containing all the instrumentation for experiments with the focused beam (see Figure 1)

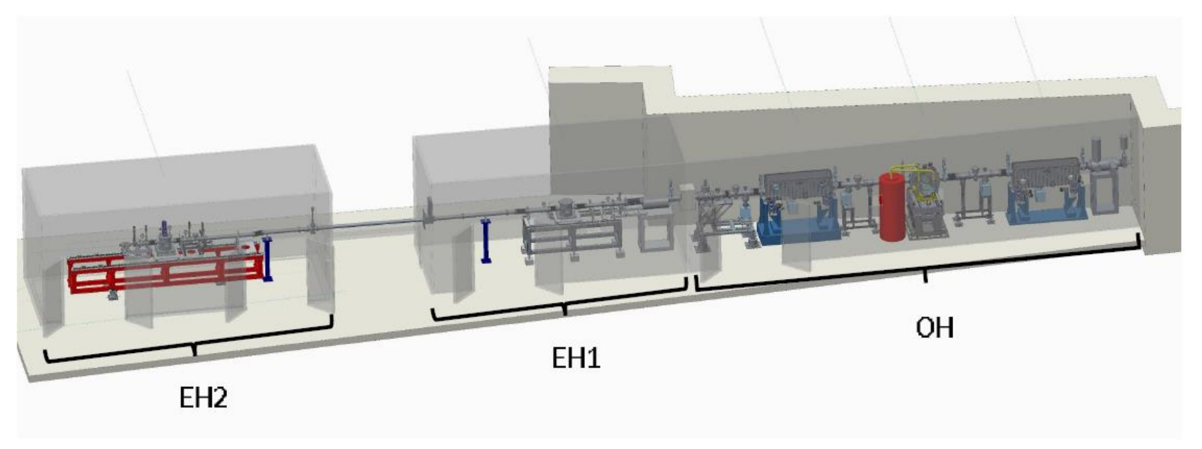

Figure 1: General layout of the LISA beamline. Picture from [Dac-19].

The center of the first hutch (Optic Hutch, OH) is at about 28m from the source, the first experimental hutch (EH1) is at 37m and the second experimental hutch (EH2) is at 49m and approximately coincides with the focal point of the focusing mirror, M2. In EH2 all the experimental apparata (slits, detectors, vacuum chambers) are supported by a 5m long bench and the vessels can be easily removed to make space for users' instrumentation. EH1 is placed upstream respect to EH2 and here a wide and homogeneous beam spot of ≈1 ×2 mm can be obtained. This reveals to be useful in the case of inhomogeneous samples and in cases when the maximum flux is not required.

1.3 X-ray Optics

LISA takes the beam from a bending magnet of the ESRF ring with an electron beam energy of 6.03 GeV and a typical current of 200 mA (uniform filling mode). The magnet has a field of 0.85 T resulting in a critical energy of 20.6 keV. The source has dimensions 78 μm hor and 36 μm vert Root Mean Square (rms) with emittance values 8.5 nm hor and 25 pm vert and it is located at about 23 m from the principal slits; a 500 μm thick Be window separates the beamline vacuum section from the machine. In the typical angular range accepted by the beamline (1 mrad hor and 50 μrad vert) the total thermal load is about 50W. For the future EBS ring LISA has chosen the Single Bend Magnet (SBM). It will have a magnetic field of 0.85 T thus maintaining the same critical energy as nowadays. The electron beam under the SBM will be highly brilliant with a size of 23(hor) × 3.6 (vert) μm RMS and a divergence of 24(hor) × 3(vert) μrad RMS. Its emission is well separated from the other magnets (Fig.1, right) so constituting a clean source well adapted to microfocus applications [LISA-16]. The layout of the Optic Hutch with the position of the various elements is shown in Figure 2: 1- vacuum chamber with principal slits, attenuators and white beam monitor, 2- first mirror M1, (3-, 6-, 8-) beam monitors, 4- monochromator, 5- cryocirculator, 7- second mirror M2, 9- beam shutter

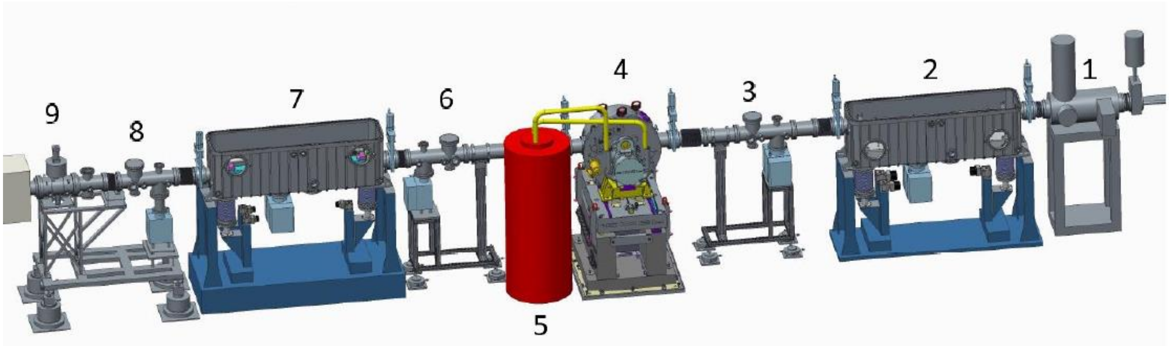

Figure 2: Side view of the optics hutch. Picture from [Dac-19]. Reproduced with permission of the International Union of Crystallography.

The first vacuum vessel contains the principal slits and a set of attenuators (100 to 500 μm C, 100 to 1000 μm Al, 100 to 250 μm Cu) that permits to reduce the thermal load on the subsequent optical elements. The first optical element is a collimating mirror M1, followed by the monochromator and by the focusing mirror M2. A pair of Pt coated plane and parallel mirrors placed in EH1 achieve the harmonic suppression at energies below 11 keV. The mirrors were produced by THALES-SESO (THALES-SESO S.A.S, Aix en Provence, France http://seso.com/) whereas the monochromator was manufactured by CINEL (CINEL Strumenti Scientifici S.R.L., Vigonza, Italy, http://www.cinelsrl.com/cinel/).

M1 has a cylindrical shape and it consists of a single crystal Si substrate with two optical regions each 35mm wide and 900mm long; one exposing the silicon, the other coated with Pt. The mirror is located at ≈24.9 m from the source and has a radius of curvature that can be varied, via a stepper motor, to maximize the beam collimation (theoretical meridional curvature radius $R^{M1}{}_{m}$ = 24.9 km. Data from the manufacturer report a slope error below 0.5 μrad and a roughness below 2 Å (rms values). The working angle for both M1 and M2 has been chosen to be 2 mrad because with this value the cutoff of the Si stripe (about 15 keV) is slightly above the L absorption edges of Pt. In this way the reflectivity in the operating energy region for both surfaces contains no abrupt steps and it is possible to have a wide energy range with only two coatings.

Figure 3: Picture of M1 in its vacuum vessel.

M1 is cooled by water via two copper blades inserted in longitudinal trenches filled with GALINSTAN (GaInSn) liquid metallic alloy. This mirror (as well as the other one that will be described in the following, M2) has suitable external mechanics (stepper motor + encoder on the translations) for the definition of the incidence angle and the choice of the reflecting stripe. This is realized by 3 vertical actuators ("vertical" kinematical plane) whereas 2 more actuators realize the horizontal positioning + yaw angle, all with a precision of 5 μm.

The monochromator is of the *fixed-exit* type with an offset of 15mm and it is equipped with two pairs of flat Silicon crystals, Si (311) and Si (111). All the crystals are mounted on the same cage so the change from one pair to the other can be carried out via a simple horizontal translation of the vacuum vessel. The angular operative range is 3.5°- 51° thus allowing to reach the energy range 2.5-32.5 keV with the Si(111) crystals, 4.9-72 keV with the Si(311) crystals and 7.6- 97 keV with the Si(333) reflection (3rd harmonic of the Si(111)). An incremental encoder mounted on the last rotation stage (linked to the crystal cage) with resolution 22 nrad is used for the determination of the angular position. A single stepping motor drives at present the Bragg rotation but the design allows the installation of a Direct Current Motor if the operation in continuous scan mode is required.

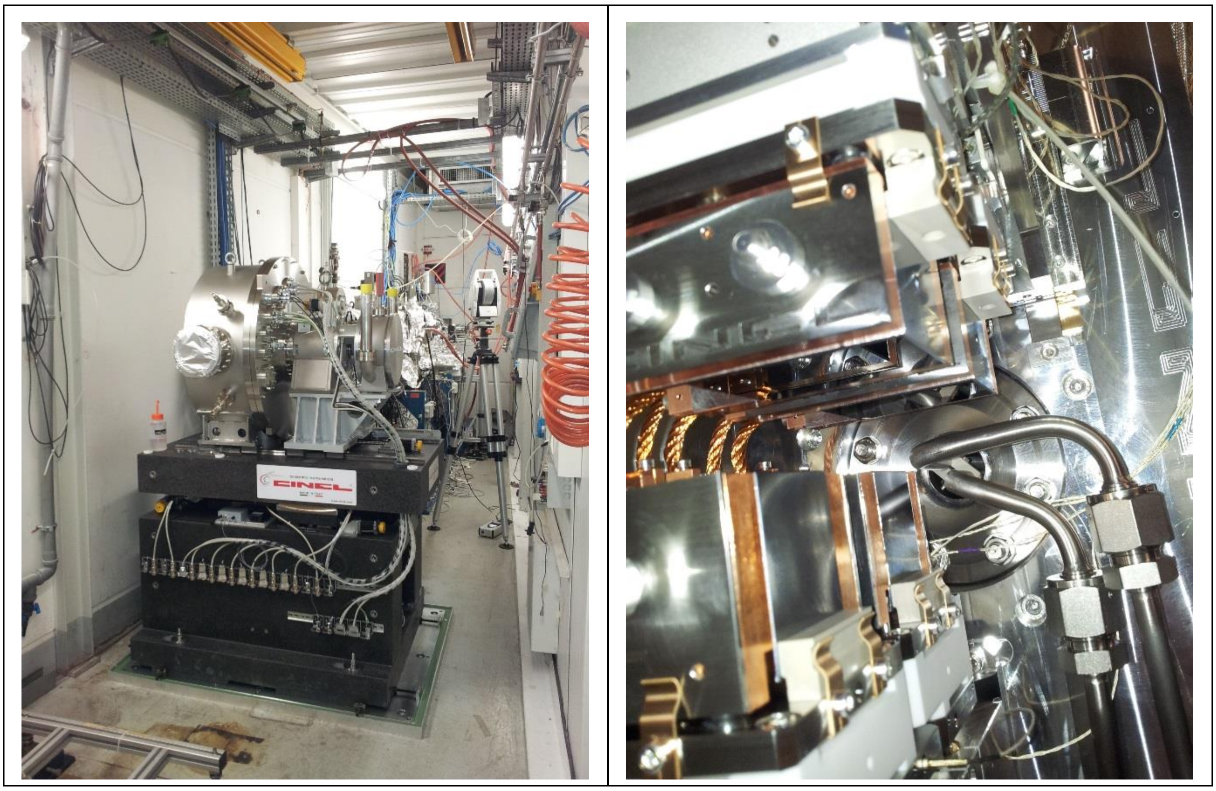

Figure 4: Pictures of the monochromator during the installation phase.

The second crystals have cascaded actuators for the pitch movement: a stepper motor for coarse positioning and a piezo for fine positioning. The piezo actuator of the pitch movement can be driven directly (manually changeable voltage) or inserted in a fast (analogic) feedback controller for the stabilization of the output intensity. In this latter case the working point (duty point) can be chosen either as fixed absolute value of the readout of the I_0 ion chamber or a fixed position in the reflectivity curve by tracking in time the ring current. 2 *roll* actuators (one per crystal) driven by stepper motors are also present on the second crystals. This allows to adjust independently the parallelism of the diffracting planes of each pair (planes are usually not perfectly aligned with the physical surfaces, in our case the misalignment resulted to be less than 0.01 deg) permitting in this way to avoid the horizontal drift of the beam for different values of the Bragg angle.

The first crystals have dimensions 40mm (width W), 48mm (thickness T) and 140mm (length L) whereas the second crystals have dimensions 40mm × 37mm × 57mm (W × T × L). The considerable thickness ensures a good resistance against mechanical deformation due to mounting. They are indirectly cooled by liquid nitrogen fed by an external cryocirculator manufactured by CRIOTEC (Criotec Impianti SPA, Chivasso, Italy https://www.criotec.com/en) connected with the general liquid nitrogen distribution network. The cooling circuit operates at a pressure stabilized at 2.8 bar (with a Standard Deviation variation over several days 0.2 mbar) and the liquid flux is about 3.5 l/min.

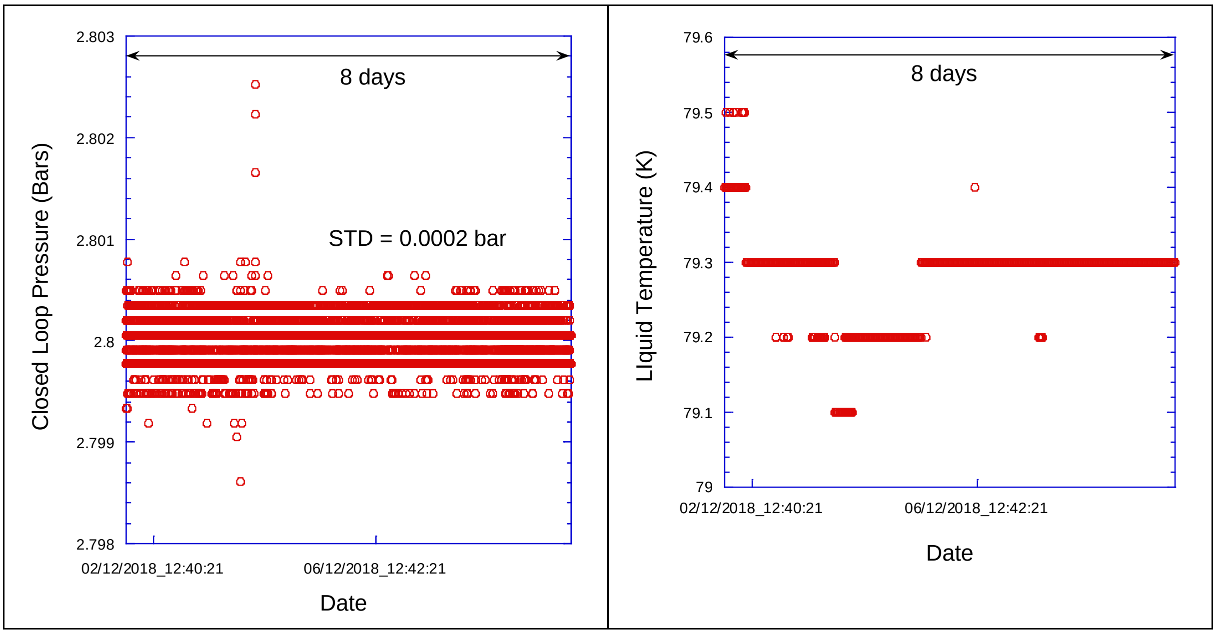

Figure 5: Mono Cryocooler: Left: Time evolution over several days of the pressure in the liquid Nitrogen closed loop Right: evolution of the liquid temperature in the same period.

The mono motion is controlled by SPEC using as the main variable the Bragg angle that defines the nominal energy (knowing the crystal type) and the crystal gap value to use. The Bragg angle is defined by the cumulated steps of the Bragg motor but this represents only a coarse determination of the angle (an offset is added to this value during the energy calibration procedures at the beginning of the experiments). The counts of the main Bragg encoder (stored in the raw datafile) are successively used by an offline routine to create the final and accurate energy scale; all XAS data shown hereafter have been treated in this way.

For accessing the highest part of the energy spectrum (>40 keV) the mirrors are removed and the monochromator lowered thanks to the vertically adjustable granite support (manufactured by ZALI SNC, Scopa, Italy, http://zali-precision.it/) having a total stroke of 15 mm.

M2 is a double toroid and it consists in a single substrate of crystalline silicon with two parallel cylindrical channels one of which is coated with Pt. This mirror is located at 31.6 m from the source and its (fixed) sagittal radius is R^{M2}_s = 45.8 mm whereas the meridional radius R^{M2}_m can be varied with a stepper motor to match the theoretical value of 17.9 km.

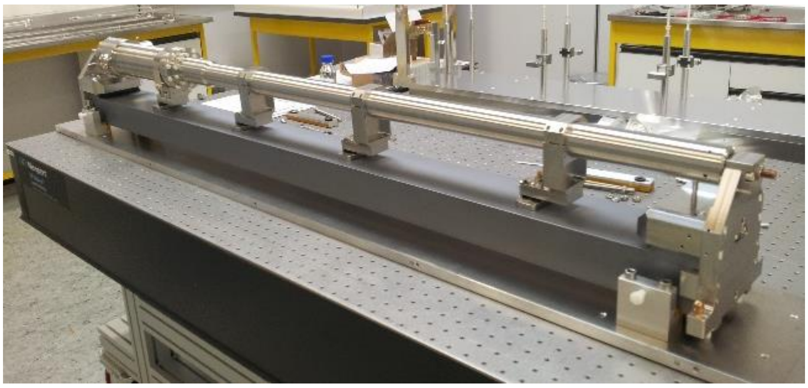

Figure 6: Picture of M2 on the assembly bench.

This permits the focalisation of the beam at 17.9 m from the mirror inside the EH2 hutch. The focusing geometry is 2:1 and this value has been chosen in order to limit the total length of the beamline and to minimize the aberrations.

In order to appropriately reject the harmonics in the lower part of the operating spectrum (mainly 4-6 keV) a pair of flat mirrors coated with Pt and working at 8 mrads is used, located in EH1. After this device, a second Be window of about 500 μm parts the high vacuum section of the beamline (including the white beam path and the main optical elements) from the following *low vacuum* sections. This window is considerably robust against accidental venting but it strongly limits the operating range of the beamline at low energy. In the case where a thinner Be window at the Front End is made available by the ESRF the installation of a thinner window also in this point will be taken into consideration.

1.4 Overall performance

1.4.1. Energy resolution

The performance of the beamline have been determined during a dedicated commissioning run and are summarized hereafter. A parameter of paramount importance for a spectroscopy beamline is the energy resolution. This depends on the crystal planes used for the data collection but also on the thermal bump and on the effective collimating power of the first mirror, especially when needing a high flux. The (meridional) radius of curvature of the first mirror $R^{M1}{}_{m}$ has been optimized by collecting a series of spectra of a benchmark compound, in this case gaseous Br at the Br-K edge (13474 eV) [Fil-00], with the Si(111) crystals. The pre-edge peak has been successively fitted with a pseudo Voigt function (using the approximation presented in [Oli-77]) consisting in a Lorentzian with Full Width at Half Maximum (FWHM) equal to 2.52 eV (the natural width as derived from [Kra-79]) convoluted with a Gaussian of variable width.

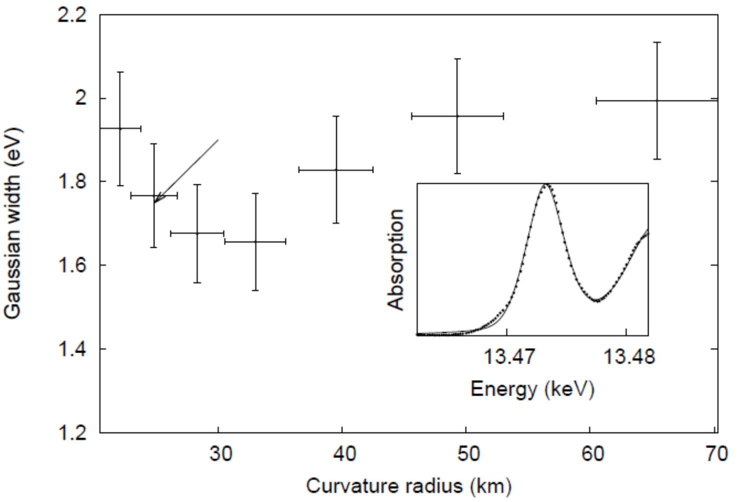

Figure 7: Optimization of the meridional curvature radius of M1. Picture from [Dac-19], Reproduced with permission of the International Union of Crystallography.

Figure 7 shows The Width of the Gaussian component of the pseudo-Voigt line as a function of the meridional radius of curvature of M1, R^{M1}_m. Data were collected with the vertical principal slits at 2mm so realizing a high flux configuration (vert divergence 90 μrad). The point of the arrow marks the theoretical radius of curvature for perfect collimation and the theoretical value of the energy resolution (crystal intrinsic). The minimum width of the Gaussian is obtained with a radius of curvature around 30 km (according to the offsite manufacturer's calibration curve) in fair agreement with the expected value of 25 km. The resolution obtained (≈1.7±0.1 eV) is in good agreement with the intrinsic resolution of the Si(111) crystal, 1.75 eV at the Br-K edge energy (for Si(111) $\Delta E/E = 1.1 \times 10^{-4}$ [Ish-05]). This means that even at the maximum vertical acceptance (high flux condition of the beamline) the energy resolution remains close to the theoretical predictions. The optimum radius resulted to be the same if using the Pt or Si side of the mirror. With the optimized R^{M1}_m value the rocking curves of the two crystal sets at different energies were collected and their Full Width at Half Maximum (FWHM) compared with the theoretical values are shown in Figure 8.

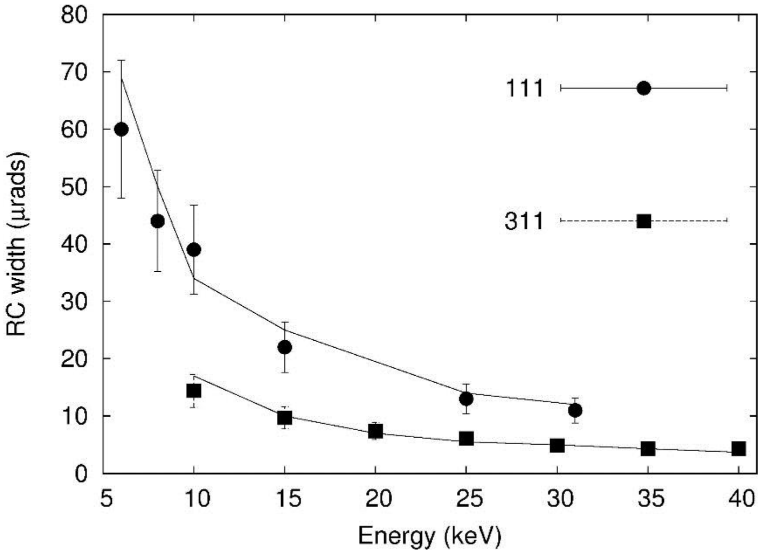

Figure 8: Theoretical (lines) and experimental (symbols) values of the Rocking Curve width at different energy values. Picture from [Dac-19] Reproduced with permission of the International Union of Crystallography.

The measured data follow closely the theoretical calculations (realized with the XOP code [san-11.1]) revealing that the principal sources of resolution degradation (namely, the crystal mechanical stress and/or the residual vertical divergence of the incoming beam) have a negligible contribution.

1.4.2. Flux

The flux available on the sample in focusing conditions has been measured in EH2 and it is reported in Figure 9

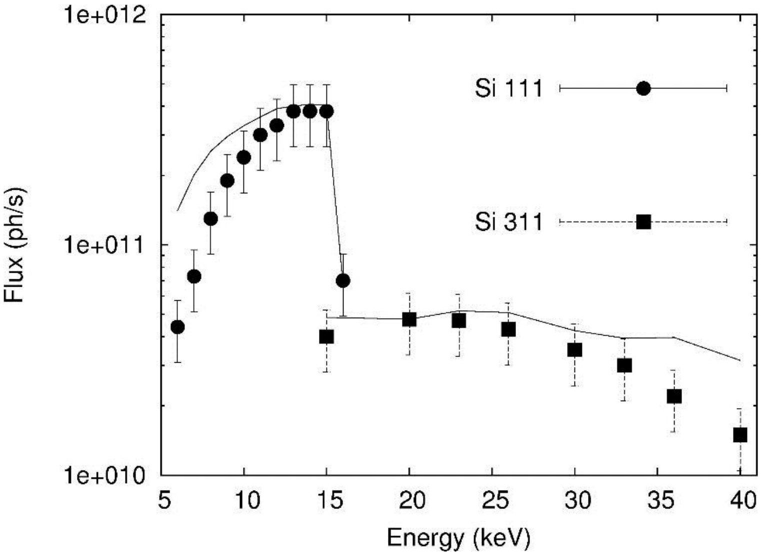

Figure 9: Measured (points) and calculated flux at the sample. Picture from [Dac-19]. Reproduced with permission of the International Union of Crystallography.

The values are in the 10^{11} ph/s range for the Si(111) crystal and on the 10^{10} ph/s range for the Si(311) crystal. The measured data follow satisfactorily the theoretical calculation with deviations at the extremes of the energy spectrum accessible: at high energy (probably due to a mirror roughness higher than what stated by the manufacturer) and at low energies (reasonably due to a higher-than-expected absorption from the Be windows).

1.4.3. Beam shape and size

The simulations of the beam shape in the focal point with the final beamline parameter have been realized by X-ray tracing using the SHADOW3 code [San-11.2]. A Si(111) crystal was considered, at 10 keV and mirror surface errors taken from data on similar mirrors measured by the ESRF optics group. The theoretical size results to be about ≈120 (h) × ≈180 (v) μm^2 FWHM and it is shown in Figure 10.

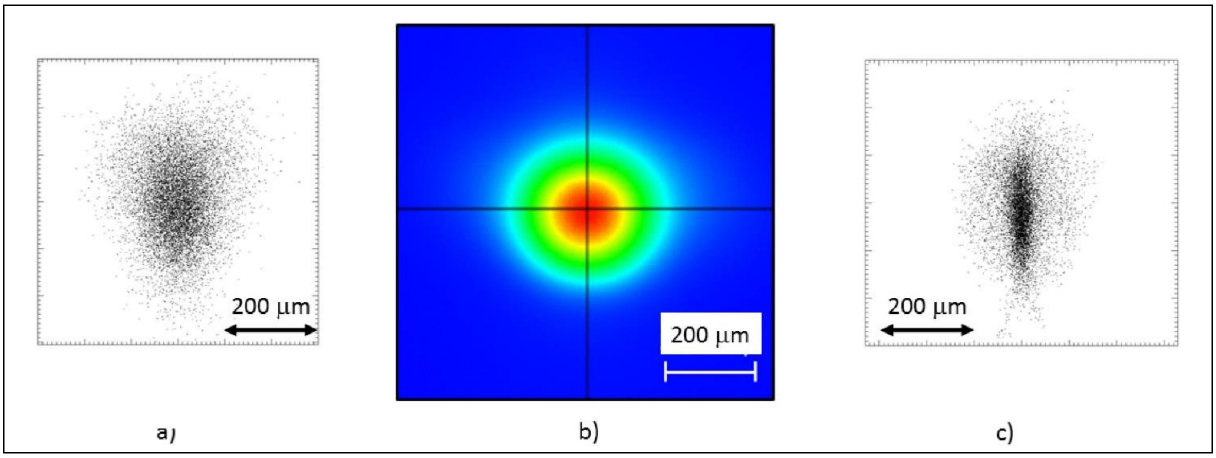

Figure 10: Theoretical and experimental beam spots. a) theoretical calculation for the present ESRF source, b) experimental spot, c) calculated spot with the EBS source. A ruler at 200 μm is also shown and is relative to both vertical and horizontal dimensions. Picture from [Dac-19]. Reproduced with permission of the International Union of Crystallography.

The experimental data have been collected both with a high resolution camera and with a blade scan yielding in both cases a size of ≈170 (h) × ≈180 (v) μm^2 FWHM, in fair agreement with the theoretical predictions. This beam shape and the low divergence will allow the collection of data in total reflection condition with the beam polarization parallel and perpendicular to the sample surface.

As already stated, the use of the toroidal mirror allows also to obtain a large (mm sized) and homogeneous beam in the *off-focus* position (in our case the center of EH1) where XAS measurements can be carried out, namely, on highly inhomogeneous samples.

1.4.4. Energy stability

In the collection of data in differential mode the stability of the energy scale is a parameter of pivotal importance. Energy shifts of the order of 10 meV at 10 keV can be sufficient to give rise to artifacts in the difference spectrum. The stability of the monochromator has been verified by subtracting two independent spectra of several compounds at different energy values and crystals, here we present the case of spectra collected on GeO_2 at the Ge-K edge collected with Si(111) crystals. The data were collected in the standard way using N_2 filled ion chambers and feedback stabilized output intensity. The choice of this compound comes from the coupling of two facts: a limited core-hole width (1.96 eV [Kra-79]) and a relatively small Bragg angle ($\Theta_B \approx 10$ deg) that result in a steep edge ideal for energy stability testing the local derivative $D = \partial\mu \setminus \partial\Theta_B$ on a normalized spectrum (i.e. edge step $\Delta\mu = 1$) is about $D \approx 300$ deg^{-1}. The result is shown in Figure 11

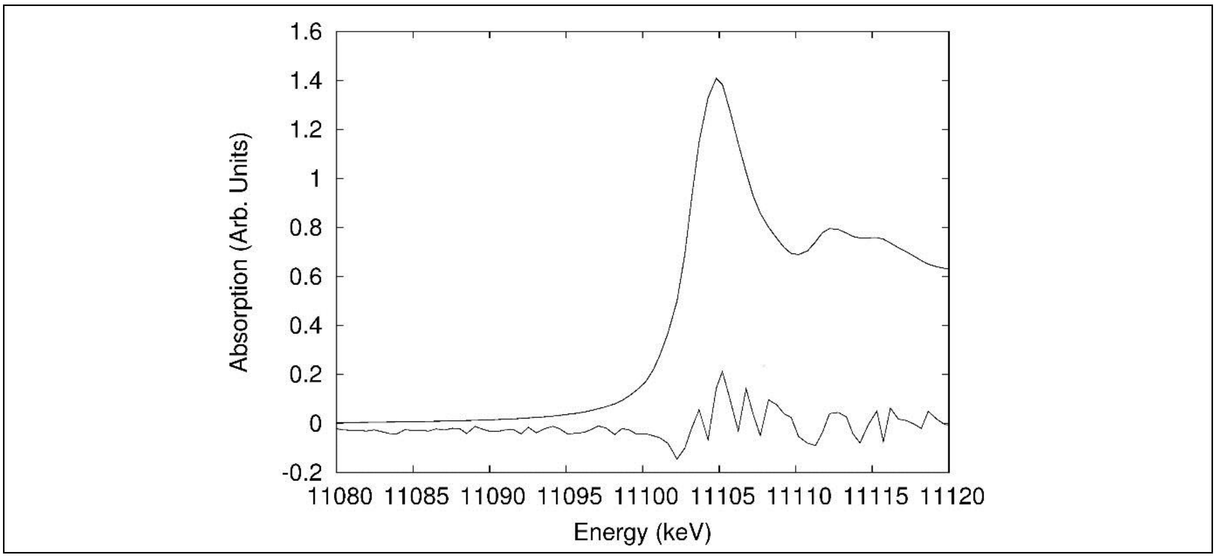

Figure 11: Two consecutive XANES spectra on a GeO_2 sample and related difference (lower curve, multiplied by a factor 100) collected at the Ge-K edge with Si(111) crystals. Picture from [Dac-19]. Reproduced with permission of the International Union of Crystallography.

The difference between the two spectra show no appreciable structures meaning that the energy calibration has remained stable in the short term of data collection (about 10 min/spectrum). In a period of several hours, however, shifts of the order of 1.5 μrad (tens meV) have been observed. The origin of this instability is currently under investigation.

1.4.5. Noise

A final parameter determining the quality of the data is the residual noise obtainable in a transmission mode experiment. Figure 12 shows an example on a Titanium foil Ti foil collected at Room Temperature with the Si(111) crystals in the *off-focus* position in EH1

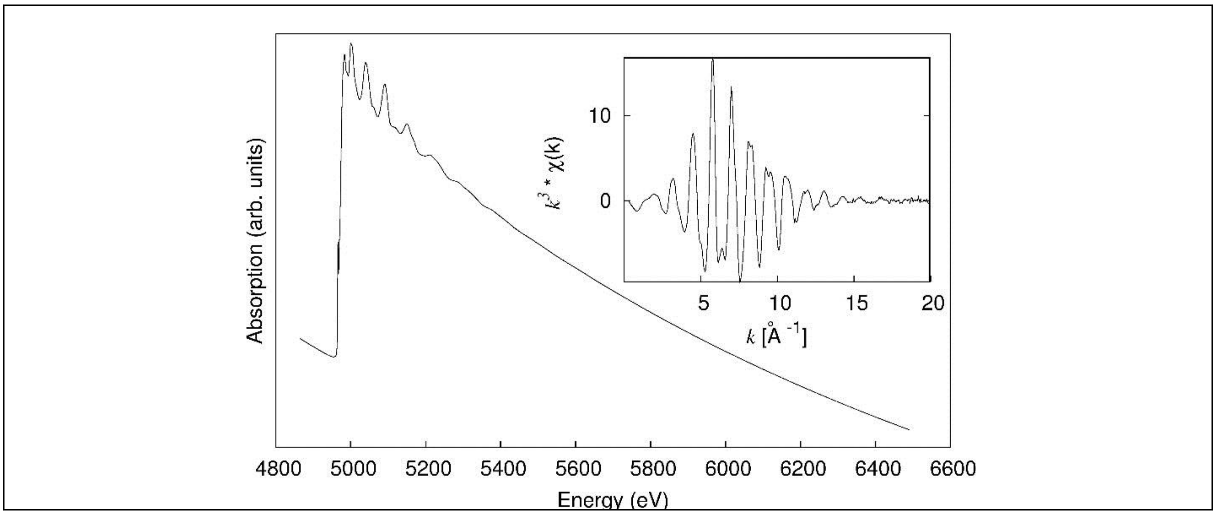

Figure 12: Example of a spectrum of a Ti foil collected at Room Temperature. The inset shows the EXAFS signal up to 20 Å^{-1} multiplied by a k^3 weight. Picture from [Dac-19]. Reproduced with permission of the International Union of Crystallography.

The residual noise has been determined as 6×10^{-5} rms, overall the data quality is good and at the same level as previous reports [Fil-00, Lut-09].

1.5 Experimental setup

1.5.1. EH1

The instruments for the data collection are grouped in two experimental hutches, EH1 and EH2. The former cabin (see Figure 13) is close to the M2 mirror and it is used when a large and homogeneous beam (dimensions about 1×2 mm) is desired.

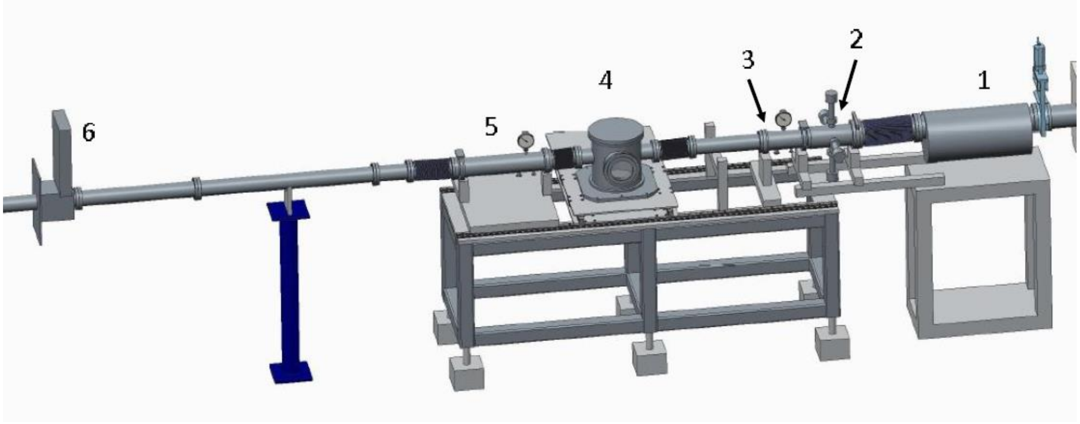

Figure 13: Sketch of EH1. Picture from [Dac-19]. Reproduced with permission of the International Union of Crystallography.

With reference to Figure 13 the main elements are: 1- chamber with low energy mirrors, 2- slits, 3- ion chamber I_0, 4- sample chamber, 5- ion chamber I_1, 6- shutter. The first vacuum vessel contains the mirrors for harmonic rejection at low-energies. Successively we have a vacuum chamber with a manipulator for the sample preceded and followed by ion chambers (length 150mm I_0 and 400mm I_1). These detectors are *parallel plates* chambers that can be filled with N_2, Ar or Kr gases at a pressure varying from 0.1 to 1 bar. A manual distribution of gases is available for the users. The typical electric field value in the chambers is around 1 kV/cm. The signals from these chambers are read by pico-amperometers and their output sent to the data acquisition computer via voltage-to-frequency converters. A support positioned laterally respect to the vacuum chamber permits the installation of one of the High Purity Germanium detectors available at LISA.

1.5.2. EH2

The subsequent experimental hutch EH2 is centered on the focal spot of M2 (see Figure 14).

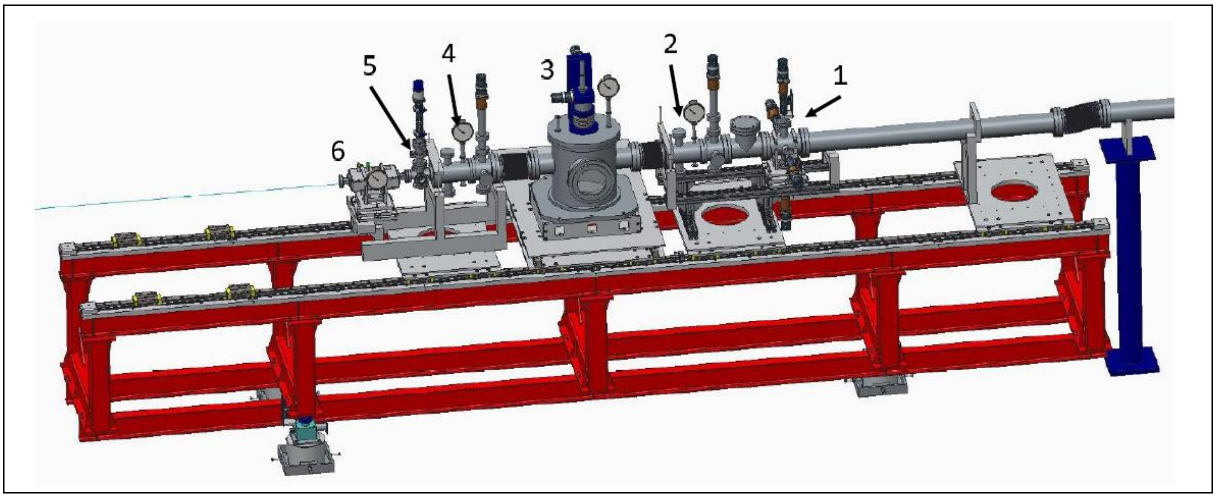

Figure 14: Sketch of EH2. Picture from [Dac-19]. Reproduced with permission of the International Union of Crystallography.

Numbers in Figure 14 label the various elements: 1- slits, 2- ion chamber I_0 3- sample chamber, 4- ion chamber I_1, 5- reference foils holder, 6- ion chamber I_{ref}. Data in this position are collected with the fully focalized beam. The instrumentation for data collection in EH2 consists in 3 ion chambers of length 100 mm similar to the ones previously described. Also here the gas type and pressure regulation is realized via a manually operated gas distribution line.

1.5.3. Detectors

For the collection of fluorescence from the samples two High Purity Germanium (HP-Ge) detector arrays (one with 12 elements the other with 13 elements) are available for high energies (E > 15 keV) whereas in the lower energy range a 4 channels Silicon Drift Detector (SDD) is used (ARDESIA project, [Bel-18], [LISA-18]). This detector is particularly effective for X-ray Fluorescence (XRF) and X-ray Absorption Spectroscopy (XAS) experiments at E < 15 keV, offering high count rates (up to 1Mcps/channel) and high energy resolution (down to 150 eV FWHM). The detection module consists of 2 × 2-pixel monolithic SDD coupled with a 4-channel version of the CUBE CMOS preamplifier [Bel-18]. The instrument has been realized to fit inside the sample chamber with a finger-like structure and allows to operate in vacuum. A built-in Peltier system grants proper cooling (-30 °C).

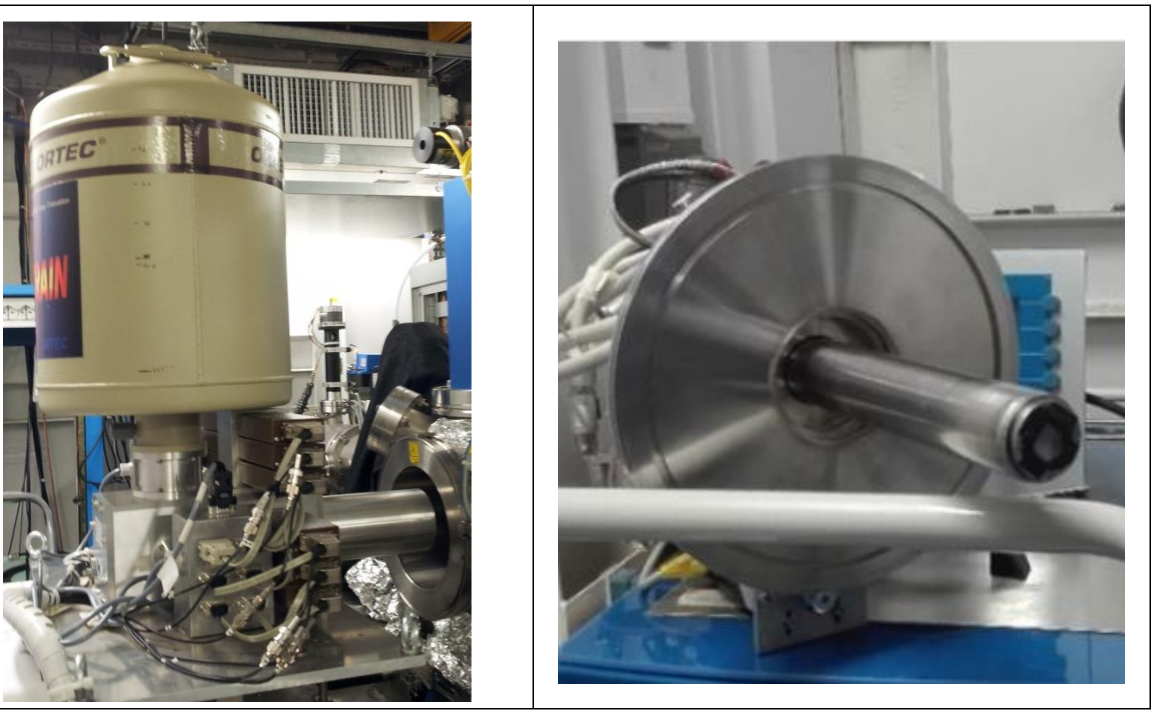

Figure 15: Pictures of some fluorescence detectors. Left: the 12-elements HP-Ge; Right: the 4 elements SDD.

In both cases the readout is made by digital analysis of the output pulses using the XIA-DXP system.

A system for the collection of XAS-XEOL data is also available [LISA-15: it consists in a lens (BK7 glass) collecting the emission from the sample coupled to a silica optic fibre. This ensemble is mounted inside the measurement vessel and can operate in vacuum and with the sample at LNT. The fibre runs out of the vessel via a feedthrough and it shines a fast photomultiplier tube (PMT, model HAMAMATSU H3164-10) sensitive in the range 300-650 nm. Between the tip of the fiber and the PMT band-pass optical filters (bandwidth 10nm) can be mounted in order to select the desired optical emission band. When working in 16b or 4b mode the PMT pulses can be windowed by a fast gate (Philips mod 744) synchronized with the machine flashes thus realizing a time resolved data collection. Samples for XAS-XEOL are prepared in pellets with a moderate absorption ($\Delta\mu \approx 0.1$) in order to obtain a good optic signal and at the same time a spectrum in transmission mode. Data shown here were collected with the ring operating in 16 bunch mode. The sample was a pellet of ZnO which is known to emit under X-ray excitation in two bands one centered at 390 nm (gap transition) and the other at 500nm (defect states). XAS data were collected at the Zn-K edge.

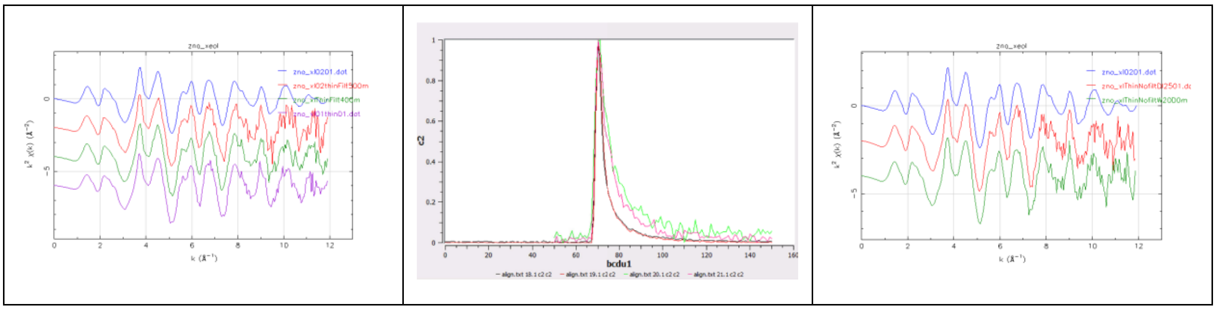

Figure 16: Left: XEOL-XAS data collected at different emission wavelength; Center: Time response of XEOL at different wavelengths, Right: XEOL-XAS spectra collected at different times after the X-ray pulse. (see text for details, pictures from [LISA-15]).

Figure 16 summarizes some features of the data collection system. The plot in the left side shows spectra taken at different wavelength values (purple: full emission, green: 400nm, red 500nm) compared with the data taken in transmission mode (blue line). In all cases a signal of good quality could be collected demonstrating the effectiveness of the use of bandpass filters for wavelength-resolved XEOL. The plots in the center and right panels refer to time-resolved data collection. The central panel shows the emission from the sample for different values of delay between the x-ray flash (arriving at about 70ns in the time abscissa) and the position of the pulse collection window (width=10ns); data were adapted to a common scale for an easier comparison. The decay of the curve is linked to the decay of the luminescence at the selected wavelength. Data were collected for the full emission (Black curve), emission at 400nm (red), 450nm (pink), 500nm (green): as expected, the emission at longer wavelength is slower.

1.5.4. Sample Treatment

Experiments are carried out in vacuum chambers with manipulators hosting cold finger or cold chamber cryostats (temperature range from room temperature to 20K), an intermediate temperature holder (credits to F. Rocca, FBK-Trento and S. Esmail, Suez Canal Univ., [LISA-18]) or a high temperature reactor cell (MICROTOMO, [Bel-03], [LISA-15]).

The intermediate temperature holder is particularly adapted to accurate temperature-dependent EXAFS measurements. The device allows to reach temperatures from 80K up to 525K and it is equipped with a gold-plated copper sample holder in order to maximize thermal conductivity The sample holder allows to mount up to four samples, the vertical range of movement is 10 cm and the manipulator can be rotated by 180° around the vertical axis. The temperature is controlled via a Eurotherm unit, allowing remote control with SPEC. The device provides a very precise temperature control on the mounted samples with a temperature stability of approximately ±0.03K.

The MICROTOMO furnace is extremely compact and can be mounted directly inside the EXAFS chamber in both absorption and fluorescence modes. The system allows full temperature control between room temperature and 800 °C both under vacuum and gas flow, allowing in-situ measurements during temperature annealing or chemical reactions. The temperature is settled via Eurotherm controller, which allows maximum ramping rate of 10°C/min and really good thermal stability. It’s also possible to program a thermal cycle.

The ovens and other sample environment devices can be easily exchanged between the two experimental hutches.

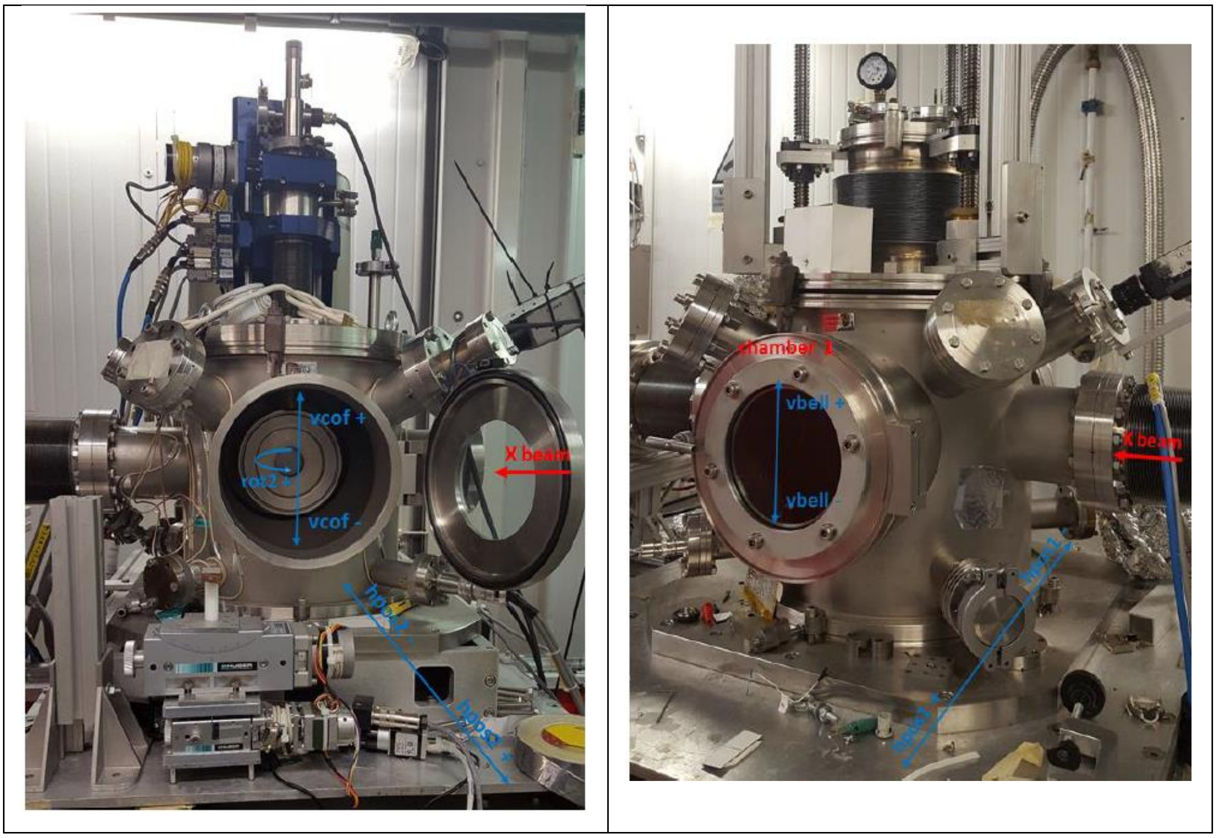

Figure 17: Sample manipulators. Left: Sample chamber equipped with the manipulator bearing the liquid He/N$_2$ cold finger, Right: Sample chamber equipped with the manipulator for heavy treatment cells (ex. MICROTOMO). From [LUM-18].

Concerning Pump and Probe experiments, recently LISA has acquired (via the participation to project NEWLI PRIN 2015CL3APH) a fast source consisting in a diode laser (mod. PiLas by A.L.S. GmbH) that can provide pulses of wavelength l = 404 nm, duration t = 1 ns of energy E = 465 pJ at a repetition rate of 5.6 MHz corresponding to the machine frequency in 16 bunches mode. The output of the laser is sent to an optic fibre that enters the sample vacuum chamber and shines the sample through a focusing lens. The beam spot is about 2mm for an easier alignment with the X-ray beam. Using a fast photomultiplier placed at the sample location it is possible to detect at the same time the X-ray and UV pulses and set the delay parameters between the pump and the probe beams [LISA-18].

1.5.5. Surface analysis

For the surface analysis of the samples the ReflEXAFS chamber operative at GILDA [Dac-03] can be installed in EH2, as an alternative the other grazing incidence apparatus [Mau-09] can be used. Recently (credits to A. Fantin, TU Berlin), a new apparatus for XAS measurements in Total Electron Yield mode has been realized. It allows to probe up to six samples, with the possibility to collect simultaneously fluorescence and TEY spectra. The main characteristics are: i) Secondary electrons collector, anode at V ≈ 17 V , ii) He gas electron multiplier , iii) Multi-sample holder (up to six specimens). The device is placed in the measurement chamber filled by He gas (0.8 bar) for signal amplification [LISA-18].

1.5.6. Beamline Control

All operations for sample alignment and data collection are carried out via SPEC (Certified Scientific Software, Xray Diffraction Software. Cambridge. MA. https://certif.com), and, for the more standard tasks, Graphical User Interfaces (GUIs) are available. Macros for data collection on up to 6 samples are available with GUIs for an easier operation by the user

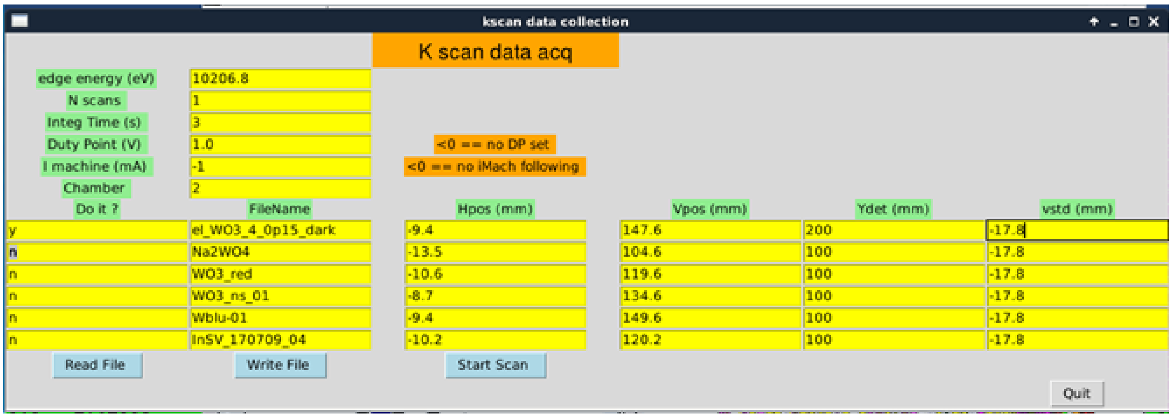

edge energy (eV) 10206.8
N scans 1
Integ Time (s) 3
Duty Point (V) 1.0
I machine (mA) -1
Chamber 2

<0 == no DP set
<0 == no iMach following

Do it ?	FileName	Hpos (mm)	Vpos (mm)	Ydet (mm)	vstd (mm)
y	el_WO3_4_0p15_dark	-9.4	147.6	200	-17.8
n	Na2WO4	-13.5	104.6	100	-17.8
n	WO3_red	-10.6	119.6	100	-17.8
n	WO3_ns_01	-8.7	134.6	100	-17.8
n	Wblu-01	-9.4	149.6	100	-17.8
n	InSV_170709_04	-10.2	120.2	100	-17.8

Figure 18: Example of a GUI for the collection of XAS spectra on 6 samples using a constant mesh in k (photoelectron wavenumber) space. For each sample the vertical and horizontal position are defined as well as the distance of the HP-Ge detector [LUM-18].

Datafiles are stored in ASCII format and contain information on a large set of detector readouts, monochromator positions and machine parameters; specific routines are available for the extraction of columns of interest of the user [LISA-17].

2. Organization

2.1 General Aspects

LISA is the Italian Collaborative Research Group (CRG) at the ESRF. According to the operation contract 70 % of the beamtime is made available for research groups from national institutions whereas the remaining 30%, for ESRF users. The current CRG contract covers the period from January 1st, 2015 to December 31st, 2019; Consiglio Nazionale delle Ricerche (CNR) being the legal contracting part to the ESRF. The formal representative of LISA *vis-à-vis* to the ESRF is Francesco d'Acapito, the beamline responsible.

Beam time proposals submitted for the CRG beamtime are selected by a committee appointed by CNR with a mandate covering the whole contract period. Any Italian public research institution can apply for beamtime at LISA. Proposals are of two types, 'rolling' for spot activity and 'Block Allocation Group" for long term research programs. There is no differentiation between scientific/technical user support for international ESRF and CRG users but CRG users do not receive financial support to cover travel/accommodation expenses.

Each year an annual report is established (Activity report of the Italian CRG beamline at the European Synchrotron Radiation Facility (ESRF), ISSN 2553-9248) containing a résumé of the recent beamline activity and highlight experiments. The reports are published on the IOM institute web site (https://www.iom.cnr.it/gilda-reports).

2.2 Beamline Staff

Resident staff is appointed by CNR through a local antenna (Operative Group in Grenoble, OGG) of the Istituto Officina dei Materiali (IOM). The staff in Grenoble maintains, operates and develops the beamline and provides user support in the broadest sense. This ranges from maintaining scientific contacts with the existing user community, establishing contacts with potential new user groups, investigate technical improvements, design and initiate new experiments, discuss the scientific issues with the users, help and train users in data analysis. Each of the scientific staff members is involved in personal research activities as well. This both via the in-house research program but as well as via collaborations with user groups. The resident scientific and technical staff running the beamline in the period 2014-present, as well as their areas of interest/competences is listed below:

Table 1: Staff having operated at LISA during the period 2014-2018.

Name	Role	Affiliation	Period	Fields of activity
Francesco d'Acapito	Responsible	CNR-IOM-OGG, Permanent	whole contract	Point defects in insulators and semiconductors, methods and instrumentation, micro-electronics.
Alessandro Puri	Post Doc	CNR-IOM-OGG, Fixed Term	Apr. 15 – Present	Highly electron correlations systems (magnetism and superconductivity), air particulate matter
Giovanni Orazio Lepore	Post Doc	CNR-IOM-OGG, Fixed Term	Oct. 15 – Present	Mineralogy, Geology, Environmental science
Angela Trapananti	Researcher	CNR-IOM-OGG, Permanent	Jan. 10 – Jun. 15	Liquids and disordered systems at extreme conditions, earth science, methods and instrumentation.
Simona Torrengo	Post Doc	CNR-IOM-OGG, Fixed Term	Feb. 13 – Oct 14	Imaging, rare earth doped glasses.

Figure 19 illustrates the staff availability (person*months) and the staff turnover within the period 2014-2018:

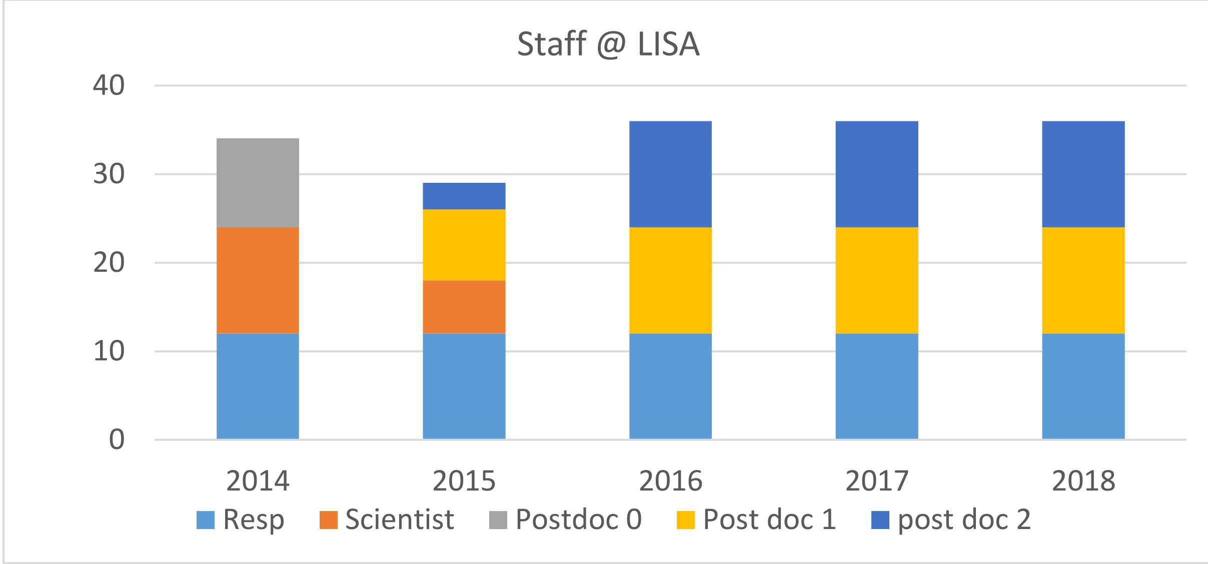

Figure 19 Evolution of the resident staff at LISA (months/person) in the years 2014-2018.

In addition to these persons, other non-resident technicians have worked with the LISA staff intervening in targeted actions:

Table 2: Technical and administrative collaborators of LISA. A Laloni, at present, is at ESS-Lund.

Name	Role	Affiliation	Competernces
Aleksander de Luisa	Technician	Permanent CNR-IOM-Trieste	Drawings
Andrea Martin	Technician	Permanent CNR-IOM-Trieste	Electronics
Alessio Laloni	Technician	Permanent CNR-IOM-OGG (ILL)	Electronics
Eric Dettona	Technician	Permanent ESRF	Liaison with ESRF services
Fabrizio la Manna	Administration	Permanent CNR-IOM-OGG	Administration

During the contract period LISA has hosted several visitors and students as collected in Table 3:

Table 3 Visitors at LISA (stay > 1 month).

Name	Home institution	Period	Funding
Giacomo Rossi	Univ. Bologna (Italy)	Feb-Aug 14	Home inst. funds
Simone Pollastri	Univ. Modena e Reggio Emilia (Italy)	Feb-Apr 14	Home inst. funds

Fabio Capodaglio	Univ. Camerino (Italy)	Aug-Sept 14	Home inst. funds
Chiara Petroselli	Univ Perugia (Italy)	Oct-Nov 15 May-Jul 16	Home inst. funds Home inst. funds
Andrea Giaccherini	Univ. Firenze (Italy)	Giu 16	Home inst. funds
Stefano Pelli Cresi	Univ. Bologna (Italy)	2015	Home inst. funds
Giulia Fantappiè	Univ. Firenze (Italy)	Sept 16 - Jan 17	Erasmus+ Traineeship
Michela la Bella	Univ. Firenze (Italy)	Sept-Dec 17	Erasmus+ Traineeship
Andrea Fantin	T.U. Berlin (Germ.)	Apr-Dec 18	Home inst. funds
Shehab ALI	Suez Canal University (Egypt)	Sept-Dec 18	IAEA Cooperations

3. Beamline Statistical data

3.1 Use of beamtime

LISA has provided beamtime to a wide variety of scientific communities with particular predominance of physicists and chemists. It must be noted however that, in the years 2016-2018 the reconstruction program has heavily affected the beamline activity. In particular, in years 2015-2016 the beamline has operated with the old GILDA setup, then in winter 2017 the new monochromator was installed in during runs 2-3 2017 the beamline operated with the new mono and old mirrors (Hybrid configuration). This was due to the time delay between the delivery of the monochromator and that of the mirrors. Finally, in 2017-18 the new mirrors were installed and LISA started operating in the final configuration. The evolution of the instrumentation is resumed in Table 4

Table 4: User mode and installation activities at LISA during the different RUNs and Shut Down (SD) periods.

	RUN1	RUN2	RUN3	Summer SD	RUN4	RUN5	Winter SD		Legend
2015	▨	▨	▨	▨	▨	▨	▨		▨ GILDA config
2016	▨	▨	▨	▨	▨	▨	🟥		🟨 Hybrid config
2017	🟥	🟨	🟨	🟥	🟥	🟥	🟥		🟥 Installation
2018	🟥	🟩	🟩	🟩	🟩	🟩	🟩		🟩 LISA config

As a consequence, the total amount of shifts available for the users has been severely reduced. The distribution of shifts among the various activities is resumed in Figure 20

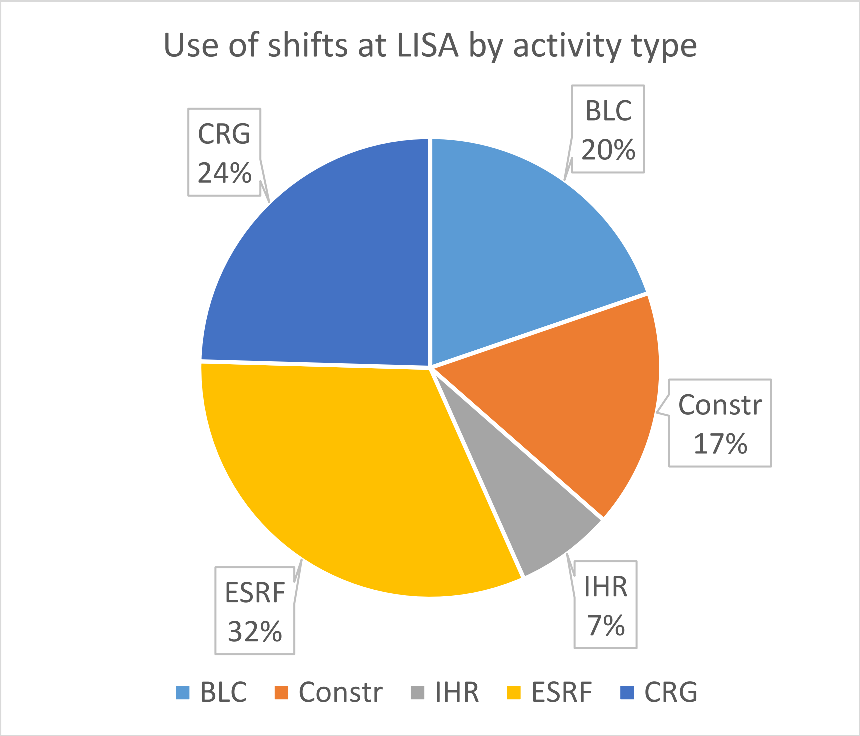

Figure 20: Distribution of shifts by activity type.

A total of 3458 shifts has been considered in total divided in CRG quota, ESRF quota, Beam Line Commissioning (BLC), Construction and In House Research. The beamtime dedicated to the user mode (USM) summed up to 1110 shifts for ESRF experiments and 849 for CRG. The total has been of 1959 shifts in USM i.e. 5% lower than the target of 2072 shifts. The reason for this reduction has been obviously the reconstruction program; it should be noted, however, that ESRF experiments have received 1110 shifts against a target amount of 692 (+60%) whereas the CRG quota has suffered more (849 shifts against a target of 1380, meaning -38%) from the construction activity.

Concerning the USM (both ESRF and CRG) and IHR the distribution of the shifts among the different scientific areas is resumed in Figure 21

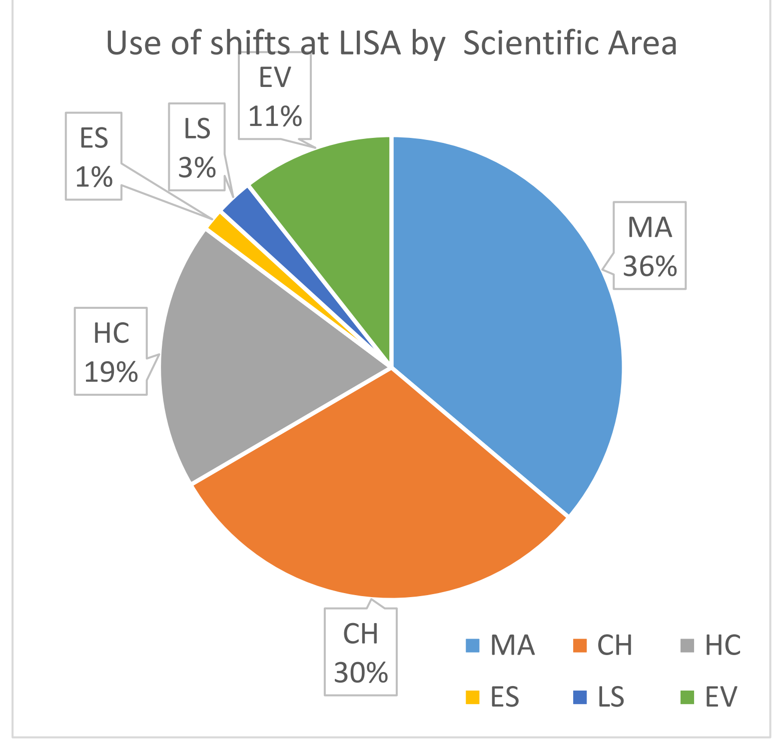

MA : Applied Materials Science

CH: Chemistry

HC: Hard condensed Matter Science

ES: Earth Sciences

LS: Life sciences

EV: Environment

Figure 21: Distribution of shifts among the standard scientific areas defined at ESRF.

The activity of LISA is dominated by 3 main activities: chemistry, hard condensed matter and materials science summing up to 85% of the total number of shifts delivered to the users.

The balance between ESRF and CRG shifts and experiments is given in: Figure 22

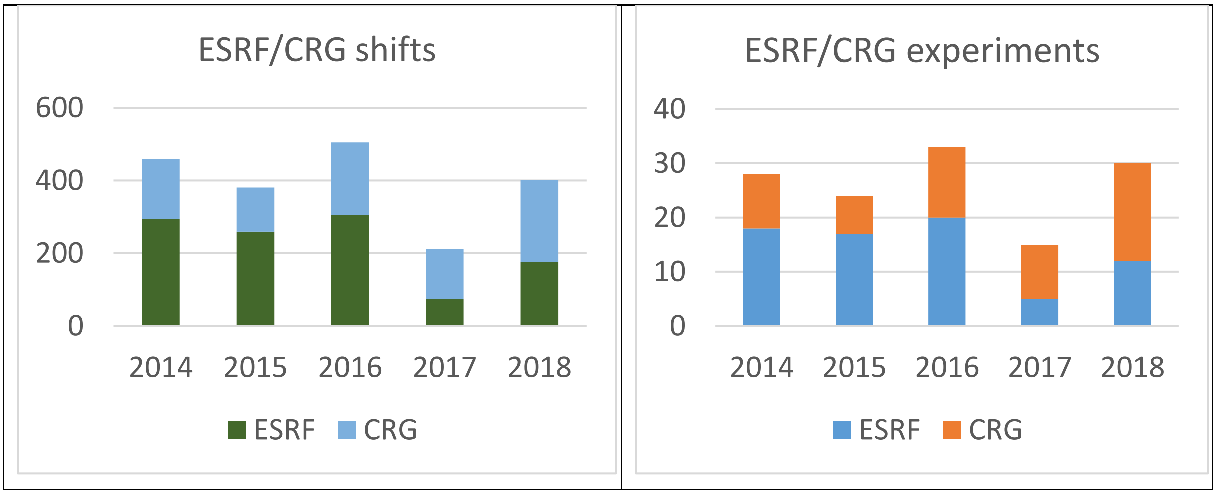

Figure 22: Distribution of Shifts and Experiments between CRG and ESRF.

With the exception of year 2017 (year heavily affected by the construction operation) the beamline has always approached 400 shifts (typical target for USM) and the ESRF shifts have always been above the typical value recommended of about 140. A number of 25-30 experiments has been carried out each year.

The distribution of the nationality of the main proposers (MP) of the ESRF experiments carried out at LISA is shown in Figure 23

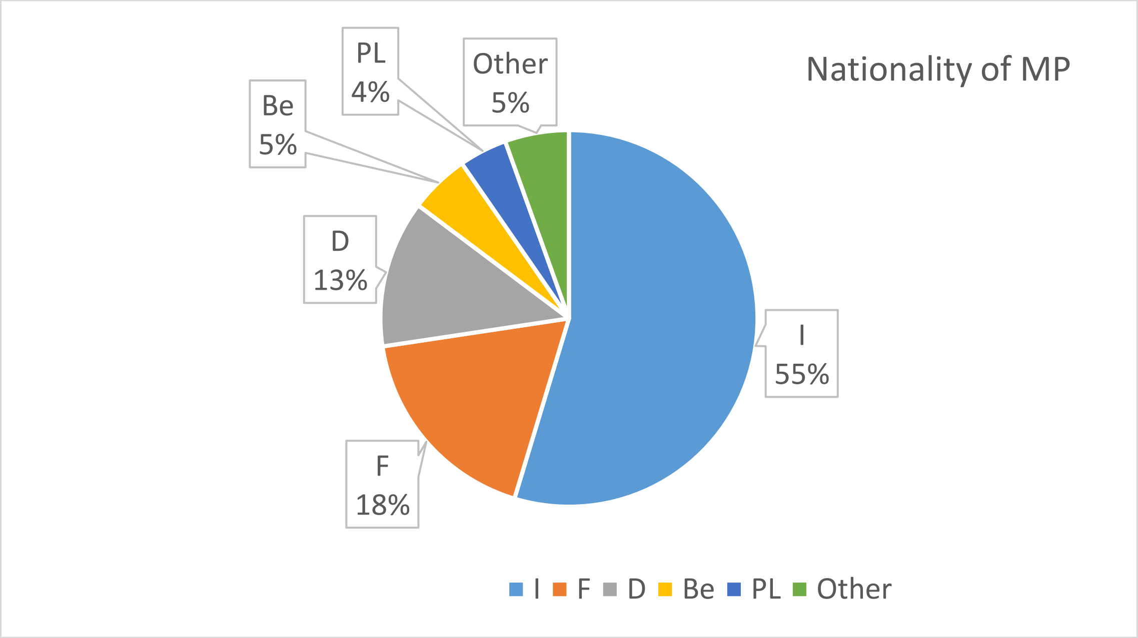

Figure 23: Nationality of main proposer

The Italian scientific community is the dominant one followed by French and German users.

Looking to the ratio between total request and available offer of beamtime (Overload) Figure 24 resumes the situation:

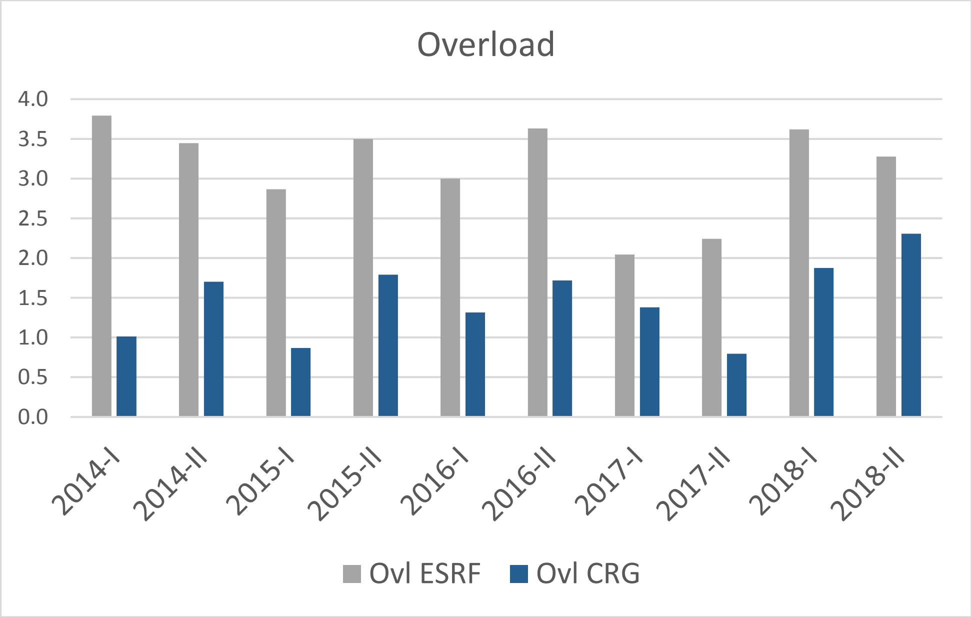

Figure 24: Overload on the ESRF and CRG beamtime quotas

The overload on the ESRF quota is usually above 3 whereas on the CRG quota it is very scattered around 1.5. This reflects the fact that the Italian users have no financial support for the experiments and frequently users apply on the ESRF quota to reduce the impact of the activity on the home laboratory budget. A considerable reduction of requested beamtime has been observed in year 2017 linked to the announced heavy reconstruction program.

3.2 Publications

In the period 2014-2018 the beamline has produced about 25 publications per year for a total number of 138 (data at Feb 2010). The sources for the data relative to publications and their analysis are the ESRF library, Clarivate Web of Science and scijournal.org. The annual production is resumed in Figure 25

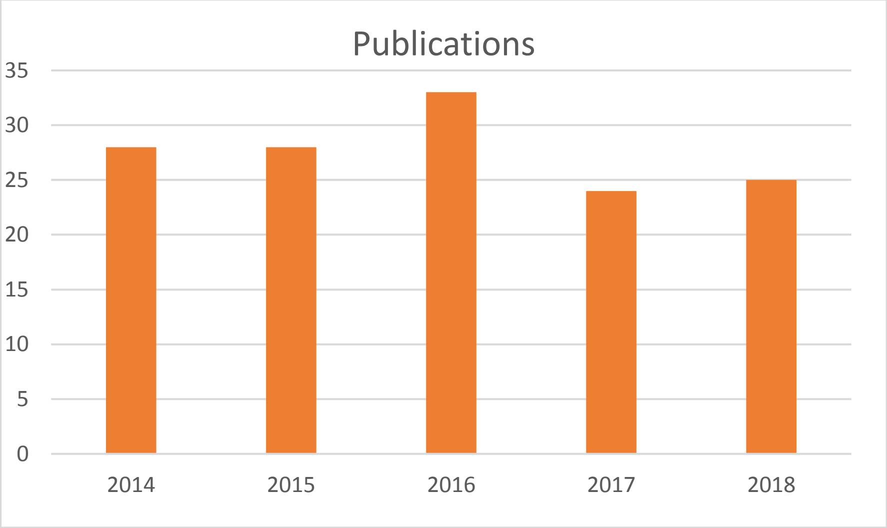

Figure 25: Publications from experiments carried out at LISA.

This corresponds approximately to 1 publication per experiment by comparing with data in Figure 22. The quality of the production in terms of distribution of the Impact Factor of the journals having published research from LISA is shown in Figure 26

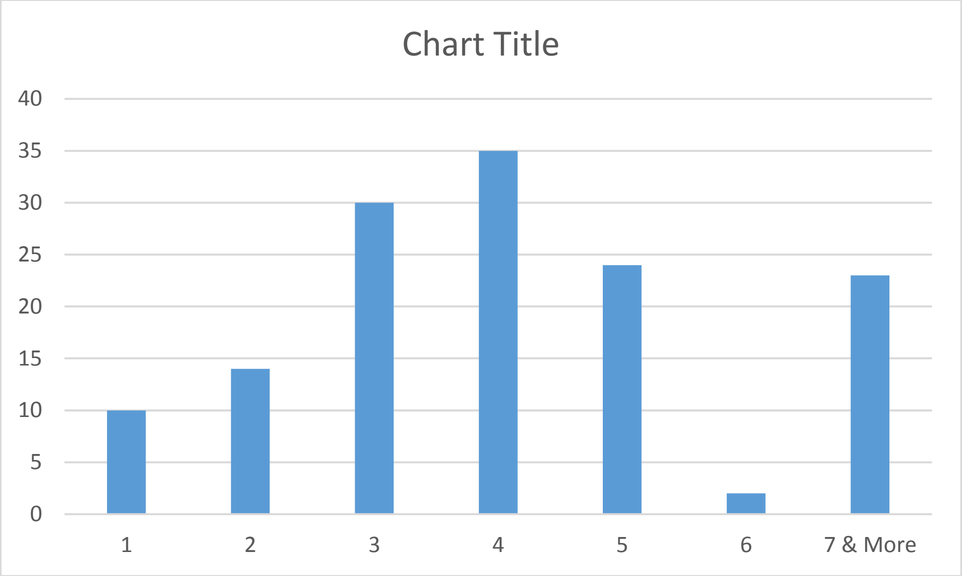

Figure 26: Distribution of the Impact Factor of the LISA publications.

The peak is achieved about at IF=4 with a considerable tail of high impact publications with IF≥7. The quality of the production has also been acknowledged by ESRF with the presence of several LISA contributions to the annual highlights book (Table 5):

Table 5: Contributions of LISA to the ESRF Highlights.

Year	Main Author	Title	Ref.
2015	E. Souchier, CEA Grenoble (F)	THE RESISTIVE SWITCHING MECHANISM OF CONDUCTIVE-BRIDGING RANDOM-ACCESS MEMORY CLARIFIED BY XAS	[Sou-15]
2016	H.A. Miller, CNR-ICCoM, Firenze (I)	NANOSTRUCTURED PALLADIUM-CERIA CATALYST FOR ANION EXCHANGE MEMBRANE FUEL CELLS	[Mil-16]
2016	O. Fenwick, ISIS & icFRC, Univ. de Strasbourg (F)	THE ELECTRONIC AND STRUCTURAL PROPERTIES OF HIGHLY LUMINESCENT OLIGOATOMIC SILVER CLUSTERS CONFINED IN ZEOLITES	[Fen-16]
2017	C. Biagioni, Pisa Univ. (I)	THALLIUM: A HIDDEN HAZARD WITHIN DRINKING WATER PIPELINES	[Bia-17]
2017	Q. Gao, Univ. of Sci. and Tech. Beijing (China)	GUEST SPECIES SWITCHES NEGATIVE AND POSITIVE THERMAL EXPANSION IN YFe(CN)6	[Gao-17]
2018	D. Grandjean KU Leuwen (Be)	ORIGIN OF THE BRIGHT PHOTOLUMINESCENCE OF SILVER CLUSTERS CONFINED IN LTA ZEOLITES	[Gra-18]

The balance between purely users' publications and publications co-authored by the staff is resumed in Figure 27

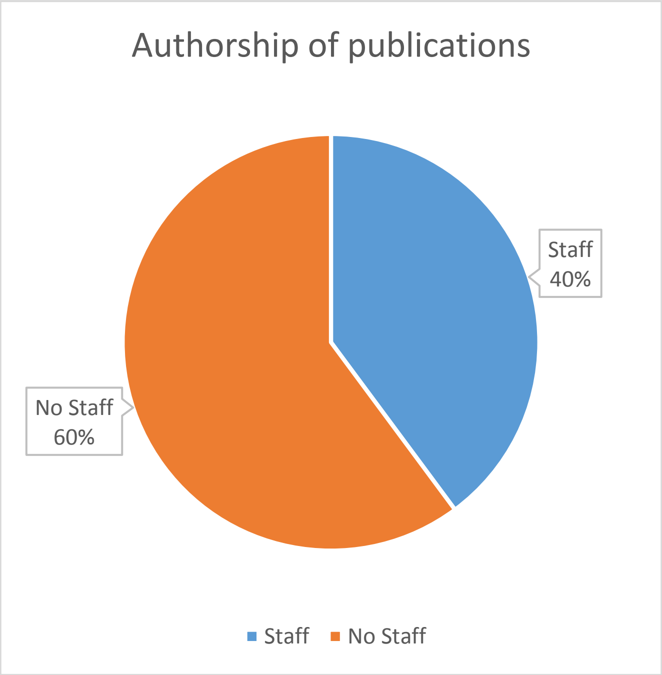

Figure 27: Authorship of publications at LISA.

The staff has co-authored about 40% of the total publication, revealing a considerable collaboration between the LISA scientist and the users.

4. Perspectives

At Dec 2018 the beamline was complete and operative. In order to use the beam from the new EBS ring it will be necessary to move all the equipment outwards by several tens of mm. The new source will be 3m upstream and this would impact the focal position. However this has already been taken into consideration during the design phase and the focal point will move upstream to the centre of the bench. Considering the reduced size of the beam and its considerable stability in time and energy a number of possible evolutions of the present experimental setup could be envisaged.

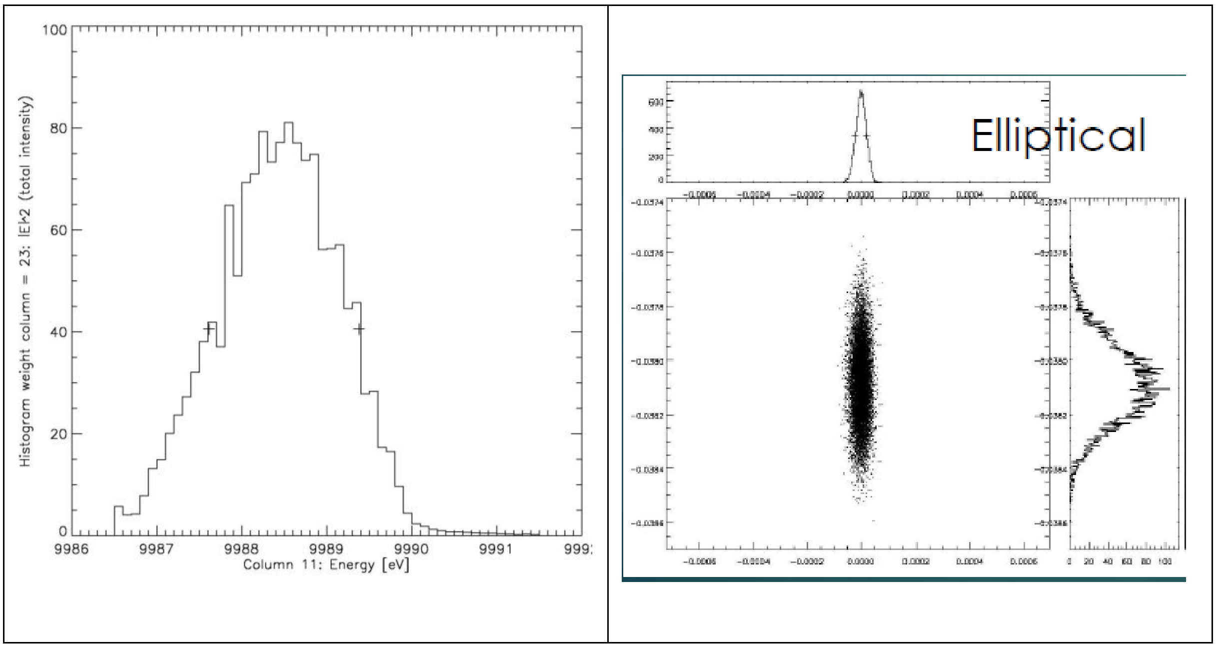

Figure 28: Left: Calculated energy resolution for a crystal analyzer using for focal spot of LISA (see text). Right calculated focal spot of a KB mirror assembly for microfocusing.

4.1 Crystal analyser for X-ray Emission spectroscopy

A possible evolution could be the installation of an emission spectrometer for the collection of XAS data at high energy resolution or for X-ray Emission Spectroscopy (XES). This could reduce the background from the sample and permit an easier data collection on systems with overlapping emission lines or overwhelming inelastic emission. A test calculation (SHADOW code, [San-11.2]) has been carried out considering a Ge(331) bent crystal analyser in Johansson geometry (bending radius R=105 cm) with a 20 × 30 mm^2 area and using the LISA calculated focal spot as source. The resulting energy resolution at about 10 keV is shown in Figure 28, Left. Calculations show that the analyser would exhibit a FWHM resolution of 1.8 eV and the flux on the detector coming from an hypothetical sample loaded with 10^{17} Hg/cm^2 (30 μg/ cm^2) would be 2 kcps (Si(111) monochromator). This would make possible XES analyses on *bulk* and *moderately diluted* samples and the dilution limits could be further pushed by using a multicrystal analyser.

4.2 Microfocus station

Taking into account the exceptional electron beam parameters for EBS and the fact that the Single Bend provides a clean beam with no spurious emissions it would be interesting to install a microfocus station (namely a Kirkpatrick-Baez assembly, KB) at LISA. The station could be installed in EH1 (41 m from the source) and run in the configuration without mirrors in order to keep the maximum brilliance from the source. A calculation with the SHADOW code [San-11.2] was carried out considering elliptic Pt coated mirrors of 30 cm length and incidence angle 8mrad. Using a moderate defocusing (namely, 20:1 leaving a space of about 2m between the mirrors and the focal point for the experimental setup) a beam of 1 (7) × 3(8) μm would be obtained (Figure 28, Right) with an intensity at 10 keV with the Si(111) monochromator of 9× 10^9 ph/s. The uncertainty on the size comes from different estimations of the shape error. Such a beam could be profitably used for microXAS or surface mapping.

5. Selection of five highlight publications

Here we list the 5 highlight publications that have been selected for fulfilling a number of *quality criteria* like impact on the community, reputation of the journal and use of unique features of the beamline. The journal Impact factor (IF) has been taken from the https://www.scijournal.org/ site whereas the number of citations is updated at Mar 21 2019 using *Clarivate Web of Science* as source.

Authors	Title	Journal	IF	Cit.
A. Minguzzi et al.	Observing the oxidation state turnover in heterogeneous iridium-based water oxidation catalysts	Chem. Sci., 2014, **5**, 3591	9	68
S. Pollastri et al.	The chemical environment of iron in mineral fibres. A combined X-ray absorption and Mössbauer spectroscopic study	Journal of Haz. Materials **298** (2015) 282	6.5	28
H. A. Miller et al.	A Pd/C-CeO_2 Anode Catalyst for High-Performance Platinum-Free Anion Exchange Membrane Fuel Cells	Angew. Chem. Int. Ed. 2016, **55**, 6004	12	53
F d'Acapito et al.	Evidence for Germanene growth on epitaxial hexagonal (h)-AlN on Ag (111)	J. Phys.: Condens. Matter **28** (2016) 045002	2.6	35
D. Grandjean et al.	Origin of the bright photoluminescence of few-atom silver clusters confined in LTA zeolites	Science **361**, (2018) 686	41	3

These articles are available in Appendix 1

6. Recommendations of the previous Beamline Review Panel

The latest Beamline Review Panel (who evaluated the beamline activity in May 2014), although recognizing a high level of research carried out at GILDA, pointed out a severe lack of investments in the preceding years. For this reason, the panel emitted three recommendations (defined in the report as *mandatory*) related to the X-ray optics refurbishment:

"The 1st development priority is the purchase of a new monochromator with state of the art technology that is consistent with the level required by the future upgrade of the ESRF machine."

LISA has been equipped with a monochromator with state-of-the-art performance. The present device has thick and flat crystals in order to minimize the mechanical stress and improve the energy resolution; moreover the 'double rotation axis' scheme for crystals has been abandoned for a more conventional 'single rotation axis'. The new monochromator is cooled via liquid nitrogen resulting in a considerable stability. The temporal variability of the crystal angular scale at long term (>2 days) is now of the order of 1 μrad, a value at the top of the present technology.

"The installation of a new collimating mirror with appropriate mechanics and cooling to deal with the new source will optimize the energy resolution and flux available for X-ray Absorption spectroscopy. This is the 2nd priority."

The new 1st collimating mirror has been installed and the tests presented in Sec 1.4.1, and in particular in Figure 7, demonstrate the compliancy with this request. The device is equipped with a motor for the optimization of the radius of curvature and this has a considerable effect on the energy resolution as demonstrated in the picture. The presence of this mirror permits to use vertical slits wide open (up to 2mm) so maximizing the flux (see Figure 9) keeping a theoretical value for the energy resolution (Figure 8). Changing slightly the radius of curvature will allow to optimize the energy resolution in the new configuration of EBS for which a source more distant by 3m is foreseen. The mirror exhibits 2 coatings, one with Platinum for energies above 15 keV and the other with Si to work below 15 keV.

"For further increase of the flux and stability at the sample position that is necessary for planned scientific cases (2D mapping, ReflEXAFS, etc..) we recommend the installation of a second toroidal focusing mirror downstream of the monochromator as the 3rd priority. "

Actually the use of the sagittally focusing monochromator in the GILDA optical scheme resulted in a very inhomogeneous beam in the focal spot with a marked horizontal displacement upon energy changes. For this reason we adopted the solution of toroidal mirrors that provides a highly spatially homogeneous beam (see Figure 10b) with a barely detectable shift with energy. Also in this case the mirror has two toroidal channels, one per coating in order to optimize the harmonic rejection level. First results on 2D elemental mappings and grazing incidence spectra confirm the effectiveness of this solution.

Additional recommendations of the panel:

"The panel encourages the beamline team to continue the expansion of, and diversity in the user community to enhance the opportunities for long term development projects."

In the last period we have considerably increased the activity in the environmental science field mainly due to the arrival of dr G. Lepore who had a solid background in the field. Also the access scheme of users has been changed by introducing Block Allocation Groups consisting in projects of up to 6 days of beamtime per semester during up to 2 years. Three groups has benefited from this program with encouraging results and the scheme will be repeated after the restart.

"In particular high count rate fluorescence detection is a significant pressing need that is common to the majority of the research fields."

"[We recommend (…)] the purchase of a new multi-element fluorescence detector and associated data acquisition electronics as the top priority."

Through a partnership with Politecnico di Milano and INFN-LNF (ARDESIA project) we have tested and installed on the beamline a 4 element Silicon Drift Diode detector (Sect 1.5.3 and Figure 15 right) that has been extensively used in several experiments. This prototype will remain at LISA available for all users. Unfortunately, the lack of the third tranche of funds (0.5M€ in 2016) has prevented us from completing the refurbishment of the experimental part of which the detector electronics is a fundamental part.

"If sufficient funding can be obtained we then strongly recommend a significant refurbishment of the end station including (i) a flexible sample space suitable for multi technique measurements such as XAS+ XRD as well as in situ or operando studies, (ii) a reliable sample positioning and manipulation system to facilitate mapping and grazing incidence experiments, (iii) the possibility to include specialist beam conditioning equipment (poly-capillary optics) "

The first recommendation has been fulfilled with the realization of a new experimental hutch (merging the old hutches #2 and #3 of GILDA) now offering a wide space for multi-technique analyses and a new bench supporting the experimental apparata (see Figure 14: Sketch of EH2. Picture from [Dac-19]. Reproduced with permission of the International Union of Crystallography.Figure 14). The remainder of the recommendations was not fulfilled due to lack of funds.

"It is important to note the successful implementation of these two investment phases will at the very least require additional 'peak load' technical staffing support during installation and commissioning periods, whilst the subsequent beamline operations will require additional scientific staff support if efficient operations are to be achieved. Specifically we would recommend the recruitment of first a technician and then an additional scientist."

For what concerns the staff the scenario, though being far from ideal, has improved in the latest years with the presence of a stable resident staff (one responsible plus two post docs, see Figure 19). It has not been possible to recruit personnel with a permanent position for a technician and/or a scientist but technicians from the neutron group of OGG (A. Laloni, who later left for ESS) and the Trieste site (A. de Luisa, A Martin) helped in realizing targeted tasks.

7. Overview of the overall scientific activity

7.1 Earth and Environmental Sciences

Giovanni Orazio Lepore - CNR-IOM-OGG, Grenoble (France)

During the last five years, several studies with impact on Earth and Environmental Sciences and related fields have been performed in LISA using X-ray absorption spectroscopy (XAS) techniques. Studies were carried out in many of the domains with which earth and environmental sciences traditionally deal with. In this chapter, the main contributions to this field, divided into 5 thematic sections, are reported.

Earth Science studies have been dealing with classical crystal-chemical problems such as cation ordering and trace-metal incorporation mechanisms as well as oxygen fugacity conditions during rocks and minerals crystallization. Specific attention has been payed to the study of geomaterials with technological implications. A great number of works discussed the environmental implications of the presence of toxic elements in sensitive matrices; likewise, LISA users community has put interest in the investigation of element speciation in dust deposits of both natural and anthropogenic origin. Finally, the bio-geo interface has been the object of several investigations, regarding both geomaterials effects on human health and bio-mineralization phenomena.

Most of these studies benefited from the high photon flux (≈10^{11} ph/s using Si(111) crystals) and the availability of a HP-Ge multichannel fluorescence detector, since they often had to deal with very diluted elements, frequently included in quite heavy matrices. An important feature of LISA that allows to perform a great number of studies in earth and environmental studies is the wide energy range attainable (4-70 KeV), which covers most elements heavier than Ca. X-ray Absorption Near-Edge Structure (XANES) studies, in particular those exploiting pre-edge features, took advantage from the high energy resolution of the Si(311) monochromating crystals.

7.1.1. Earth Science

A series of studies has addressed issues in the field of fundamental earth science and mineralogy by investigating minor to trace element redox state and local structural environment.

[Cic-15] and [Sta-17] performed a series of reduction experiments on synthetic silicate glasses in order to investigate the dependence of iron on oxygen fugacity and alkali atomic ratio [Na/(Na+K)]. Knowledge of the oxidation state of iron in silicate melts represents indeed a relevant tool to comprehend magmatic processes and understand some of the properties of iron-bearing glasses. Variation of the relative abundances of iron species may affect Fe-O distances and bond strengths, affecting melt and glass properties including density, polymerization and viscosity. Iron oxidation state and coordination geometry have been inferred by Fe K-edge XANES spectroscopy. The results provided by [Cic-15] and [Sta-17] highlighted the important role of [Na/(Na+K)] ratio in controlling the [Fe^{2+}/(Fe^{2+}+Fe^{3+})] for any oxygen fugacity condition (Figure 29).

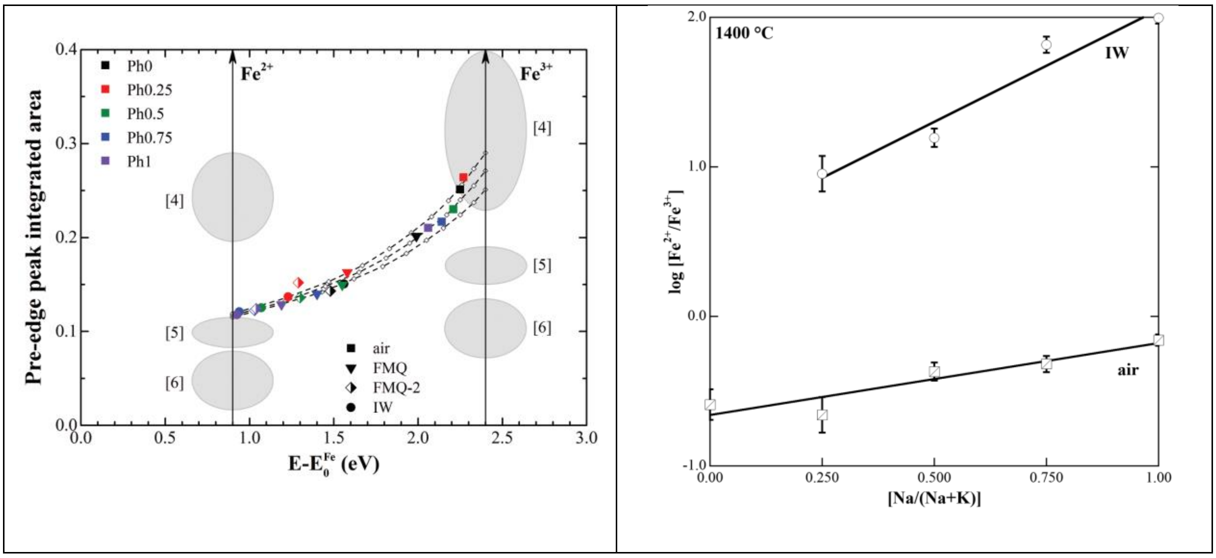

Figure 29: ***Left:*** *plot of the pre-edge peak integrated area vs. centroid energy position for all the glasses synthesized at HT and at different redox conditions (air, FMQ, FMQ-2, and IW). At constant oxygen fugacity, the [Na/(Na+K)] ratio has a strong effect on the* Fe^{3+}/(Fe^{2+}+Fe^{3+}) *ratio.* ***Right:*** *The log[*Fe^{2+}/Fe^{3+}*] vs. the [Na/(Na+K)] ratio for samples synthetized at HT at oxidizing (air) and reducing conditions (IW). By increasing the K content in the glasses, both at oxidizing and reducing conditions, there is an increase of ferric iron. Pictures from [Cic-15].*

This kind of information is crucial for the implementation of models that predict the viscosity and the redox state of natural melts at geological conditions, where iron is usually treated as a single species without taking into account variable valance states.

[BenF-16], with the aim of building a framework that could be used to analyze compounds with unknown structure, carried out a systematic study on a set of vanadium-bearing model compounds, representative of the most common V coordination geometries and oxidation states. Data were analysed by means of XANES calculations in the full multiple scattering (FMS) framework.

In order to infer the role of water circulation during the metasomatic process and amphibole formation, [Bon-14] characterized a series of amphiboles by means of single-crystal X-ray diffraction, XAS, electron microprobe and secondary ion mass spectroscopy; pre-edge peak analysis at the Fe K-edge allowed to fully assess the state of dehydrogenation of the samples.

[Mar-18], investigated the structural transition *Pbca*→*Pca*2_1 of bornite (Cu_5FeS_4) below 65 K with X-ray powder diffraction (XRPD) and extended X-ray absorption fine structure (EXAFS) data collected at low temperature on ID22 and BM08, respectively. Important information on the ordering of Fe atoms at the M4 and M5 sites of bornite were obtained by comparing results on Fe-S bond length distances from XRPD and EXAFS.

[Geo-19] studied the speciation of Tl in (Tl, Sb, As)-rich pyrite through EXAFS analysis at the As and Sb K edge and Tl L_3 edge. They found that Tl, Sb, and As occur as Tl^+, Sb^{3+}, As^{3+}, and As^- with Tl displaying a wide range of coordination numbers (≈3 to ≈6) and bond distances (2.98-3.16 Å), revealing the occurrence of different local environments. The study indicated a disordered Tl local environment, suggesting that Tl may be hosted in structural defects lacking long-range order.

7.1.2. Geomaterials

Many minerals and related inorganic compounds are basic materials for technological applications. During the last years, a global concern has grown over the long-term availability, and the secure supply of certain raw materials employed in technological applications. [Dib-16] described synthesis and structural characteristics of nanocrystalline powders of Fe-bearing kuramite ($Cu_{3-x}Fe_xSnS_4$), promising material for solar cell applications. The material was obtained through a mild, environmentally friendly and scalable solvothermal approach, thus fulfilling the need of reducing the footprint and the energy costs for production. XANES measurements allowed assessing Sn and Cu valence state that resulted to be tetra- and mono-valent, respectively.

[Gua-15] investigated the potential use of a laterite from Togo as a raw material for low-temperature geopolymers preparation using both phosphoric acid and alkaline sodium silicate solution. Structural and mechanical properties were measured; pre-edge peak analysis at the Fe K-edge (Figure 30) evidenced changes in the chemical and structural environments of iron following thermal treatment of geopolymers.

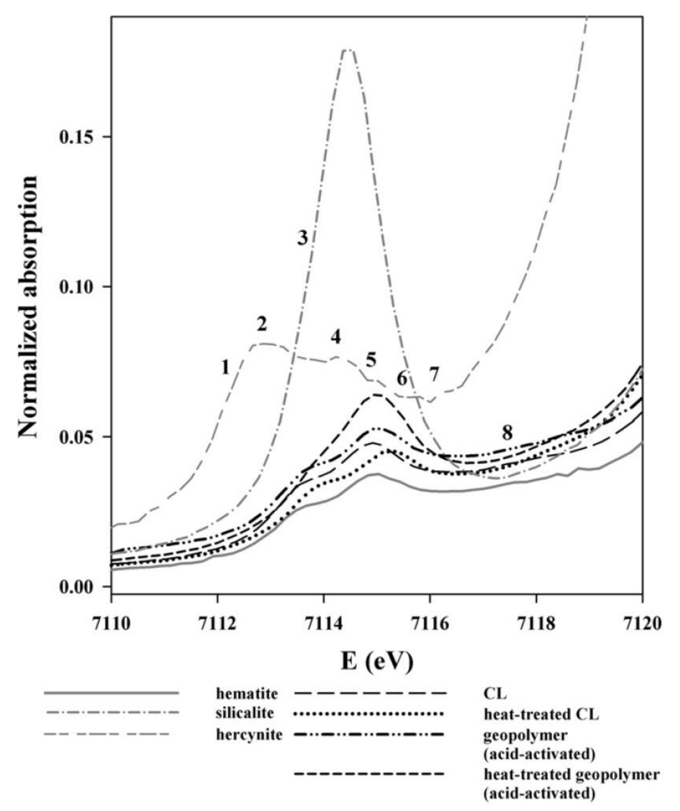

Figure 30: Normalized pre-edge peak of the XANES region of calcined laterite (CL) and geopolymer (acid-activated) as well as the corresponding heat-treated samples. In addition, reference spectra of hematite, hercynite and silicalite are also shown. Picture from [Gua-15].

These changes indicate interaction between the geopolymer structure and iron during heating, possibly leading to redox properties. The results of the study indicate that these laterite-based geopolymers could be a green alternative to Portland cement; moreover, they could represent economically viable alternatives in developing countries where this raw material is readily available.

7.1.3. Contaminants in environmentally sensitive matrices

The presence of naturally occurring toxic/polluting elements, asbestos and mineral fibers and other contaminants can make exposure to water, soils and rocks hazardous. Due to natural causes or anthropic factors, such phases may be disseminated in the environment, resulting in contamination of soil, water and air media with a consequent risk for human health. Several studies have been conducted in this topic; most of them dealing with the identification of valence state and speciation of As in mineralogical hosts, groundwater and sediments.

Arsenic, a well-known environmental carcinogen, is subject to a variety of mobility-altering processes. A wide range of studies has thus been dedicated to investigate the mobility of arsenic in natural media.

[Kan-14] studied the effects of redox reactions between an As-rich pyrite and aqueous Se^{4+} as a function of reaction time and ferrous content in the pH range 5.05–8.65 using XANES and EXAFS analyses at both Se and As K edge. They found that reduction to Se^0 occurs at all the studied pH values and that oxidation of As-rich pyrite by aqueous Se^{4+} involves multiple complex and concurrent reactions.

[Pha-17], [Pha-18] and [Pha-19] focused their attention on the impact of As contamination on the Mekong delta area, where As concentrations exceeding 1600 ppb in groundwater can be found, taking into account how different redox conditions may affect As distribution. [Pha-17] analysed the relationship between the electrical ground conductivity and As distribution. Linear Combination Fit (LCF) of As K-edge XANES spectra showed that As was present as both As^{3+} and As^{5+}, with As^{5+} bonded to Fe oxyhydroxides and As^{3+} to both Fe oxyhydroxides and sulphides and allowed to trace a depth-profile of As speciation in sediments.

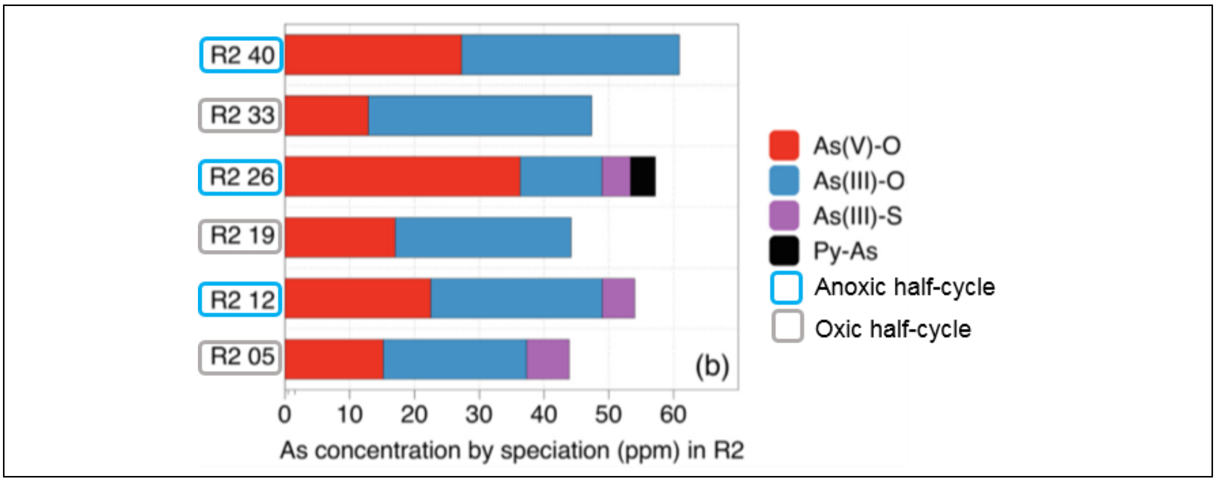

Figure 31: Arsenic quantitative speciation in reactor 2 used during the experiment (1mMSO_4^{2-}) at the end of each anoxic or oxic half-cycles. The quantitative speciation is estimated by multiplying total As concentration in sediments samples by the fraction of each As species as obtained by LCF of As K-edge XANES data. Picture modified from [Pha-19].

[Pha-18] and [Pha-19] studied how redox oscillations, caused by seasonal fluctuations such as monsoons and irrigations, influence As release in aquifers by investigating the As, Fe, and S species generated by oscillating redox conditions in laboratory experiments in automated bioreactors containing As-rich sediments. XANES was exploited to reveal solid-phase As species (Figure 31). [Pha-19] found that: a) As is first released during Fe reducing conditions but is then sequestered during SO_4^{2-} reduction; b) As adsorbs/desorbs on Fe-oxyhydroxides; c) aqueous thioarsenic can form and be adsorbed on Fe sulfide minerals; and d) the reactions leading to the decrease of aqueous As concentrations over subsequent cycles are driven by microbial activity, which induces fermentation during anoxic periods, and respiratory consumption during oxic ones.

[Bia-17] dealt with another important issue concerning Tl contamination in drinking water. Thallium (Tl) is one of the most toxic elements for living organisms. In 2014, Tl contents up to 10 µg/L were detected in drinkable water from the public distribution system of Valdicastello Carducci-Pietrasanta (northern Tuscany, Italy). The study of segments of the pipelines revealed the presence of insoluble Tl_2O_3 aggregates in the rust scales lining the pipeline. XANES and EXAFS studies were able to point out the presence of minor amounts of a more soluble Tl^+ salt, later identified as TlCl by leaching and drying experiments that gave rise to a secondary and unexpected source of contamination.

The speciation of Fe in bulk and suspended respirable quartz dusts coming from ceramic and iron-casting industrial processes was studied by [Dib-14] via XAS. The study lead to the determination of Fe speciation through a coupled analysis of XANES and EXAFS regions at the Fe–K edge and provided marked differences of Fe speciation in bulk quartz powders, collected at different stages of the two production processes, and the corresponding respirable dusts, effectively inhaled by workers, and thus responsible for the silica toxicity.

[Pol-15] performed a systematic structural investigation of iron in asbestos and erionite (considered the most relevant mineral fibers of social and/or economic-industrial importance) using synchrotron X-ray absorption and Mössbauer spectroscopy. [Pol-15] found that iron in the bulk structure is found in octahedral sites and can be made available at the surface via fiber dissolution; on this basis, the authors hypothesized that the amount of hydroxyl radicals, capable of attacking biological tissues, released by the fibers depends upon their dissolution rate.

7.1.4. Metals in particulate matter

Particulate matter (PM, i.e., PM_{10}, $PM_{2.5}$ and PM_1) is considered an environmental concern due to its numerous effects on public health and to its capability of transporting and diffusing a number of pollutants. Small-sized particles remain suspended in the air for long periods, moreover they can travel long distances and recombine with other liquid and gaseous phases in the atmosphere. Consequently, pollution by PM constitutes a highly dynamic phenomenon. A series of experiments was dedicated to the investigation of the role of contaminants in the particulate matter. [Dac-14.1], [Liu-19] and [Pet-19] studied iron speciation of natural and anthropogenic dust. Fe is often one of the most abundant elements in PM, however, the main interest on Fe is associated with the Fenton cycle. Iron is indeed able to act as a catalyst in the formation of radicals and in the generation of reactive oxygen species (ROS) in tissue, possibly provoking an inflammatory response as in the case, for instance, of diseases related to crystalline silica. [Dac-14.1] provided detailed information on Fe species in urban $PM_{2.5}$ from downtown Rome: following EXAFS analysis, Fe resulted to be mainly present at the trivalent state hosted in a nano- or crypto-crystalline form of ferrihydrite. [Liu-19] performed XANES LCF analyses on insoluble dust in snow from the Laohugou No.12 glacier (China) and in sand from the glacier deposits finding an altitude effect on the Fe speciation in the snow. [Pet-19] characterized iron speciation and local structure for two well-known atmospheric aerosol types: Saharan dust and steel production plant emissions. Through a coupled XANES-EXAFS approach, the authors were able to successfully distinguish peculiar features of Saharan dust, which results to be mainly constituted by aluminosilicates and iron oxyhydroxides, and steel production emissions, where spinel-like oxide phases are predominant.

[Val-17] studied The Cu, Zn, and Sb speciation in road dust samples by means of LCF analysis, using both conventional stoichiometric and environmental standards, such as environmental certified reference material or samples of tyre, brake pads, and soil collected in the same location as dust samples. This approach allowed obtaining fine information on metal speciation, highlighting differences among similar samples, thus indicating the chemical processes leading to the presence of Cu, Zn, and Sb and their sources.

7.1.5. Bio- Geosphere interactions

In the last years, there has been a reconsideration of the role of biota in influencing geological and environmental processes, aiming at understanding the relationship between physical processes and organisms in different environments. Indeed soil, surface and ground water can be, as also pointed out by some of the contributions described in the previous paragraph, seriously compromised in areas affected by mining and industrial activities and intensive farms and breeding. The development and evaluation of eco-friendly and cost-effective “green” methodologies employing bio-geo materials for the restoration of soil and water quality requires a multidisciplinary approach encompassing geoscience, agronomy and engineering.

The dispersion of metals in the environment has straightforward implications in agriculture, since metals can accumulate in crop organs. In this context, [Mas-14] studied the immobilization and transport mechanisms of Pb in some edible crops, with the aim of assessing Pb distribution among plant organs and understanding which compounds are responsible for Pb transport and accumulation in different plant organs. [Mas-14] found that Pb concentrates primarily in roots and secondarily in leaves. By means of XANES analysis, performed at Pb L_3 edge, they were able to identify that Pb immobilization is mainly due to the formation of Pb-histeine complexes and, to a lesser extent, the precipitation of Pb carbonates; on the other hand, Pb transport from roots to upper plant organs was attributed to the formation of Pb complexes with organic acids.

In the same framework, [Eic-14] investigated concentration, distribution, and speciation of selenium in different parts of wheat and Indian mustard, grown in a seleniferous area of Punjab. An extreme enrichment in Se was found in all plant organs, in particular those in the upper plant parts, testifying a high mobility of Se within the plant organs.

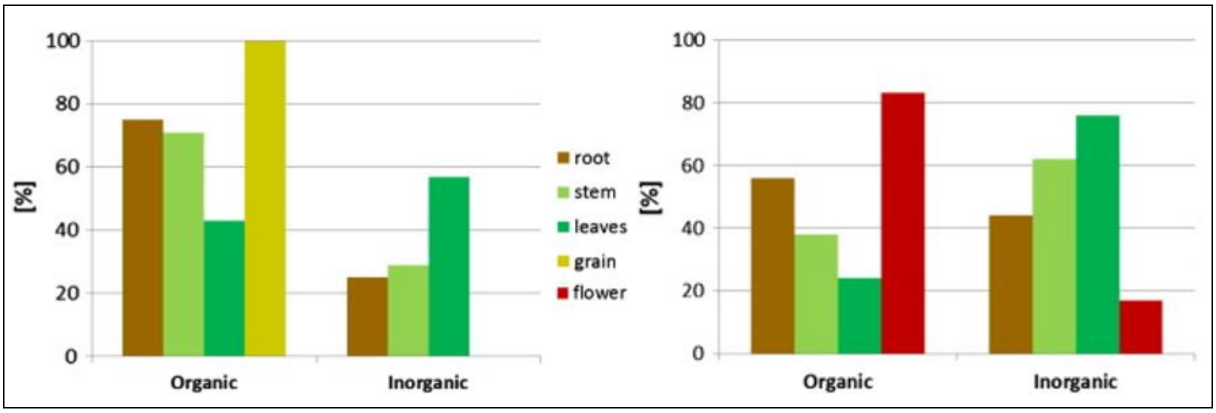

Figure 32: Proportion of organic and inorganic Se species in different plant parts of wheat (left) and Indian mustard (right) based on the results of LCF analyses. Pictures from [Eic-14].

XANES results (Figure 32) indicated selenate and organic Se (mainly Se-methionine) as the main forms of Se taken up by plants; dimethylselenide and methylselenocysteine were produced by plant organs as an active detoxification response. In addition to the generally high Se concentration, these findings highlighted a considerable health risk for human health since a considerable fraction of Se is in a form that is highly absorbable by human and animal metabolism.

Another interesting aspect bonding bio- and geosphere is related to the formation of the so-called biominerals. Biominerals are composite materials containing an organic matrix and nano- or micro-scale amorphous or crystalline minerals; they play fundamental functions for a variety of living organisms and can affect the control of the environmental behaviour and fate of heavy metals and pollutants. However, their reactivity and solubility are poorly understood. [Med-14] and [Med-14.1] performed studies on Zn biomineralizations from the Naracauli stream, Sardinia. By means of a multi-technique approach (XRPD, scanning and transmission electron microscopies, and XAS), [Med-14] obtained structural information on amorphous Zn biominerals that allowed to highlight significant differences with respect to other Zn biomineralizations found along the same stream. These differences were hypothesized to be related to local differences in the physicochemical parameters and/or in the microbiological consortia. [Med-14.1] investigated structure and solubility of a set of hydrozincites of different nature: natural abiotic, synthetic, and biominerals using EXAFS and XRPD. They found an increasing disorder from geologic to synthetic to biomineral samples, associated with an increase in unit cell dimensions and a decrease in crystal size. These structural characteristics, mainly the reduction in crystal size, were found to be related to the observed differences in solubility that increased from the geologic sample to synthetic analogues to biominerals.

7.2 Magnetism and Superconductivity

A. Puri, CNR-IOM-OGG, Grenoble (France)

Regarding the research activity on magnetism and superconductivity, the LISA (BM08) CRG beamline at ESRF has been particularly active in the study of thin films and nanostructures containing magnetic elements and in the investigation of superconducting systems. In many cases X-ray absorption spectroscopy (XAS) was employed in conjunction with diffraction and other complementary spectroscopic techniques, as well as imaging and magnetometry, providing crucial information on the local structure around the absorber atom.

The possibility to acquire spectra in fluorescence mode, using linear dichroism to gain information on the anisotropy of a system [Jac-18, Lau-14, Wol-17], the availability of two 13- and 12-element fluorescence HPGe detectors and the ability to work at cryogenic temperatures (20 K), thanks to a cold finger nitrogen/helium cryostat, are the LISA key features which have emerged from the works considered in this report.

7.2.1. Thin films containing magnetic elements/layers

Ultrathin film systems containing magnetic 3d metal (e.g. Co, Fe) interleaved with a non-magnetic material exhibiting tunable magnetization anisotropy, are of particular importance for spintronics as well as for technology of magneto-optical memory devices. A spin reorientation transition (SRT) between in-plane and out-of-plane magnetization was evidenced in Pt/Co/Pt structures when irradiated with ion beams and light pulses of different photon energy. In particular, the ultrafast annealing with optical lasers leads to structural and magnetic changes at the magnetic Co film and its interfaces, without overheating of the substrate, which is important for technological applications. Pt/Co/Pt films of different Co layer thickness, irradiated with extreme ultraviolet (XUV) nanosecond pulses have been investigated by means of X-ray diffraction (XRD), X-ray Absorption Near Edge Structure (XANES), Extended X-ray Absorption Fine Structure (EXAFS) and complimentary techniques [Jac-18, Wol-17]. Both XANES and EXAFS were measured at the BM08 beamline at Co K-edge in florescence mode at 77 K, under ‘grazing’ (75° between the incident beam direction and the normal to the sample’s surface, probing out-of-plane bonds perpendicular to the sample's surface) and ‘normal’ (15°, probing in-plane bonds parallel to the sample's surface) incidence configurations. For each sample the spectra in normal and grazing incidences were very similar, indicating very small anisotropy. The EXAFS analysis confirmed that the irradiation caused significant changes in the local structure around Co atoms, introducing Co-Pt intermixing and the formation of $Pt_{1-x}Co_x$ alloys with different Co concentrations and strain in the layers. The bond lengths and local disorder increased. Moreover detailed EXAFS analysis revealed that the bond lengths in the direction parallel to the layer surface were longer than in the perpendicular one for all irradiated samples, suggesting that the light irradiation caused strain in the layer which contains Co-Pt alloy. Under the same quasi-uniform irradiation conditions, the final $Pt_{1-x}Co_x$ composition was found dependent on the thickness of the as grown magnetic Co film. The structural modifications were accompanied by magnetization changes. The Co-Pt alloys composition in the irradiated layer was found to be correlated with the magnetization remanence.

Another class of materials with interesting properties for magnetic memory devices are the $L1_0$ alloys, which are considered promising systems for future ultra-high-density perpendicular magnetic recording media beyond 1 Tbits per square inch (1 inch = 25.4 mm), owing to their high uniaxial magnetocrystalline anisotropy originating from their peculiar structure of stacking layers, which enables them to be thermally stable even at grain sizes down to 3 nm, as in the case of Fe-Pt alloys, where planes of pure Fe or Pt alternate along the [001] direction (c axis). More interestingly the magnetic anisotropy of these systems, which is strictly correlated to chemical ordering and lattice distortion (in particular the c/a ratio), can be controlled via the addition of a third element to the alloy, for example Cu, that reduces the temperature needed for the $L1_0$ formation. Laureti et al. [Lau-14] employed Cu K- and Pt L_{III}-edge EXAFS in fluorescence mode to characterize $L1_0$ Fe–Pt–Cu thin films synthesized with different Cu content. The measurements were carried out at a temperature of 100 K to reduce the thermal atomic vibrations, using linear dichroism to enhance the sensitivity to differently oriented bonds (Figure 33), which allowed to describe in detail the local atomic environment around the two absorber atoms.

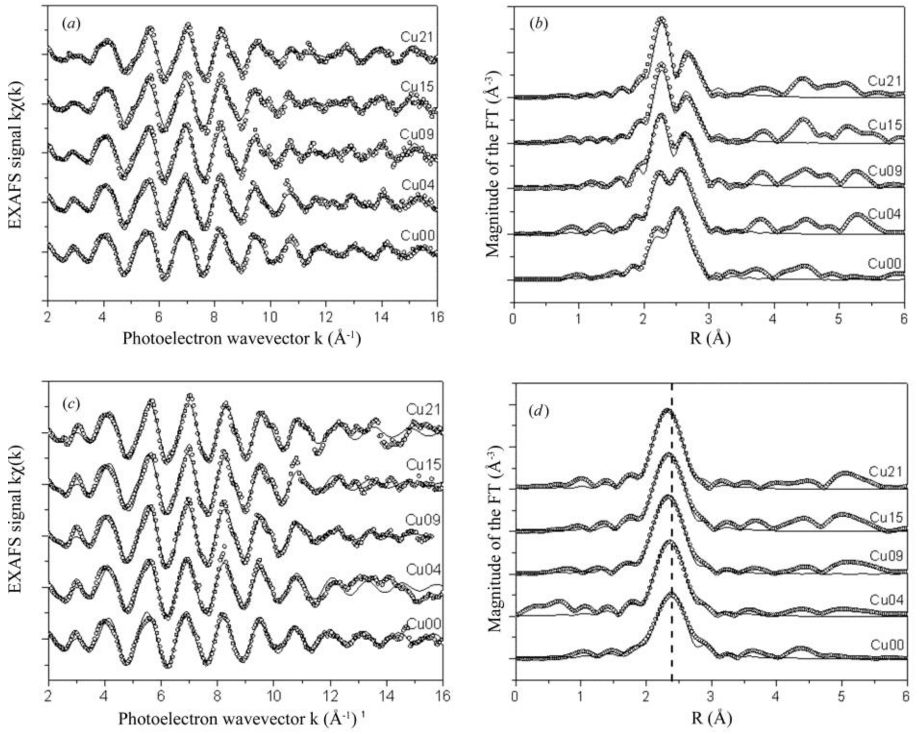

Figure 33: EXAFS signals (left) at the Pt L_{III} edge and the relative Fourier transform (right) obtained in the 'parallel' (90° between the X-ray polarization vector and the normal to the sample surface) (a), (b) and 'perpendicular' (15°) (c), (d) configurations. Experimental data (open circles) and fit (solid lines) [Lau-14]. *Reproduced with permission of the International Union of Crystallography*

The study allowed to distinguish experimentally the effects on the chemical order and lattice distortion induced by the Cu atoms. In particular, it revealed that the chemical order around the Pt atoms was strongly influenced by the addition of Cu atoms, consistent with the variation of the magnetocrystalline anisotropy. On the other hand, the effect of Cu atoms in the alloy was a lattice distortion with a linear reduction of the c/a ratio, although this effect had a minor influence on the magnetocrystalline anisotropy when compared to the effect of the chemical ordering.

Zinc Oxide doped with a transition metal (TM), such as Cu, is particularly interesting because of its room-temperature ferromagnetism (RTFM). However the mechanism responsible for the RTFM in this system is still poorly understood. One of the major questions is whether the observed RTFM is an intrinsic property of the TM-doped ZnO or whether it is due to extrinsic causes such as nanoclustering of the dopant. Thin $Zn_{1-x}Cu_xO$ films synthesized with different Cu doping ($x = 0.02, 0.04, 0.07, 0.10$) have been studied [Vac-16] via superconducting quantum interference device (SQUID) magnetometry, high-resolution x-ray diffraction, x-ray linear dichroism, x-ray circular magnetic dichroism (XMCD), Cu K- and Zn K-edge XAS. The XANES and EXAFS spectra were measured at the BM08 beamline, at 77 K, using the available 13-elements Ge multidetector. Zn K-edge EXAFS revealed a close similarity with a perfect wurtzite lattice, as in pure ZnO, while Cu K-edge EXAFS indicated that the Cu atoms were not incorporated into the wurtzite lattice but were mostly in a CuO-like environment with only a small fraction occupying Zn-substitutional sites at high doping. Even though the samples exhibited room-temperature ferromagnetism with magnetization increasing with Cu concentration, no signatures of local magnetic moments associated with Cu atoms were detected, as evidenced by the lack of any XMCD signal. The results indicated that ferromagnetism of the investigated films was not directly linked to the doping atoms but rather due to some other changes which have been introduced to the host ZnO by the dopants.

7.2.2. Magnetic nanoparticles and nanostructured materials.

In nanotechnology a frontier topic is the realization of multifunctional nanoparticles (NPs) or nanostructures by appropriate combination of different elements of the periodic table, in which different properties are achieved by a fine control of nanomaterials structure and composition. Very interesting is the case of magnetoplasmonic materials, where a noble metal with excellent plasmonic response, such as gold and silver, coexists with a metal with magnetic or catalytic properties such as transition metals (Fe, Co, Ni, Ti, Rh) or other "non-plasmonic" noble metals (Pt, Pd). Nanoparticles composed by two immiscible elements, Fe and Ag, have been synthesized by laser ablation in liquid solution [Ame-15]. The NPs have been characterized by transmission electron microscopy (TEM), x-ray photoelectron spectroscopy (XPS), XRD, Mössbauer spectroscopy, Fe K-edge EXAFS and magnetization measurements. The EXAFS spectra, collected in fluorescence mode at BM08 with a 13-element Ge fluorescence detector, indicated that iron was present mostly in metallic form as disordered Fe-Ag alloy domains and partially in the oxidized state. The NPs had an innovative structure composed by a scaffold of face centered cubic metal silver embedding metal iron as dopant in disordered silver-iron alloy domains, all arranged in a truffle-like morphology. Fe-Ag NPs showed both the plasmonic properties of silver and the magnetic response of iron-containing phases.

Thin Au-Co bimetallic films have been produced via magnetron co-sputtering and characterized by XAS at Au- and Co-edge measured at BM08 in fluorescence mode, using a 12-element HP Ge detector [Mau-18.2]. The samples were cooled at 80 K using a liquid nitrogen cryostat to reduce thermal vibrations. The results clearly indicated the formation of a full-metallic layer composed for the major part of a binary Au_xCo_{1-x} alloy, and for a minor fraction of segregated metals, also suggested by transmission electron microscopy analysis. Further XMCD analysis at Au $L_{2,3}$ edges carried out at the ID12 beamline at ESRF showed that the Au atoms acquired a net magnetic moment whose estimated orbital components were slightly higher for the film of balanced composition. The magnetic characterization [Chi-17] revealed an unexpected hysteretic behavior characterized by in-plane anisotropy and crossed branches in the loops measured along the hard magnetization direction. The hysteretic features have been qualitatively well reproduced by micromagnetic calculations performed for a simplified system composed of a AuCo matrix surrounding a Co cluster, provided that the two phases had almost orthogonal anisotropy axes.

The addition of 3d transition metals, like Fe, to particles and ceramic structures of nonreducible metal oxides gives rise to a variety of functionalities used in industrial applications such as catalysts and functional ceramics. Niedermaier et al. [Nie-17] were able to produce MgO nanocrystals with iron atoms trapped inside, via a gas-phase-based synthesis approach. After thermal annealing in vacuum, they combined structure characterization techniques (X-ray diffraction and transmission electron microscopy) with X-ray absorption and Mössbauer spectroscopy, to track the valence state and local chemical environment changes of Fe ions inside the nanocrystals as a function of the annealing temperature. The admixed iron ions were found to completely transform into ferric iron (Fe3+). Fe K-edge EXAFS measured at BM08 in transmission mode evidenced that thermal annealing induced a decrease of the local symmetry of the octahedrally coordinated iron ions. This was attributed to complexation with Mg2+ vacancies, i.e. the formation of Fe3+−Mg2+ vacancy clusters. Moreover, clear evidence was found for clustering of Fe3+ ions and their segregation into the nanoparticle surface.

The lanthanide titanates $Ln_2Ti_2O_7$ with the pyrochlore structure are considered promising dielectric materials, catalysts, solid electrolytes and radiation absorbers. These systems are very interesting because, depending on lanthanide cations, the long-range ordered ground state is frustrated, resulting in novel short-range ordered alternatives, such as spin glasses, spin ices, and spin liquids. The structure of these complex oxides is strongly affected by the crystallite size; if the size is small (less than 3 - 5 nm), the local structure, which determines some important electrophysical and optical properties, differs from the crystal one. For this reason the information about the local structure in addition to the crystal structure parameters is important to understand the properties of these systems. Popov et al. [Pop-18] investigated the process of crystallization and local atomic structure rearrangement during the formation of

$Ln_2Ti_2O_7$ (Ln = Gd, Tb, Dy) samples prepared by calcination of initially amorphous precursors at various temperatures, trough EXAFS and XANES spectroscopy at the K-Ti (4966 eV), L_3-Gd (7243 eV), L_3-Tb (7514 eV) and L_3-Dy (7790 eV) edges, together with X-ray powder diffraction and complementary spectroscopy techniques. The XAFS-spectra were acquired in transmission mode with high signal-to-noise ratio up to 16 $Å^{-1}$. EXAFS and XANES spectroscopy provided the sensitive indicators of changes in $Ln_2Ti_2O_7$ local crystal and electronic structure upon amorphous to pyrochlore transition. In particular the EXAFS-FT spectra at the *Ln* L_3-edge showed significative changes on going from the amorphous state to the pyrochlore-type crystalline phase. In fact an explicit splitting of the first coordination shell into 2 components, corresponding to 2 shorter Ln-O and 6 longer Ln-O bonds has been observed. Moreover the K-Ti pre-edge region of XANES spectra exhibited very strong changes, reflecting the local electronic structure rearrangements in $Ln_2Ti_2O_7$, which accompany the crystallization process from initially amorphous precursors (Figure 34).

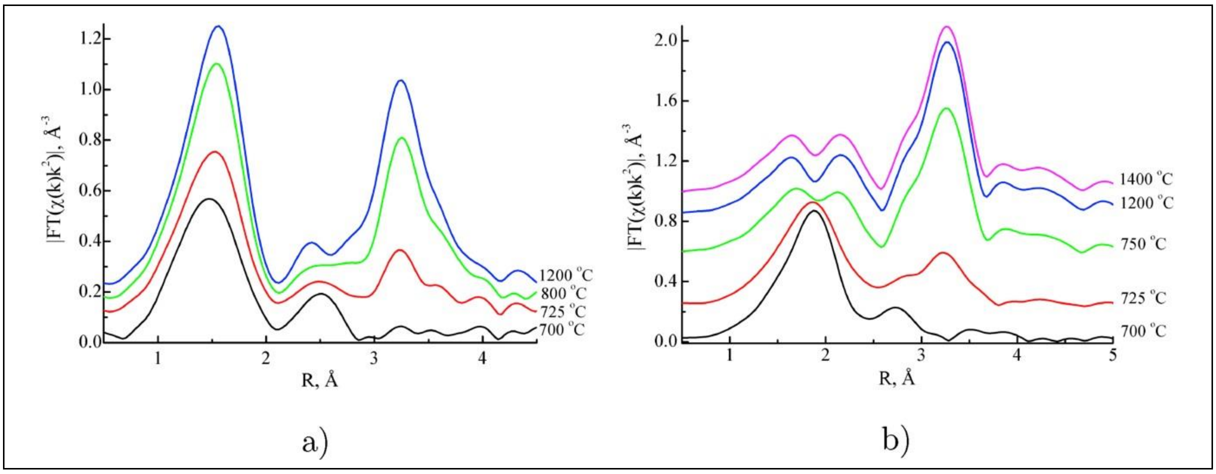

Figure 34: FT modulus of XAFS spectra at K-edge of Ti (a) and L_3-edge of Ln (b) for $Dy_2Ti_2O_7$ synthesized at different calcination temperatures [Pop-18].

7.2.3. Superconducting systems

Bismuth-based layered dichalcogenides, namely $REOBiS_2$ (RE = rare earth) have been drawing a large amount of attention due to their superconducting and thermoelectric properties. The crystal structure of these materials is based on alternate stacking of electronically conducting BiS_2 layers and insulating block REO layers. In these systems superconductivity is generally introduced by substitution in the REO layer injecting charge carriers in the BiS_2 layer hosting superconductivity. In addition to the charge doping, the local structure optimization is an important parameter for the superconductivity of these materials. To explore the interplay of charge and structural degrees of freedom, a new superconductor, namely $Eu_{0.5}La_{0.5}FBiS_{2-x}Se_x$, was synthesized by cosubstitution in REO layer and BiS_2-layer. The superconductivity phase diagram and crystal structure of this compound are shown in Figure 35-1. For small Se substitution (x = 0.0 and 0.2), filamentary superconductivity with a lower transition temperature (T_c) is observed while the bulk superconductivity appears for x > 0.6.

The effect of Se substitution on the Eu valence in $Eu_{0.5}La_{0.5}FBiS_{2-x}Se_x$ has been studied [Miz-17], using Eu L_3-edge XANES (6977 eV), measured at BM08, combined with x-ray photoelectron spectroscopy (XPS). The Eu has been found in the mixed valence state with coexisting Eu^{2+} and Eu^{3+} (Figure 35-2). The average Eu valence showed a significant decrease with increasing Se substitution, suggesting a decrease in the electron carriers; however Bi *4f* XPS results revealed a small increase in the carrier density in the $BiS_{2-x}Se_x$ layers by Se substitution. From the combined analyses, it has been proposed that the Eu-valence may not have a simple correlation with charge doping in the BiS_2-layer, and Se substitution acts mainly on the carrier mobility due to the reduced in-plane disorder.

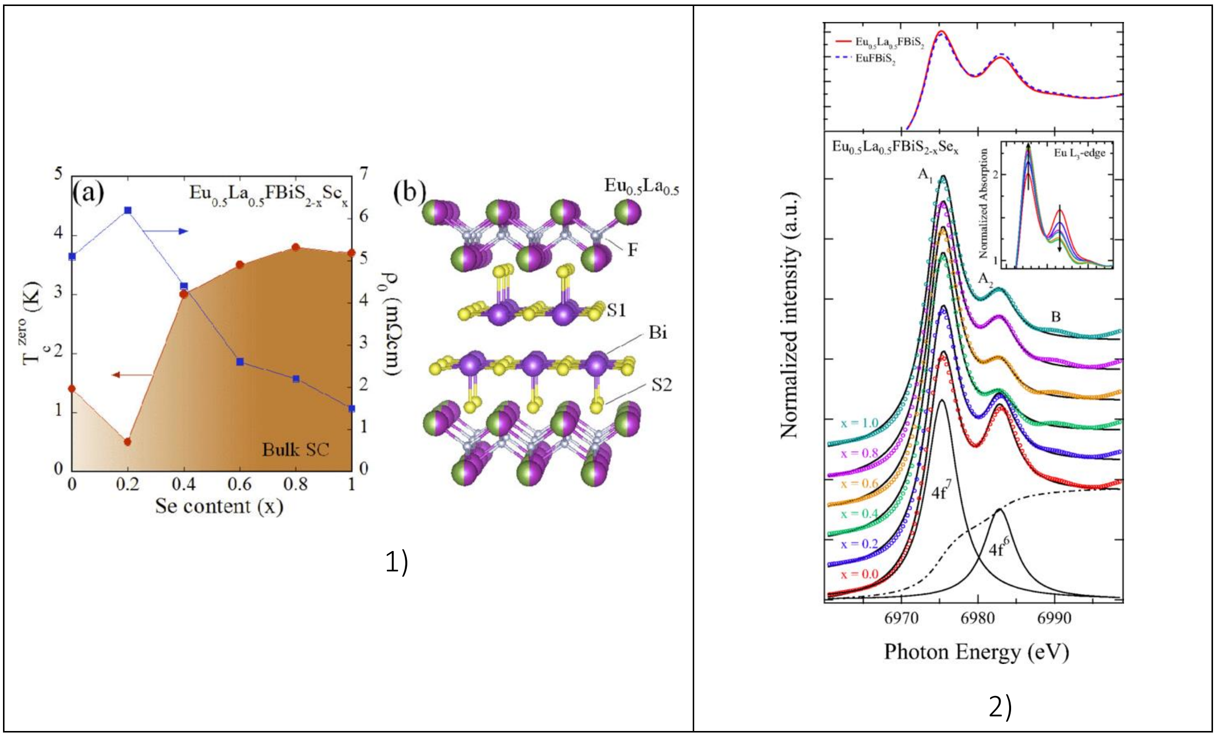

1)

2)

Figure 35: 1): (a) Superconductivity phase diagram of $Eu_{0.5}La_{0.5}FBiS_{2-x}Se_x$. The right axis shows the resistivity ρ_0. (b) Crystal structure of $Eu_{0.5}La_{0.5}FBiS_{2-x}Se_x$ is schematically shown for x=0.0. S1 and S2 denote the in-plane and the out-of-plane chalcogen sites [Miz-17]. 2): (bottom) Eu L_3-edge normalized XANES spectra of $Eu_{0.5}La_{0.5}FBiS_{2-x}Se_x$. The spectra are shown deconvoluted (solid curves) in two Gaussian components corresponding to $4f^7$ (Eu^{2+}) and $4f^6$ (Eu^{3+}) after background (dash-dotted curve) removal. The inset shows a close-up of the Eu L_3-edge XANES white line peaks. (top) Eu L_3-edge XANES white line peaks of $EuFBiS_2$ (dashed line) are compared with those of $Eu_{0.5}La_{0.5}FBiS_2$ (solid line) [Miz-17].

A study of the correlation between local structure and superconductivity in 122-type palladium arsenides with different T_c's has been conducted by Terashima et al. [Ter-18]. A systematic temperature-dependent investigation using As K-edge EXAFS has been performed on $BaPd_2As_2$ and $SrPd_2As_2$ at the Spline beamline, while the same type of measurements were also carried out at BM08 on an intermediate compound, $CaPd_2As_2$, from 20 K to room temperature. The study revealed marked differences in the mean square relative displacement of the As-Pd bonds of the systems for both static disorder and bond stiffness determined by the related Einstein temperatures.

7.3 Glasses

Francesco d'Acapito, CNR-IOM-OGG, Grenoble (France)

XAS is an ideal technique for the study of glasses as it does not require long range order. It is noticeably the short range order the main topic of the study of glasses with XAS. The cases involving glassy materials studied in this period at LISA are relative to 3 main topics: glasses for applications in microelectronics, luminescent glassy materials and fundamental studies on bulk glasses. In many cases the object of the study was a dopant in low concentration and then, the availability of an intense beam and an effective fluorescence detection system (normally the multi-element HP-Ge array) revealed to be of paramount importance.

7.3.1. Glasses for microelectronics

Glassy materials (mostly of the chalcogenide class) are used in microelectronics for the realization of non-volatile memories. In this case the materials are produced as thin films over silicon substrate and for this class of materials the potential of LISA in investigating surface systems via grazing incidence / total reflection techniques has been fully exploited. A series of papers ([Sou-15], [Dac-16.1], [Dac-16.2]) have been dedicated to the depth resolved structural study of Conducting Bridge Random Access Memories. These memories are based on a thin chalcogenide glass (GeS_2 in our case) sandwiched between an inert (bottom) electrode and a top (active) electrode (in our case Ag). By applying an electrical field at the electrodes, atoms from the active electrode migrate to the bottom electrode eventually forming a filament capable to conduct current and realize a low resistance state (*set*) of the memory cell. Applying a reverse electrical field the filament is locally dissolved and the cell falls in a high resistance state (reset). In order to study the diffusion of the top electrode samples have been produced, cycled to create the filaments and then the top electrode was removed. Depth resolved XAS measurements have been realized with the ReflEXAFS technique using the dedicated chamber available at the beamline [Dac-03]. In order to achieve depth sensitivity measurements at different incidence angles (from total reflection condition to full penetration) have been carried out and the data have been analysed in conventional way and with the CARD code [Ben-08] specially conceived for the analysis of ReflEXAFS data at an arbitrary value of the incidence angle.

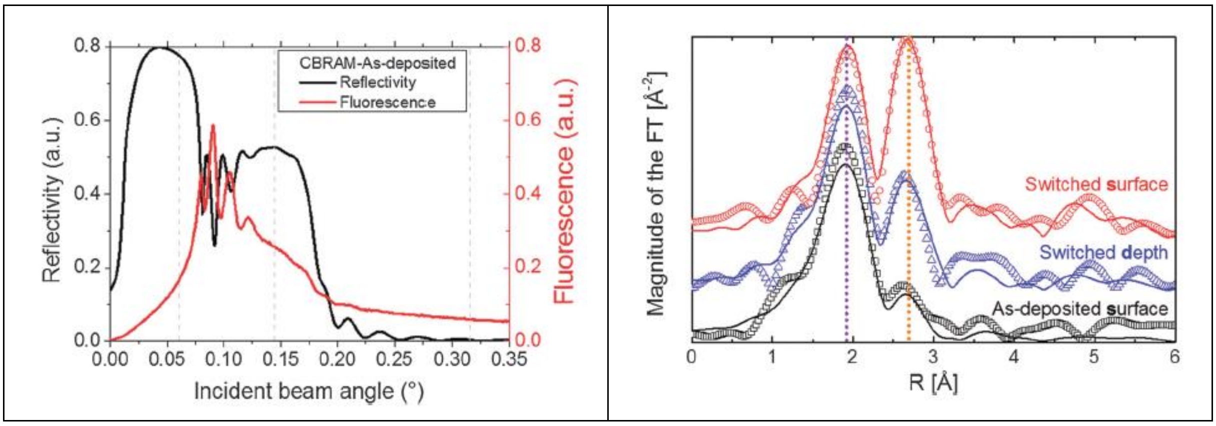

Figure 36: Left: reflectivity of the CBRAM samples (black). The dashed lines mark the angles used for the collection of ReflEXAFS data: surface (0.06°), layer (0.15°), depth (0.32°). Left: the Fourier transforms of the ReflEXAFS data collected at the various angles on as-deposited and switched (i.e. with formed filaments) samples. The peak at almost 2 Å is relative to Ag-S bonds, the following one at about 2.7 Å is related to Ag-Ag bonds. Pictures from [Sou-15].

This study has permitted to describe completely the filament formation procedure. At the beginning Ag ions diffuse in the GeS_2 glass and promptly are reduced to metal again. Indeed the metal content (estimated from the metallic Ag-Ag bonds revealed in the XAS spectrum) is higher near the surface than in the depth. After the forming cycle the filament can reach the inert electrode and realize the low resistivity state. The analysis of the fluorescence from the sample [Sou-15] or reflectivity [Dac-16.1]. The addition of Sb to the glassy film [Dac-16.2] resulted in an increase of the Ag fraction in the metallic state. Sb was found to be strongly linked to S in the glass and not to be influenced by the filament forming cycles. By bonding S atoms it revealed to increase the stability of the metallic state of Ag.

A further application of grazing incidence XAS was a study on thin films of GeTe for the production of Phase Change Memories [Noe-16]. A well-established problem in this class of materials is the “Resistance drift” phenomenon, i.e. the evolution of the resistivity of the amorphous phase towards higher values with time. This is a particularly undesirable phenomenon when seeking to realize multilevel memory cells. The samples analysed were 500nm thick films of GeTe and with different levels of resistivity. Grazing Incidence XAS was used to obtain high quality data avoiding the unwanted effects from the crystalline substrate (mainly Bragg peaks). The XAS analysis permitted to evidence an increase of homopolar Ge-Ge bonds with time linked to the resistivity increase.

7.3.2. Luminescent materials

Oxide glasses doped with rare earth ions have been the object of intense study in the past years at GILDA and then at LISA. A number of these studies have been focused on optic fibre preforms in which the fibre core is only a few hundreds of μm (Figure 41)

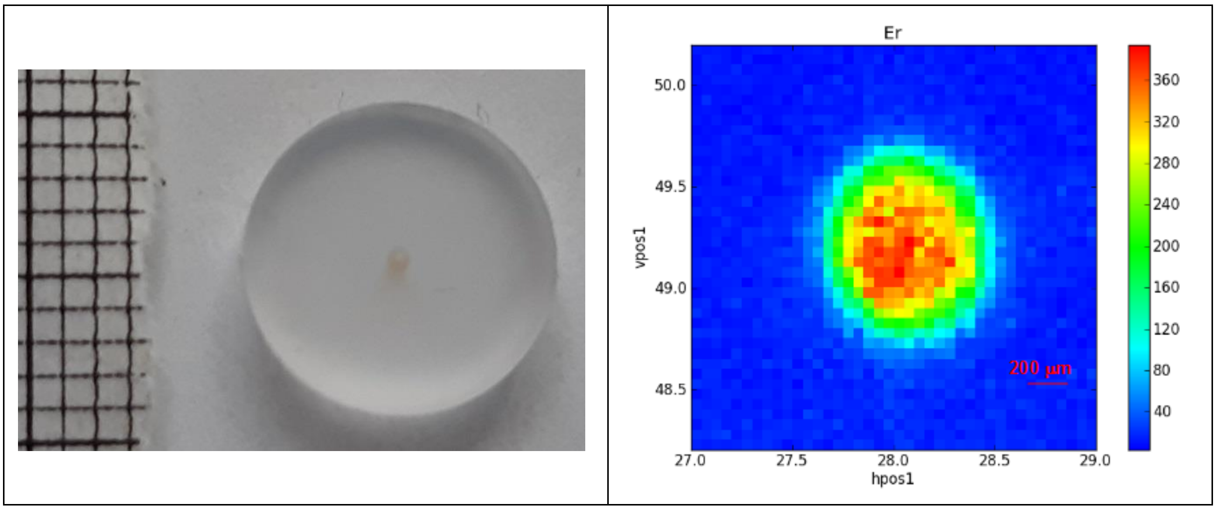

*Figure 37: Left: picture of a typical fibre preform, the core is visible as a darker region inside the glassy cladding. The reference aside has squares of 1mm. Right: X-ray fluorescence map of the core collected with the Er-L_α line. The beam size in this case was 200 * 200 μm^2.*

Making use of the old GILDA optical setup these materials could be investigated only by selecting a thin horizontal fan from the incoming beam, resulting in an intensity of a few 10^9 ph/s with the Si(311) crystal. The new optics of LISA delivers a beam below 200 μm using the full horizontal acceptance and with a Si(111) crystal it is possible to have in the same area a few 10^{11} ph/s with a gain of 2 orders of magnitude. As a consequence a considerable improvement of the data quality is to be expected for this class of materials with the new beamline. The studies presented here, however, are relative to the old GILDA optical scheme. The study presented in [Dac-14] reported about the local order around Er^{3+} ions in optic fibre preforms and in particular the effect of magnesium addition to the glass on the Rare Earth (RE) clustering. Without Mg XAS evidenced the formation of nuclei of $ErPO_4$ structure otherwise not revealed by the analysis with the photoluminescence (due to the extreme limited dimensions of the nuclei). The addition of Mg permitted to avoid the formation of the phosphate nuclei. A further study on optic fibres was about Bi doped systems [Tor-15], [Pau-16]. The aim of this study was to determine the exact valence state of Bi and its local environment. Bi resulted to be in the 3+ state bound to 3 oxygen atoms in a pyramidal configuration (3 oxygens on one side and the Bi lone pair on the other side).

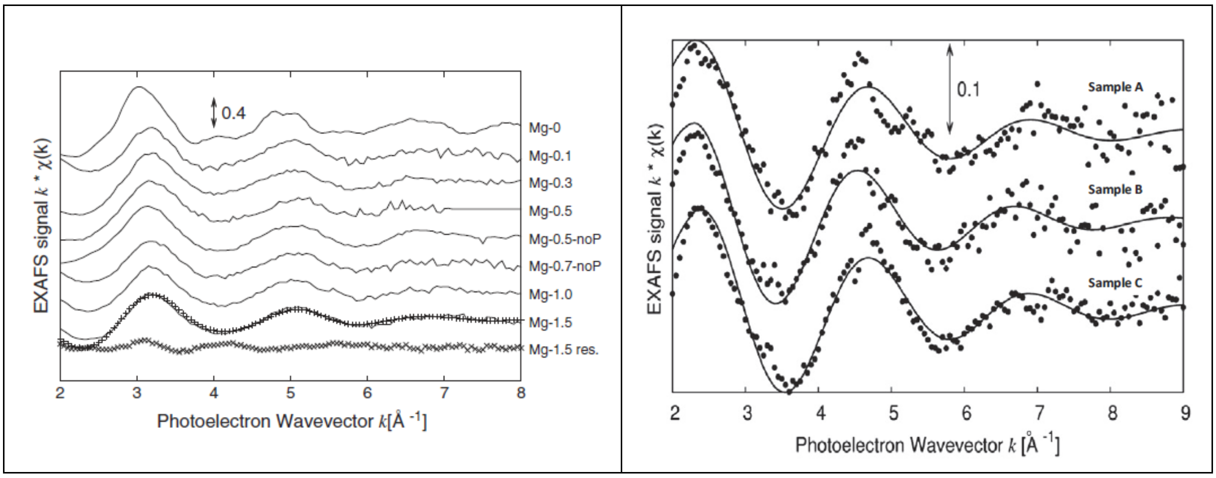

Figure 38: EXAFS data collected in fluorescence mode on different fibre preforms using a 200μm beam (GILDA configuration). Left: EXAFS data at the Er-L_{III} edge (from [Dac-14]), Right EXAFS data on Bi-L_{III} edge (from [Tor-15]).

The 3+ state for Bi in silica-alumina glass was successively confirmed by another investigation [Veb-18] on bulk glasses. Here, a series of samples with different amounts of Bi were compared. This study revealed that for decreasing values of the Bi concentration the metal tends even to reduce at valence values < 3^+. The environment of Er has been studied in the case of a glass ceramics consisting in glassy SiO_2 and nano-crystalline SnO_2 [Van-15]. The scope of creating this composite material is that when inserted in crystals Er ions are less prone to clustering (so degrading the luminescent properties) than when hosted in a glass. The use of sufficiently small nanoparticles provide at the same time a crystal for hosting the RE and a transparent material with reduced light scattering effects. In this case the comparison of experimental data with ab-initio calculations revealed to be fundamental in order to distinguish Er in one matrix or in the other. Indeed, according to structural simulations, Er in SnO_2 substitutes for Sn so entering in a 6-coordinated site whereas in silica the coordination is higher. This is reflected by the Er-O bond length that approaches $R_{Er\text{-}O}$=2.20 Å in the former case and $R_{Er\text{-}O}$=2.30 Å in the latter case. From these considerations it was possible in [Van-15] to define for Er a double occupation, part of the RE in the silica matrix and part in the crystalline inclusions that could reach up to 13% in case of a suitable thermal treatment.

Concerning glasses for medical applications we report here a study on Silica microspheres (hollow or bulk spheres) doped with Er and Yb [For-14] for applications in Photoluminescence bio-imaging. This study was aimed to determine the ligand of the RE (fluorine of oxygen) as in the two cases the efficiency of up-conversion from IR to green is different. Following the various preparation methods, the hollow microspheres exhibited RE ions linked to fluorine whereas in the preparation of bulk spheres the REs formed a thin layer of crystalline oxide. In this case a combined analysis with data collected in standard fluorescence method and XEOL (X-ray Excited Optical Luminescence) yielded the same result revealing that all the luminescent ions were in the crystalline oxide phase. Bioactive glasses doped with Ce have been studied by [Ben-17]. In this case the wide energy range of the beamline revealed to be decisive as the analysis at the Ce-K edge (40443 eV) permitted to have spectra well extended in k space for an easier comparison with ab-initio calculations. The result in this case was that Ce in the glass has a contracted bond length with O respect to CeO_2 crystal bulk and that if exposed to H_2O_2 no appreciable changes in the Ce valence state were evidenced. X-ray Photoelectron Spectroscopy instead had revealed differences in this case and this was interpreted as only the most surface Ce ions interact with the external environment.

Further studies about Rare Earth ions in glassy matrices were those about Erbium in Porous Silicon [Mul-17] and in Zinc-Lead telluride glass and Nd in chalcogenide glasses [Cha-18].

7.3.3. Bulk Chalcogenide glasses

A series of studies has been devoted to the structure of bulk chalcogenide glasses Ge-(Ga)-(As/Sb)-(Se/Te) [Pet-15], [Pet-16], [Pet-18]. In this case the problem of the dilution of the absorber was not present and the data collection was carried out in the conventional transmission mode. In order to minimize the interactions between the focused beam and the sample inhomogeneity data were collected with flat crystals in the old GILDA configuration. Considering the improvement experienced in this way, LISA was equipped with an experimental hutch (EH1) totally dedicated to data collection with a large and homogeneous beam far from the focal point of M2. XAS data were collected at the K edges of all the components and the data analysis was carried out in an advanced way making use of the Reverse Monte Carlo (RMC) technique. In order for this method to work data from other techniques are needed (X-ray or Neutron scattering), in order to model the long range features of the glass. Successively a structural model is generated and the structure is adjusted until a good agreement is reached between the calculated EXAFS function / scattering functions and the experimental data. From the structure so obtained it is possible to extract the partial pair correlation functions and all the more relevant structural parameters (bond length values, number of neighbours). It has been evidenced that the number of neighbours around the different components follow quite strictly the “8-N” (N being the number of electrons in the outermost *s* and *p* states) Mott’s rule with some limitation on Ga.

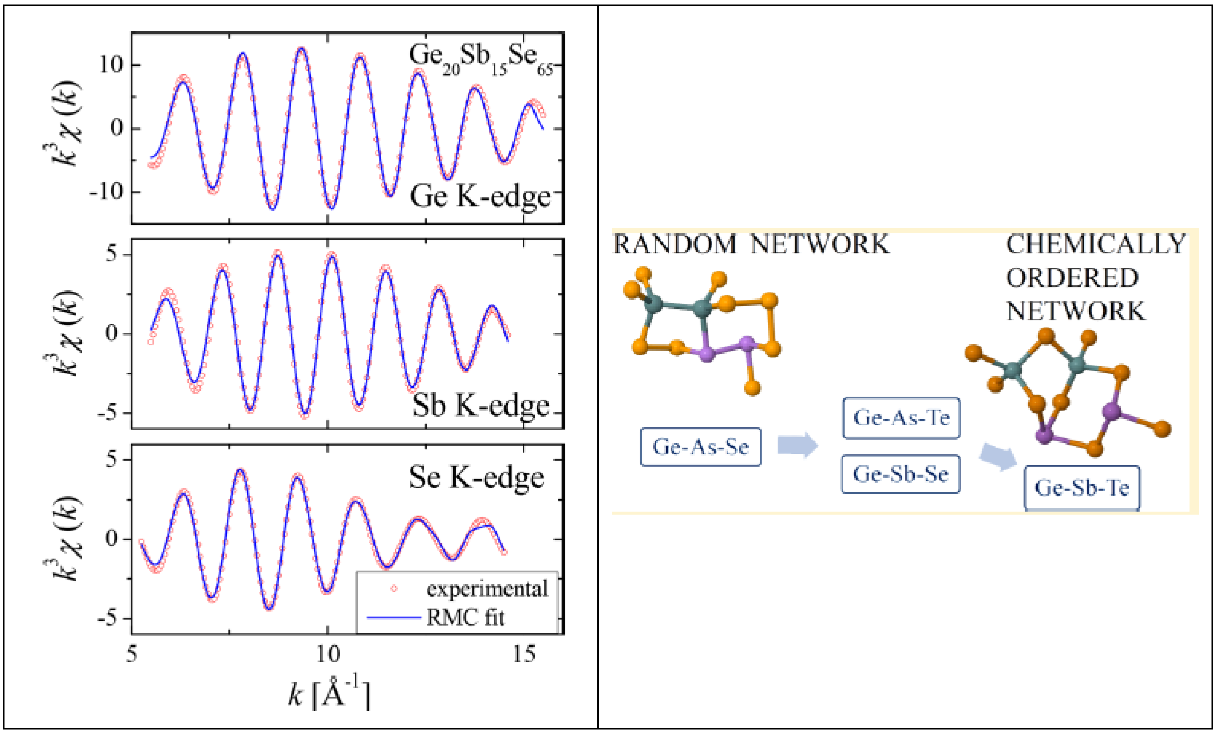

Figure 39: Left: comparison between the experimental data (filtered EXAFS functions) and the fit with the RMC method. Right: structural network models ('random' or 'chemically ordered') for the different glass compositions. Pictures from [Pet-16]

These systems tend to create heteroatomic bonds for the metal elements (Ge, Sb) with some Se-Se or Te-Te bonds in cases of abundance of chalcogen. Ge-Ge bonds reach a minimum for stoichiometric compositions but never go to zero and their presence in the structural model always improves the RMC fits. Generally the networks can be described by an ordered model (Chemically Ordered Network Model, CONM) for the Ge-Sb-Te system whereas the Ge-As-Se system in completely random.

7.4 Nano-Optics

Francesco d'Acapito, CNR-IOM-OGG, Grenoble (France)

A series of articles has been devoted to luminescent nanostructures for optical applications. In these cases the use of the XAS-XEOL experimental technique and/or the comparison with ab-initio structural simulation have revealed to be powerful tools for the comprehension of the systems under study.

7.4.1. Metal clusters in zeolite

Metal oligomers in zeolites have been shown to be efficient light emitters [Fen-16]. Ag_4 clusters namely are strong emitters in the green band [Gra-18] and the emission can be tuned by changing the composition of the host material [Bae-18]. In the case of Ag in Linde Type A (LTA) zeolite the metal form clusters of 4 atoms that are surrounded by a variable number of water molecules. Transmission XAS (Tr-XAS) and XEOL-XAS data collected at the same time on the sample permitted to reveal the structure of these clusters. XAS data contain information on the bonds of Ag with Oxygen (from zeolite framework or water) and other silver atoms. Tr-XAS exhibit Ag-Ag bonds always shorter respect to XEOL-XAS. The quantitative analysis, carried out compared with Density Functional Theory structural simulations, permitted to interpret the data as follows. The clusters are formed by 4 silver atoms in a tedrahedral-like arrangement and can be surrounded by either 2 or 4 water molecules (Figure 40). Simulations show that the ground state of the cluster is with all the 4d states full and a 2+ total charge. This leaves 2 electrons in the lowest energy 'superatom' state of the type ^1S. Optical excitation brings these electrons in a ^1P state at first but the presence of water molecules, induces a ligand field perturbation of the states that makes possible the decay to the ^3P state at lower energy. The difference between Tr-XAS and XEOL-XAS (i.e. a shorter Ag-Ag distance in the former case) is similar to what calculated by DFT for the ground and excited states, showing then that XEOL evidences this last set of Ag sites.

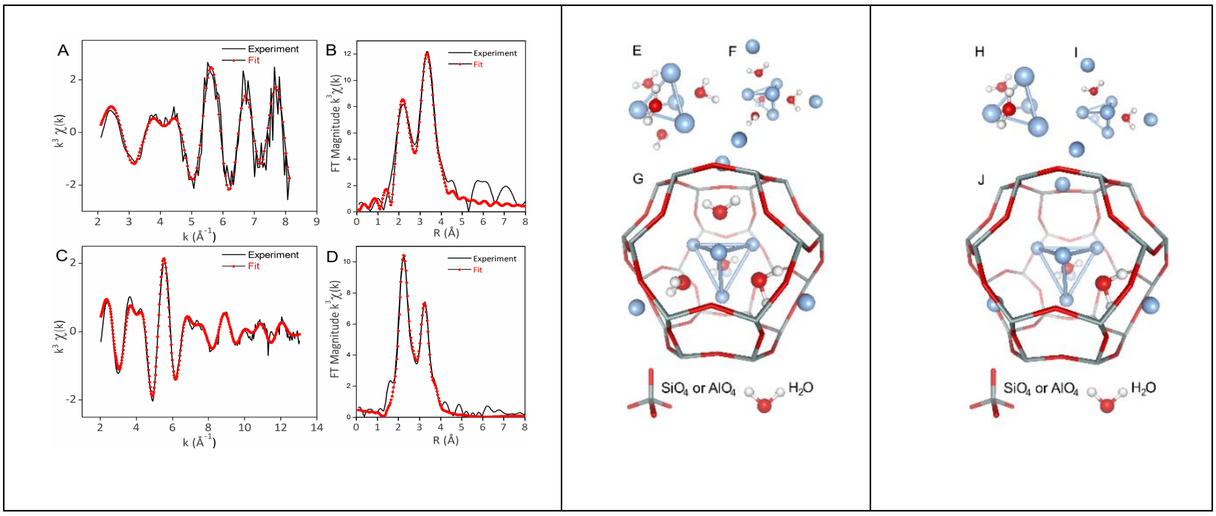

Figure 40: XEOL-detected (A,B) and transmission-detected (C,D) k3-weighted Ag K-edge EXAFS with the phase corrected FT of heat-treated Ag3K9-LTA best fits. Structures of Ag4(H2O)4 and Ag4(H2O)2 (E and H), including AgR cations (F and I) and embedded in the sodalite) (G and J) respectively. Pictures from [Gra-18]

Further evidence of different information brought by XEOL-XAS respect t Tr-XAS has been revealed in [Bae-18]. Here samples of Ag-doped LTA zeolites were produced with a variable amount of Li as additional cation. The Li insertion was shown to cause a contraction of the overall lattice parameter of the zeolite. From the point of view of XAS the Ag-Ag distances exhibited a different behaviour with Li content depending on the data collection method: for Tr-XAS they were unaffected by the Li amount whereas for XEOL-XAS a contraction was observer upon Li increase. This is in agreement with the observed optical behaviour and ab-initio simulations for which a shift towards shorter emission wavelength is reported. Tr-XAS measurements carried out on LTA zeolites loaded with Pb have revealed a similar behaviour with formation of Pb_4 clusters in the sodalite cages of and optical emission in the blue part of the spectrum. The analysis of the related XEOL-XAS data are currently in progress.

7.4.2. Doped nanoparticles.

Nanoparticles (NPs) can possess unique optical features due to the quantum confinement of the electronic states. The addition of dopants is in principle a way to further modify the optical response of the NPs provided that an efficient method of incorporation of the host atoms is found. XAS reveals to be an ideal technique at this purpose as it permits to shed light on the surrounding of the dopant so revealing the possible incorporation. Ab-initio structural simulation constitutes a fundamental tool for the correct interpretation of the XAS data. A recent paper [Sta-16] relates about the doping of PbS nanoparticles with either Sb or In (n- or p- doping). XAS data at the K absorption edge of the dopant permitted to reveal its incorporation site. Due to the limited amount of absorbing atoms all measurements were carried out with a focused beam and in fluorescence mode. For Sb two types of bonds were evidenced, one with O revealing Sb atoms on the surface of the NPs or in the neighbouring environment whereas a further bond with S revealed a possible incorporation in the particle. In order to obtain a deeper understanding of the data ab-initio structural simulations were carried out on possible complexes involving Sb in the PbS matrix. In particular the Sb_{Pb}, $2Sb_{Pb} + V_{Pb}$, $2Sb_{Pb} + S_I$ atomic arrangements were considered and the result has been that $2Sb_{Pb} + V_{Pb}$ possess the lowest formation energy and the better agreement of the bond length values with the experimental data.

Nanoparticles can also act as hosting material for luminescent species as already discussed in vitro-ceramics systems. Incorporating, namely, Rare Earth ions (REs) in crystals permits a complete dissolution of the REs limiting the clustering effect respect to the doping in glasses. Here we report on a study dedicated to the incorporation of Er^{3+} species at high (5%) and low (0.5%) concentration in CaF_2 nanoparticles [Dac-16]. Nanoparticles of about 30 nm in diameter were prepared by co-precipitation. The XAS analysis carried out at the Er-L_{III} edge revealed the presence of 2 shells around the RE: Er-F at 2.27 Å and Er-Ca at 3.92 Å with the second shell more disorder in the case of the high Er content. (Figure 41)

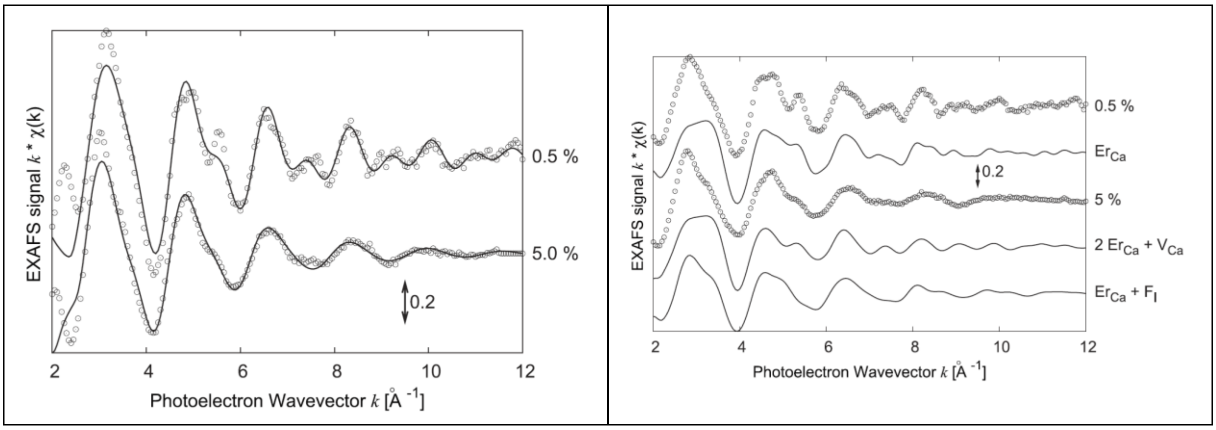

Figure 41: Left EXAFS spectra for the high- and low- Er content samples with the best fit curves. Right: experimental (dots) and theoretically calculated (lines) EXAFS spectra of samples and some complexes considered in the theoretical simulations. Pictures from [Dac-16]

In order to understand these results ab initio structural simulations were carried out. In particular Density Functional Theory (DFT) methods were used to produce either static relaxed structures (i.e. by minimizing the total energy) but also dynamic structures (via Molecular Dynamics) in order to generate theoretical EXAFS signals. A series of possible sites were considered Er_{Ca}, $2Er_{Ca}+V_{Ca}$, $Er_{Ca}+F_I$, this last being the site indicated by literature for the incorporation of Er in bulk crystals. For reasons of charge balance the Er_{Ca} site is actually not alone but associated to a charge compensating defect (either a vacancy or an interstitial) positioned at a sufficiently long distance to avoid any local structural effects. The analysis of the DFT results permitted to discard the $Er_{Ca}+F_I$ site as the Er-F bond length was predicted to be too long (2.33 Å) respect to the experimental data. On the other hand the other two sites seemed to reproduce well the experimental findings. In order to decide the best candidate EXAFS spectra were simulated from the MD frames and compared with the experiment. The $2Er_{Ca}+V_{Ca}$ exhibits a higher disorder in the second coordination shell (induced by the presence of the vacancy and consequent split of the shell) respect to the Er_{Ca} site. It was then supposed that the latter was the site for Er at low concentration and the other was formed in case of high concentration.

7.5 Catalysis

Antonella Balerna, INFN-LNF, Frascati (Italy).

Many catalysis studies have been performed at the LISA beamline from the end 2014 to 2018 investigating quite different catalytic reactions and systems. Some proposals required *in situ* measurements, using specific environmental cells, and some *ex situ* ones. The spectroscopy mainly requested was XAFS (X-ray Absorption Fine Structure) but there were also some important results achieved using XRD (X-Ray Diffraction) measurements at LISA. In particular important results on catalysts used for hydrogen storage were achieved with *in situ* measurements monitoring the structural evolution by *both XAFS and XRD*.

7.5.1. Bimetallic catalysts: AuAg/Al2O3, PdCu/PVPy, CoRu/SiO2, CoPt/SiO2

`Bimetallic catalysts are of great interest from both a scientific and an industrial point of view thanks to their catalytic, electronic and optical properties often different from their corresponding mono-metal systems. Among the numerous structural features which can influence their catalytic efficiency, such as particles size and shape like in the monometallic systems, the chemical states and the distribution of the two metals within the individual nanoparticles (e.g., alloying, core-shell or segregation) play a crucial role. Bimetallic catalysts with application in different field have been studied at the LISA beamline due to the presence in the bimetallic samples of elements with high atomic number or the need to study the K-edges of *4d* elements. As a function of the metallic wt% presence in the different samples, XAFS measurements were performed in transmission or also in fluorescence mode thanks to the possibility to use at LISA a 13-element HPGe XRF detector.

Bimetallic **AuAg** catalysts on Al_2O_3 prepared using two different techniques like Solvated Metal Atom Deposition (SMAD) and the Sol Immobilization (SOL**) [Jou-18]**, were studied using XAFS spectroscopy in order to control the effects of the structure of the catalyst on the selectivity of glycerol oxidation. The use of heterogeneous catalysts with molecular oxygen represents an environmental friendly alternative to stoichiometric amounts of inorganic oxidants, which generate abundant waste. The high potential of gold nanoparticles on various supports is well demonstrated in aerobic oxidation reactions. Silver nanoparticles (NPs) are one of the catalysts most employed in oxidation reactions. The drawback that limits the expansion of silver utilization is its tendency to deactivate due to passivation phenomena. A possible solution to overcome this limitation is to combine silver with a second metal, in particular Au. Especially in selective oxidations the gold-rich alloyed and gold nanoparticles largely exceeded the activity of monometallic silver nanoparticles. AuAg bimetallic catalysts were rarely studied in glycerol oxidation, but synergetic effect and selectivity modification may be expected and was demonstrated [Jou-18] because compared to the gold containing ones, and both the SOL and SMAD bimetallic systems presented synergetic activity increase. The XAFS measurements performed at the LISA beamline revealed in both cases the presence of Au-rich cores and Ag-rich shells. XAFS showed that in SOL preparation Ag only partially covers Au whereas in the case of SMAD the Ag enrichment on the surface is much larger than in the SOL case. Ag resulted more resistant to oxidation in the SOL sample than in the SMAD one (Figure 42 a). A part from differences due to particle size, strong differences can be revealed in the catalytic oxidation of glycerol in terms of activity and selectivity. AuAg SOL prepared is more active than AuAg SMAD one and, most interestingly, the SOL sample showed a different selectivity compared also to the monometallic Au SOL catalyst probably due to its smaller dimensions (Figure 42 b).

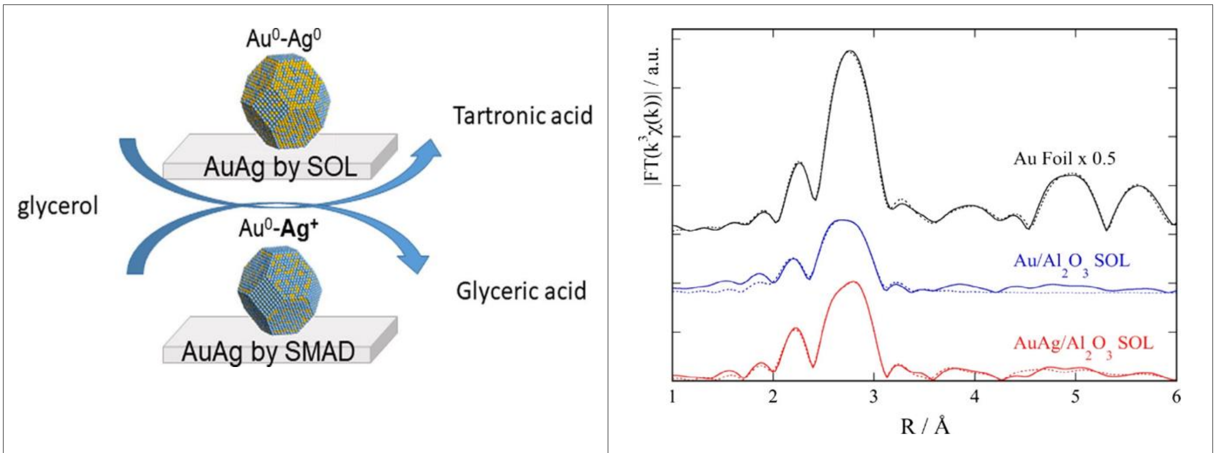

(a)

(b)

Figure 42: [a]: Schematic view of synergistic effects of the AuAg SOL and SMAD bimetallic catalysts in glycerol oxidation giving different behaviours as a function of the depth of the Ag shell. [b]: Fourier transforms of the experimental (full lines) and theoretical (dashed lines) EXAFS spectra of the as prepared Au and AuAg SOL samples compared to the ones of the Au reference sample.

Bimetallic catalysts which include a combination of a group VIII, such as Pd, and a group IB, such as Cu, have been extensively studied in many processes such as hydrogenation or oxidation reactions but only a smaller number of studies concern their use in Sonogashira coupling reaction that is a very powerful method for the formation of C_{sp2} - C_{sp} bonds. **PdCu** bimetallic solvated metal atoms (SMA) synthesized by metal vapor synthesis (MVS) technique and supported on poly-4-vinylpyridine (PVPy) resin, showed significantly higher catalytic activity in Sonogashira-type carbon-carbon coupling reactions than the corresponding monometallic Cu and Pd systems. The analysis of the bimetallic catalyst combining HRTEM and XAFS spectroscopy revealed the presence of small Pd nanoparticles (d_m=2.5 nm) **[Bal-16]** while the analysis at the Cu Kedge suggested the formation of thin and incomplete Cu oxide layers around the Pd-rich cores **[Eva-17]**. Some Pd-Cu alloying in the immediate subsurface layers of the Pd nanoparticles was found, whereas the bigger portion of Cu atoms were in an oxidized Cu^{2+} phase probably forming thin and incomplete shells around the Pd-rich cores The higher catalytic efficiency of the bimetallic system compared to that of the corresponding monometallic Pd and Cu systems suggested that the presence of a Cu-Pd interaction favors a synergic effect between the two metals in Sonogashira reactions, increasing significantly (about 4 times) the activity of the catalyst. The formation of a Cu oxide shell on the surface of metal

Pd nanoparticles could explain this effect. Although the catalytically active species involved in the coupling reaction mechanism are still not well known, it has already been observed that the increase of the catalytic activity in the presence of copper oxide species agrees with the formation of transient Cu-acetylide species which leads to alkynylpalladium (II) derivatives by transmetallation which proceeds to give the required coupled products and to regenerate the active Pd species [Eva-17].

CoRu and **CoPt** bimetallic catalysts supported on silica prepared by successive impregnation were characterized, in particular using EXAFS spectroscopy, and tested in Fischer-Tropsch synthesis (FTS) reactions **[Pir-14]**. FTS is a well-known industrial process, which starts from syngas (mixture of CO and H_2 obtained from CH_4, coal or, as a new tendency, biomass) for the production of light and heavy hydrocarbons. FTS usually requires catalysts based on iron or cobalt. Co-based catalysts show longer lifetime and higher CO conversion compared to the Fe based catalysts. Promotion with platinum and ruthenium greatly increases the rate of cobalt reduction. There are many experimental works on the study of the structure of FTS catalysts, aiming to unveil the role of both Co and noble metals. This is not a simple task due to the complex nature of the samples, which are composed of a support, Co in metallic and oxide phase (about 10 wt%) and the noble metals acting as promoters (less than 2 wt%). In the present work two sets of supported bimetallic catalysts (BMCs) containing 10 wt% of Co and different percentages of Pt and Ru (0.1, 0.25, 0.5, and 2.0 wt%) were studied in order to study and compare their catalytic performances and structures. FTS results showed that both CO conversion and the total yield towards desired products could be tripled thanks to the action of the noble metals, present in low amount (0.5 wt%) in the catalysts composition. EXAFS analysis has shown different interactions of the two noble metals with cobalt in the BMCs. Concerning the CoRu catalysts, Ru_{1-y} Co_y solid solutions with hexagonal close packed structure form were identified with *y* in the 0.1-0.23 range for all Ru concentrations. Differently in the CoPt BMCs, the structures found are strongly dependent on Pt amount: for low Pt amount (0.1%) Co and Pt form an intermetallic PtCo compound with a face centered tetragonal structure while for the higher Pt amount (2%) a close packed cubic structure was found.

7.5.2. Monometallic catalysts and substrates: Ag/CeO_2, Pt/CeO_2, Pd, Au, Cu

Cerium oxide is receiving a great interest in recent years, due to its high reducibility, i.e. due to the possibility for Ce ions to quickly modify their oxidation state in a reversible way. The reducibility of cerium oxide can be enhanced by the proximity of metallic atoms in the form of dopants or by supported metallic nanoparticles (NPs). The Ag/CeO_2 [Ben-15] and Pt/ CeO_2 [Pil-16] catalysts have been studied at the LISA beamline. The Ag/CeO_2 system has important applications in catalysis. In most cases, the **Ag/CeO_2** catalyst showed a higher activity and durability than its individual components, and catalysts with lower Ag loadings, in which the Ag-CeO_2 interface has a larger relative weight, show lower activation temperatures. The strong interaction between Ag and cerium oxide has been shown to be largely dependent on the shape and stoichiometry of the oxide. The structure of Ag nanoparticles supported on the cerium oxide (111) surface, was investigated by XAFS at the Ag K-edge **[Ben-15]**. The XAFS spectra were acquired in the fluorescence mode using a HP Ge detector. In spite of the extremely low surface density of Ag atoms in the samples (ranging from ∼ 6 to 90 Å x 10^{13} atoms/cm^2), XANES spectra, with an acceptable signal-to-noise ratio on all samples were taken at the LISA beamline (Figure 43 [a]). On the other hand the EXAFS spectra were acquired only on two selected samples, containing 0.2 and 1.5 Å of Ag (see the Fourier transforms of the EXAFS data in Figure 43 [b]). On the 1.5 Å Ag sample, the EXAFS spectra were measured in three different experimental geometries, to selectively study structural changes in different orientations *exploiting the polarization dependence of the XAS cross section*. The different configurations used were: (i) sample in the vertical orientation and photon beam at 80° from sample normal (V80°); (ii) same as sample with the photon beam at 45° from sample normal (V45°); (iii) sample in a nearly horizontal orientation (higher sensitivity to the surface layers) and photon beam at 86.5° from sample normal (H86.5°). The Ag nanoparticles showed a face centered cubic structure with an Ag-Ag interatomic distance contracted by 3-4% with respect to the bulk value. The presence of Ag-O bonds at the interface between the nanoparticles and the supporting oxide was also detected. The Ag-O interatomic distance decreased with decreasing nanoparticle size possibly due to a larger charge transfer per Ag atom between the NPs and cerium oxide.

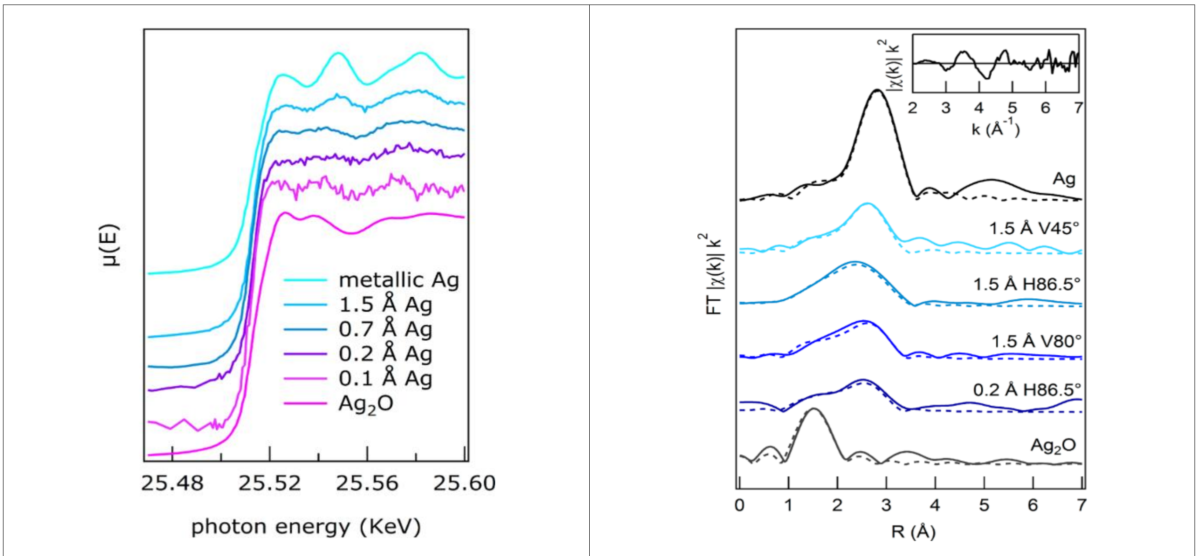

(a)

(b)

Figure 43: [a]: Ag K-edge XAFS spectra in the near edge energy range for the samples with different Ag nominal thickness on a 10 ML cerium oxide film. The reference spectra of bulk metallic Ag and Ag2O are also shown for comparison. [b]: Modulus of the Fourier transform of the k^2-weighted Ag-K edge $\chi(k)$ (solid lines) and fits (dashed lines) for the 1.5 Å Ag sample in three different experimental configurations, for the 0.2 Å Ag sample in the H86.5° configuration and for a metallic Ag and Ag_2O reference samples. The inset reports the raw k^2-weighted $\chi(k)$ data of the 1.5 Å sample in the V45° configuration.

Recent literature on **Pt/CeO_2** catalysts revealed that ionic Pt species could be incorporated into the CeO_2 lattice. A detailed study of Pt segregation in air and under a reducing atmosphere conducted on thermally treated samples by high-resolution X-ray diffraction (XRD) and X-ray absorption spectroscopy was performed **[Pil-16]**. Also a kinetic study by in situ XRD measurements with the aim of estimating the activation energy for Pt cluster segregation and coalescence in air, which was found to be ∼3.88 eV was realized. The high activation energy indicates that Pt clusters are strongly anchored on the CeO_2 surface and that their mobility is activated only at $T > 900$ **°**C. On the basis of thorough characterization, a possible segregation pathway under oxidizing conditions as opposed to a mere surface reduction during a reducing treatment, leading to the coalescence of less anchored Pt was proposed. The catalytic performances confirmed the remarkable activity and thermal stability.

For the first time a **Pd** catalyst supported on the commercial resin K2621 for the *direct synthesis* (DS) of H_2O_2 from H_2 and O_2 was investigated using *in situ* Pd K-edge XAFS spectroscopy also at the LISA beamline **[Cen-15]** and **[Cen-15.1]**. The development of catalytic systems suitable for the selective synthesis of H_2O_2 from H_2 and O_2 (direct synthesis, DS) has been the subject of extensive investigation for at least a decade Although H_2O_2 is currently produced on the scale of 2.2 million metric tons per year by the well-established and efficient anthraquinone autoxidation (AO) process, the formation of H_2O_2 is an important topic for the development of new processes for the small-scale production. Applications on a smaller scale are less attractive because of the high transportation costs for H_2O_2. Consequently, the implementation of new processes based on DS is expected to boost the exploitation of H_2O_2 in new applications, such as the preparation of fine chemicals. A Pd catalyst supported on the commercial resin K2621 has been characterized by *in situ* XAFS spectroscopy by using a suitable plug-flow reactor cell during the direct synthesis of H_2O_2. Both the dry and methanol-swollen catalysts were characterized by the presence of metal Pd and PdO with the same relative abundance and structural parameters. No significant changes in the features of both the Pd and PdO phases were observed treating the catalyst with methanol (the reaction solvent) and under the reaction conditions. Interestingly, in the presence of sodium bromide, a remarkable leaching of the active phase was detected, both with concentrated (1000 ppm) and diluted (10 ppm) solutions of sodium bromide, which was confirmed by the decrease of the edge jump. The leaching and the apparent reduction of PdO were simultaneous and the action of bromide ions observed directly for the first time could be connected to their well-established promotion of this reaction.

A detailed study of the structure and surface morphology of small **Au** clusters (around 2.5 nm) deposited on silica/silicon substrates with different defects content has been carried out using several characterization techniques **[Por-14]**. Native silica on silicon substrates (n-SiO**x**/Si) enriched in defects was prepared by air exposure of silicon surfaces with different doping levels. Defect free SiO_2/Si (t-SiO_2/Si) substrates have been prepared by thermal oxidation. The average gold cluster dimensions have been determined also using XAFS spectroscopy at the LISA beamline. The interactions between the deposited gold clusters and the support were studied. The presence of an Au-O component only for the samples deposited on n-SiO_x/Si substrates proved the presence of an interaction between Au atoms from the clusters and oxygen atoms from the support. The observed interaction suggested that the first deposited Au clusters anchor on the defects present at the substrate surface (dangling bonds, non-bridging oxygen centers), inducing a preferential aggregation of Au clusters around these anchoring points. The Au-substrate interaction is thus responsible for the larger grain size and the higher surface roughness of Au nanoparticle films deposited on n-SiO_x/Si. These results evidenced metal-support interaction in small gold nanoparticles supported on silica, that such interaction can affect their morphology and can play an important role in their properties.

The use of supported metallic nanoparticles (NPs) is fundamental for the development of new catalysts with high activity and selectivity. For this reason, the choice of a suitable support, the selection of metal precursors and the preparation methods become quite important. The structural effects induced on metal vapor synthesis (MVS) derived **Cu** NPs by different carbon-based supports such as poly-4-vinylpyridine (PVPy) and carbon and how these effects can affect their catalytic activities in Huisgen azide-alkyne cycloaddition reactions (CuAAC) have been studied **[Bal-17]**. As shown by the XAFS data analysis, Cu NPs, immobilized on PVPy, resulted in a Cu(I) oxidized phase while the ones on carbon were in a Cu(II) phase. The structural effects induced by the different supports determined a completely different catalytic behavior of the two catalytic systems in a model CuAAC reaction: the PVPy-supported Cu system was active and re-usable whereas the analogous carbon-based system was almost inactive.

7.5.3. Oxo-clusters, nano-oxides, oxides and oxides nanowires

The synergy between different functional building blocks is the driving force for the synthesis of novel organic-inorganic hybrid materials **[Ben-16]**. Particularly interesting are materials obtained by covalent incorporation of functionalized inorganic metal-based building blocks into a polymer matrix through copolymerization with suitable monomers (so-called class II organic-inorganic hybrid materials). Among inorganic nano-sized building blocks, oxide-based clusters or **metal oxo-clusters** are receiving growing attention. In particular, metal oxo-clusters and polyoxometalates containing early transition metals in their highest oxidation state (d^0) display interesting catalytic properties. They have been shown to activate hydrogen peroxide or organic peroxides and promote the oxidation of different substrates, such as olefins, sulfides, sulfoxides, and alcohols. Organic-inorganic hybrid nanoparticles were prepared by free-radical copolymerization of methyl methacrylate (MMA) with the structurally well-defined methacrylate-functionalized zirconium oxo-cluster Zr_4O_2(methacrylate)$_{12}$ [Benedetti-16]. The formation of covalent chemical bonds between the organic and the inorganic counterparts improved the distribution of the guest species (oxo-clusters) in the polymer particles, overcoming problems related to migration, leaching, and stability. Because of the presence of a high number of double bonds (12 per oxo-cluster), the oxo-clusters act as efficient cross-linking units for the resulting polymer matrix, thus ruling its swelling behavior in organic solvents. The synthesized hybrid nanostructures were applied as heterogeneous systems in the catalytic oxidation of an organic sulfide to the corresponding sulfoxide and sulfone by hydrogen peroxide, displaying quantitative sulfide conversion in 4-24 h, with overall turnover numbers (TON) up to 8000 after 4 cycles. To confirm the structural integrity of the Zr_4 oxo-cluster after the polymerization, the hybrid poly(MMA-co-Zr_4) nanoparticles were analyzed by XAFS at Zr K-edge and the spectral output compared with that of pristine Zr_4 oxo-clusters.

Cerium oxide based materials are attractive due to their capacity to quickly store, release and transport oxygen ions, which makes them suitable for application in different fields. An accurate description of the structural and chemical modifications of **cerium oxide nanoparticles** is mandatory for understanding their functionality in applications. The relation between local atomic structure, oxidation state, defectivity and size in cerium oxide NPs with variable diameter below 10 nm, XAFS analysis has been investigated **[Pel-17]**. Using a magnetron sputtering and inert gas aggregation nano-cluster source, under controlled conditions, NPs were prepared. XAFS analysis determined that the cerium oxide NPs with diameter below 10 nm had a dominant single crystalline fluorite structure showing a contraction of the Ce-O distance compared to the bulk value, in contrast with the frequently observed lattice expansion with decreasing NP size. The contraction had a linear dependence on the surface-to-volume ratio and was ascribed to a compressive strain arising from reduced dimensionality. The size-induced strain dominated over the local expansion expected at the Ce^{3+} sites, due to the low concentration of reduced ions in the investigated samples.

To further improve the thermal stability and the textural as well as redox properties of **CeO_2-based materials** without deteriorating their *oxygen storage capacity* (OSC), *t*-$Ce_{1-x}Zr_xO_2$ solid solutions are employed in automotive catalysis. The solid solutions, $Ce_{1-x}Zr_xO_2$, are shown to be both catalytically active and chemically stable over a wide concentration range of Ce from 20 at.-% to 80 at.-%. Recently, it was reported that the OSC can be dramatically enhanced by transforming a *t*-$Ce_{0.5}Zr_{0.5}O_2$ solid solution in the so-called “kappa phase” κ-$Ce_2Zr_2O_8$. The κ-$Ce_2Zr_2O_8$ phase contains an ordered array of cations, and 1/8 of the oxygen anions can readily be removed leading to an extraordinarily high OSC. This phase has demonstrated high catalytic activity in the combustion of chlorinated compounds due to the improved OSC properties. The κ-$Ce_2Zr_2O_8$ phase has been synthesized starting from *t*-$Ce_{0.5}Zr_{0.5}O_2$ solid solution, which was reduced by hydrogen at high temperatures to form the pyrochlore $Ce_2Zr_2O_7$ phase (*pyr*-$Ce_2Zr_2O_7$) with high degree of ordering of the cationic sublattice **[Urb-16]**. The final step in the synthesis of the κ-$Ce_2Zr_2O_8$ phase included a mild re-oxidation of *pyr*-$Ce_2Zr_2O_7$ at around 600°C under atmospheric conditions. Compare dto other studies it was shown that 1300°C is not sufficient to warrant the preparation of phase-pure *pyr*-$Ce_2Zr_2O_7$ and κ-$Ce_2Zr_2O_8$, but that temperatures as high as 1500°C are required to assure phase purity of both phases. These conclusions were drawn from XRD and XAFS analyses that provided details of their structures, on the evolution of the special periodic structure and the coordination of the metal atoms.

Release of various organic pollutants such as textile dyes, phenols, aromatic amines and other carcinogenic materials from many industries is becoming a serious problem. Dyes from textile industries are often organic molecules with complex structures, highly toxic in water, non-biodegradable and a serious concern to the ecosystem. Hierarchical 3D urchin-like nanostructures are promising for wastewater treatment through heterogeneous photo catalysis because of their high surface area, which facilitates catalysis by providing a larger solid liquid interface **[Edl-15]**. Pulsed Laser Deposition (PLD) and thermal oxidation synthesized a porous coating assembled with hierarchical 3D Co_3O_4 urchin-like particles. Laser ablation of Co-B powder, used as the target material, in oxygen atmosphere formed core-shell particles on the coating surface with mainly a metallic Co core and a mixture of Co, B and O accommodating the shell. The thermal oxidation of these core-shell particles in air at 600°C induced the morphological transformation to urchin-like particles consisting of **nanowires** (NWs) (diameter: 30-60 nm and length 1-3 μm) grown radially from the core surface. The extrusion marks on the surface of NWs indicate that the stress induced growth process is caused by difference in the thermal expansion coefficient. XAFS data analysis confirmed that the NWs were polycrystalline consisting of pure Co_3O_4 phase. Features such as high surface area, enhanced stability against agglomeration, polycrystalline nature of the NWs, porous surface and superior adhesion, are responsible for the enhanced photo catalytic activity of these Co_3O_4 urchin-like particles.

7.6 Materials for energy conversion and storage

Alessandro Minguzzi, Dip. di Chimica, Univ. Milano, Milano, Italy

The LISA (BM08) facility at the ESRF allowed an intensive and high impact work on materials to be used in energy conversion and storage devices. I here group the contributions in four main sections, that are dedicated to: (i) *Electrocatalysis for energy conversion,* dedicated to materials for fuel cells and electrolyzers, (ii) *Sunlight harvesting,* that deals with materials in photoelectrochemistry and photovoltaics, (iii) *Thermoelectric materials*, dedicated to materials capable of convert heat in electric energy and finally (iv) *Batteries¸* dedicated to the study of battery materials, particularly in Li-based ones. Considering all the published material discussed in this highlight, it is very easy to find common reasons that explains the choice of BM08:

- the availability of a 12-element fluorescence detector, which enables fluorescence mode experiments. This is needed in the case of diluted samples, or when the amount of sample is particularly low, as in thin films, electrodes etc.

- the availability of a system for illuminating samples in the hutch with visible/UV light that can be controlled remotely and in sync with the monochromator, for example for recording light/dark difference spectra in the study of photoelectrodes.

- the easiness of adapting the facility to the need of each and every experiment. For example, the synchronization of visible light pulses with single synchrotron bunches and the possibility of triggering the start of an electrochemical measurement and the acquisition of the X-ray absorption coefficient in fixed energy experiments.

7.6.1. Electrocatalysis for energy conversion

This section includes a wide variety of systems, ranging from water electrolysis to fuel cells and extending towards the storage of gases involved in these devices. In the latter case, metal organic frameworks (MOFs) will likely play an important role. A Cu-based MOF was studied at the Cu-K edge to prove structural changes while it is exposed to air for several days [Tod-17]. The study represents an interesting example on the high potentialities of XAS in this field and highlights the structural changes (e.g. Cu-Cu distance) caused by the absorption of water.

The capacity of storage a reaction reagent, intermediate or product might become a key-feature for a functional material. An example is given by gadolinia-doped ceria (GDO), which is capable of absorbing oxygen and being used in the oxidation of HCl [Mol-15]. Here, XAS was adopted to prove that Gd is homogeneously dissolved in the ceria and does not segregates as Gd oxides clusters. Oxygen plays indeed an important role in energy conversion technologies. In particular, the oxygen evolution reaction (here reported in acidic media):

$$2H_2O \rightarrow O_2 + 4e^- + 4H^+ \quad (1)$$

Represents the kinetic limits in water electrolyses, the latter being the most favorable reaction for the production of high purity H_2 using renewable energy sources. Electrocatalysts for the oxygen evolution reaction (OER) has been a favored research topic of electrochemists for several decades and new investigation methods are constantly under evaluation to collect new outcomes for clarifying the mechanism and thus design better and less expensive electrocatalysis. On these bases, operando XAS has been used to determine the nature of the active site in the case of Ir oxide electrocatalysts, that are the most active and stable materials in acidic media. As it happens in most of the studies summarized here and particularly in operando ones, where the material of interest is deposited as a layer onto a conductive support, the fluorescence detector installed in LISA represented the key of success for effective fluorescence mode experiments. Thanks to this setup, operando XAS at the Ir L_{III}-edge was carried out onto electrodeposited iridium oxide films to determine the oxidation states assumed by Ir during the OER [Min-14]. Working at the L_{III} edge allows the direct observation of the Ir *d* state occupancy. The work concludes in suggesting the co-presence of Ir(III) and Ir(V) under OER conditions, i.e. at 1.5 and 1.6 V ves the reversible hydrogen electrode, Figure 44-1. This study was followed by another one that, with a similar approach, aimed at studying the local structure of Ir in IrO_x with different hydration degrees [Min-15]. The results point to a negligible change in the local structure, meaning that it is able to easily accommodate different oxidation states of Ir. This might be at the bases of a low reorganization energy during the catalytic cycle and thus of the good performance of these materials. Another system of great interest subject of intensive study by XAS are Pd-based anodes for anion exchange membrane fuel cells (AEM-FC). The anodic process of this device is the hydrogen oxidation reaction (HOR):

$$H_2 + 2OH^- \rightarrow 2H_2O + 2e^- \quad (2)$$

This reaction has poor kinetics in alkaline media and new electrocatalysts are needed.

Pd catalyst onto a composite support made of active carbon and CeO_2 proved to be particularly effective. In this context, XAS demonstrated a relevant presence of PdO, that results from the strong Pd-CeO_2 interaction and from the oxide spillover capacity of ceria [Mil-16]. This causes the weakening of the Pd-H bond but also favors a fast transfer of OH^- ions from ceria to Pd that explains the high activity of this composite. The development of Pd catalyst could help in eliminating Pt from these devices. Unfortunately, Pd lacks of long terms stability. Understanding the reasons behind this is of high importance in the search of stabilizing strategies. To this aim, operando XAS was used to investigate on the reasons of this poor stability [Wan-15, Mon-17]. Ex-situ experiments were devoted to compare a Pd catalyst before and after use as AEM-FC anode [Wan-15]. The result points to the oxidation of Pd towards Pd^{2+} after operation. This is reasonably at the basis of the catalyst loss of activity. The system was further study using fixed energy X-ray absorption voltammetry (FEXRAV) which allows to monitor the oxidation state of the absorbing atom in real time and under operation [Mon-17].

FEXRAV is not capable of clearly distinguish different species having the same oxidation number and was here coupled to numerical modelling for a clearer interpretation of the experimental results. The use of a Ge fluorescence detector was vital for the success of the experiment. The study was able to confirm the prevalence, of the electro-dissolution processes of Pd, through Pd(OH)$_4^{2-}$ over the formation of PdO, Figure 44-2. The adoption of FEXRAV revealed to be effective also in two other cases of interest, where electrochemistry plays an important role in chemical synthesis and environmental remediation as mild process with low impact, thanks to the possibility of using renewable energy sources to drive the process. The first case allowed to prove the adsorption of the reacting species onto Ag nanoparticles [Ron-16]. This is in turn an interesting outcome that demonstrates the effectiveness of FEXRAV in studying phenomena leading to weak spectral changes, otherwise cancelled by signal manipulation (normalization, background correction etc.).

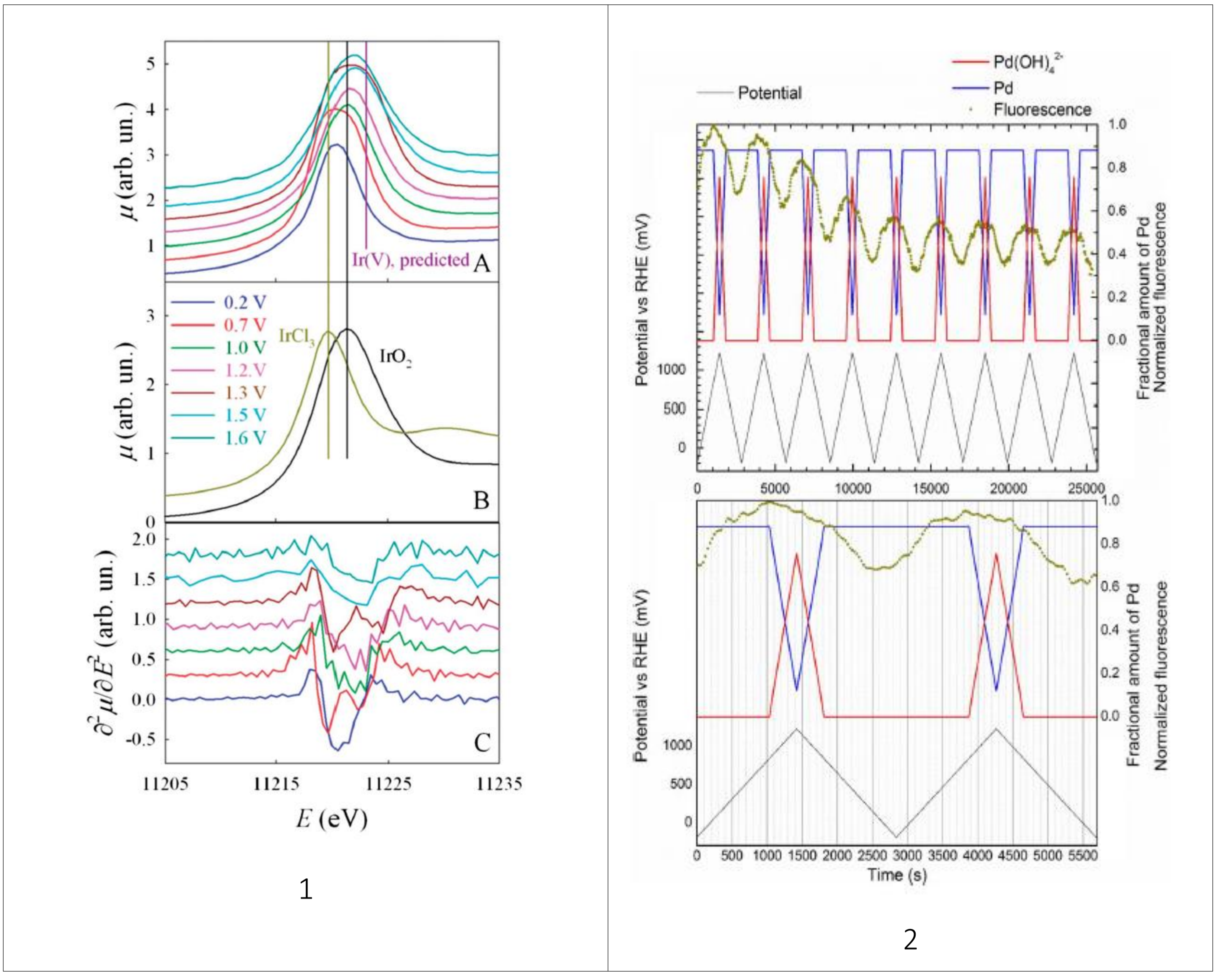

1

2

Figure 44 (1): Normalized Ir-L$_{III}$ edge XANES spectra of the electrode material under different applied potentials (A). The spectra of bulk IrO$_2$ and IrCl$_3$ are shown as a reference (B). The second derivatives are also shown(C). For better clarity, the spectra are shifted along the y axis, and vertical lines marking the energies of the White Lines of IrCl$_3$, IrO$_2$ and Ir(V) (predicted) are drawn. Reprinted from [Min-14]. (2): Experimental FEXRAV signal and calculated fractional amount of the relevant species, Pd and Pd(OH)$_4^{2-}$, during a potential scan rate of 1mV/s. The electrochemical cell was mounted in the three electrode scheme, and filled with a KOH 2M + EtOH 2M solution. FEXRAV signal was detected through the Fluorescence detector. (a) is the overwiew of the entire voltammetric scan (b) is a closeup of the first two cycles. Reprinted from [Mon-17].

The second study allowed to study two FeOOH phases, namely α-FeOOH (goethite) and γ-FeOOH (lepidocrocite) that are found as corrosion products of the steel cathode in the sodium chlorate process [Fra-18]. Analysis of the whole XAS spectrum (EXAFS+XANES) highlighted the presence of a structure bearing a relation with that of green rust that is forming under hydrogen evolution. This is independent on the phase of the initial electrode. Interestingly, during the electrochemical re-oxidation, the original phase is restored, meaning that the reduced phase brings some memory of the structure of the pristine material.

7.6.2. Sunlight harvesting

The production of hydrogen indeed represents one of the main topics in the research of materials for energy conversion: hydrogen has been identified as the most promising vector to store and transport renewable energy that is localized and intermittent. Alternatively, sunlight can be transformed directly to electric energy, as done in photovoltaics. In both cases, suitable semiconductors for a high yield transformation are needed. However, the functional material can be composed of two or more “actors”, each with a proper role. For example, a conductive support is needed, to connect the light harvesting materials to the other parts of the circuit. This support often needs to be transparent to the visible light, to allow the latter to reach the semiconductor. To this aim, new transparent conductive oxides (TCO) are under development. One of these, based on In_2O_3/Ag/In_2O_3 was studied at LISA by means of grazing incidence X-ray fluorescence (GIXRF) measurements, a suitable method for the study of multilayer systems [Cab-15]. In this case, GIXRF highlighted the presence of a thin inter-diffusion profile induced by thermal treatments. Thins film semiconductors were also studied as functional materials in photovoltaic cells. For example, Cu-, Zn-, S-bearing semiconductors were synthetized by electrochemical atomic layer deposition and studied by XANES and EXAFS to determine the obtained phases [Dib-15]. Another system of interest in photovoltaics, Cu(In,Ga)Se_2, is known to benefit from Cu-rich intermediate growth stages and from the presence of alkali elements such as Na, K, and Rb. Therefore, this material was studied at LISA to study local structural parameters as a function of the final Cu content, varying history of the Cu content, and varying alkali treatment [Sch-18]. Results point to the negligible influence of the presence of alkali ions on the bulk structural properties of the films, which are mainly dependent on the Cu content. Very interestingly, XAS can be used to study organic compounds of interest in photovoltaics, particularly in dye-sensitized solar cells. An example are phtalocyanines, which have been studied in the case of Fe, Co, Cu and Zn containing ones [Ros-16]. In this field, it is very important to investigate the local atomic and electronic structure to understand the relevant optoelectronic properties. To this aim, K-edge spectra were recorded and their interpretation allowed to observe consistent variations of bond lengths and Debye Waller factors in dependence on the atomic number of the metal ion, which indicates a variation of the metal–ligand bond strength correlated to the spatial arrangement and occupation of molecular orbitals. As mentioned, sunlight can be exploited to drive chemical reaction, either to produce species with high added value or energy vectors like hydrogen. Also in this case, materials science is developing new synthetic methods for shape controlled nanostructures as well as multilayer, composite materials. An example of the first case is the synthesis of Co_3O_4 sea urchinlike nanostructures, obtained by pulsed laser deposition, which underwent a complete structural investigation that included XAS to reveal the complex growth mechanism [Mau-18]. For what concerns operando experiments, most of the work at LISA was dedicated to the study of photoanodes and photocathodes for photoelectrochemical water splitting. To this aim, a novel spectroelectrochemical cell was designed and created by means of 3D printing [Ach-16]. For what concerns photocathodes, the research was focused on Cu-based oxides and particularly on CuO, a promising system with higher stability than Cu_2O. The reasons behind this were disclosed thanks to FEXRAV and by ex-situ XAS (before and after use): CuO undergoes partial reduction to Cu_2O but is not further reduced to Cu (at least in the investigated potential window) [Bar-16.2]. Operando XANES was also adopted for the investigation of the role of overlayers in multilayer photoanodes, in the particular case of α-Fe_2O_3/IrO_x [Bar-16, Min-17]. This system was initially studied in steady state, recording differential spectra at the Ir L_{III} edge in the dark and under 400 nm LED illumination. This was possible thanks to a unique feature at LISA: for each energy value the acquisition was performed both in the presence and in the absence of UV-Vis light before stepping the monochromator to a higher energy value (stepping mode). This approach allows to (i) minimize possible systematic errors and (ii) avoid severe data manipulation (e.g. background subtraction) whose effect on the two spectra could “mask” the small differences under light and in the dark. This method allowed to directly observe electron and hole transfers from the illuminated semiconductor to the overlayer. The nature of the transferred charge depends on the applied potential, as shown in Figure 45-3 [Min-17]. A similar system was also studied with time resolved XAS in the first operando pump & probe XAS experiment in photoelectrochemistry. In this case, experiments were carried out with the storage ring operating in 4 bunches mode with a bunch spacing of 700 ns and a pulse duration of 100 ps whereas UV flashes had a duration of 60 ns. The pump (UV) and the probe (X-rays) were delayed for 0 or 600 ns. The results demonstrate the occurring of a hole transfer from the semiconductor to the IrOx overlayer under conditions in which anodic photocurrents are observed, with an increase of the number of transferred hole that is higher for the high delay time (Figure 45-4). On the other hand, for lower applied potentials, we could observe a partial reduction of Ir, a phenomenon that starts with the charge transfer and is followed by the adaptation of the oxide structure after 600 ns [Bar-16].

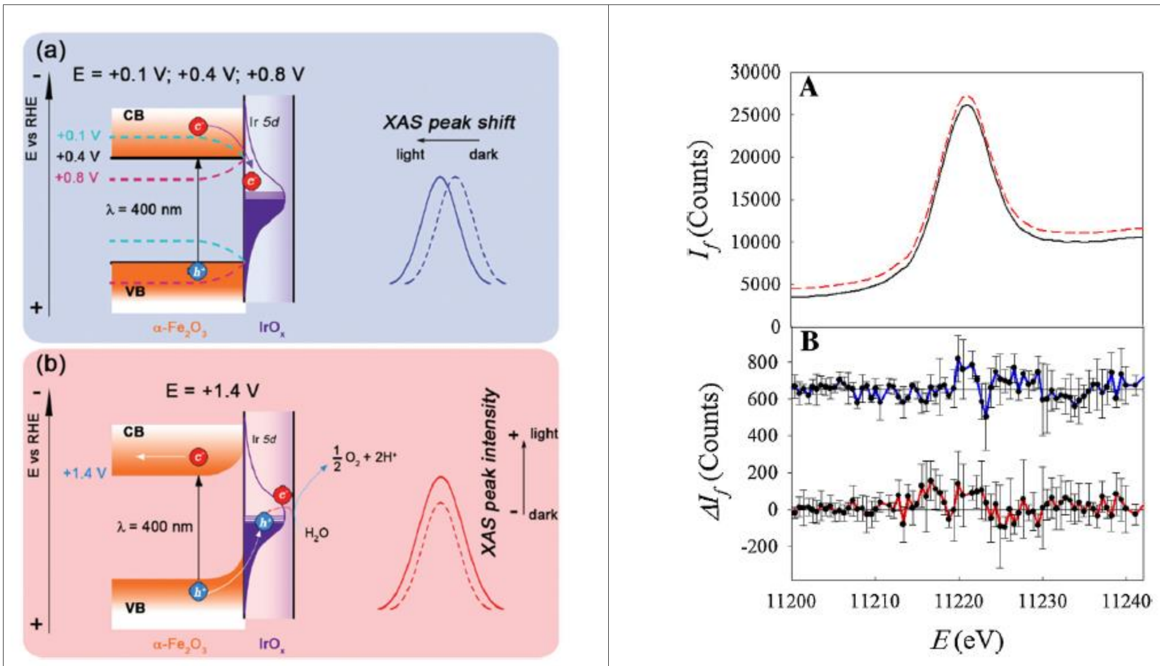

3

4

Figure 45: (3): Schematic representation of the energy diagram of the a-Fe$_2$O$_3$/IrO$_x$/electrolyte junctions at different applied potentials ((a) 0.1, 0.4 and 0.8 V and (b) 1.4 V vs. RHE) and the relevant change of the Ir L$_{III}$ XANES peak. Reprinted from [Min-17]. (4): (A) Ir-L$_{III}$ XANES spectrum in presence (red dotted line) and in absence (black full line) of 400 nm light acquired in presence of 600 ns delay between the pump and the probe; the two spectra were shifted along the y axis for the sake of better clarity. (B) difference spectra (light on-light off) and related error bars in presence (red line) and in absence (blue line) of delay; the two spectra are shifted for clarity, and the zero is defined by the horizontal lines. Reprinted from [Bar-16], with the permission of Elsevier.

7.6.3. Thermoelectric materials

Materials capable of convert heat into electric energy have been also studied at LISA mainly to study the role of dopants. In fact, it is known that dopants are potentially able to improve the thermoelectricity functional properties by injecting mobile carriers, increasing phonon disorder, and modulate the band structure.

Strontium barium niobate (SBN), undoped or heavily doped with K, Y, Zr and Mo was studied in the transmission mode, by mixing with cellulose to form pellets [Ott-17]. Doping ranged in a wide window, up to huge doping [Ott-18]. XAS was adopted to obtain precious information on the Nb charge state and possible injection of charge carriers. Data analysis demonstrated that Nb remains always in a Nb(V) state and that the pre-edge feature is not significantly modified by K- or Mo-doping, but indicates an increase of the empty density of states projected on Nb with Y doping and a decrease with Zr doping.

7.6.4. Batteries

Materials for batteries have been investigated to highlight the role of doping and of lithiation/delithiation in the oxidation state and local structure of the absorbing atom. The most investigated devices are certainly Li batteries, aiming at studying new electrode materials for enhanced energy and power densities and increased safety.

Ex-situ investigations were devoted to the study of Iron and Cobalt Doping on the Structure of Nanosized ZnO [Giu-15]. XAS allowed to prove the effective incorporation of the two dopants into the ZnO structure without the formation of undesired metallic or segregated oxide phases. The case of Fe doping was further investigated to unravel its role upon discharge, when it partially reduces to Fe^{2+} [Giu-18]. Moreover, it was demonstrated that Li^{+} insertion is possible thanks to the presence of cation vacancies. Similarly, XAS was adopted to investigate the role of Ni and Mn doping in V_2O_5 bilayers prepared as aerogels (i.e. removing the synthesis solvent under supercritical conditions) introducing a sonication step [Mor-18]. The interest of this work is due to the importance assumed by V_2O_5 in being a promising host material in many type of batteries, i.e. based on Li^{+}, Na^{+}, Al^{3+}, Mg^{2+} ions. Among the studied materials, phosphoolivine $LiMnPO_4$ represents one of the most studied one as cathode material in Li-ion batteries. This materials, synthetized by a rapid microwave-assisted precipitation procedure, was studied by ex-situ XAS at the Mn K-edge to demonstrate that absorbing Mn atoms have only an oxidation state of +2 and that particles of 35 nm (average diameters) present a more disordered structure than 65 nm ones [Voe-16]. Another olivine, iron-doped $LiCoPO_4$ was studied by ex-situ XAS [Bru-17]. The unique properties of XAS allow the parallel study of different absorbing atoms, leading to synergistic information. In this work, XAS was carried out at both the Co K-edge and the Fe K-edge. The paper conclusions report a partial substitution of cobalt ions in the lattice with iron ions, which in turn regulates the long range crystal structure as well as the short range atomic coordination. This has important implication in the Li transport properties. Finally, $ZnFe_2O_4$ electrodes were chosen for the study of the solid electrolyte interphase (SEI), a key player in the efficiency of Li-ion batteries in that prevents further decomposition phenomena [Rez-16]. Using an As containing electrolyte, $LiAsF_6$, and thanks the penetration depth of the X-ray beam at the As K-edge, XAS was used to study the lithiation process and local structure of the formed phases on the SEI layer. This study was possible thanks to the availability of a multielement Ge detector, to be used in the fluorescence mode because of the small concentration of As in the samples. As K-edge spectra were collected at different stages of the SEI formation. Combined XANES results point to the co-presence of different oxidation states of As, Figure 46-5 and Figure 46-6, as can be explained by the equations:

$$LiAsF_6 + 2Li^{+} + 2e^{-} \rightarrow 3LiF + AsF3 \qquad (3)$$

$$AsF_3 + 2xLi^{+} + 2xe^{-} \rightarrow xLiF + LixAsF_{3\text{-}}x \qquad (4)$$

XANES and EXAFS demonstrate that, during the SEI formation, the As oxidation state and its local coordination varies. EXAFS analysis of the cycled electrodes has shown the presence of a well-defined shell of As second neighbors confirming the reoxidation of the SEI structure after prolonged charge−discharge cycling.

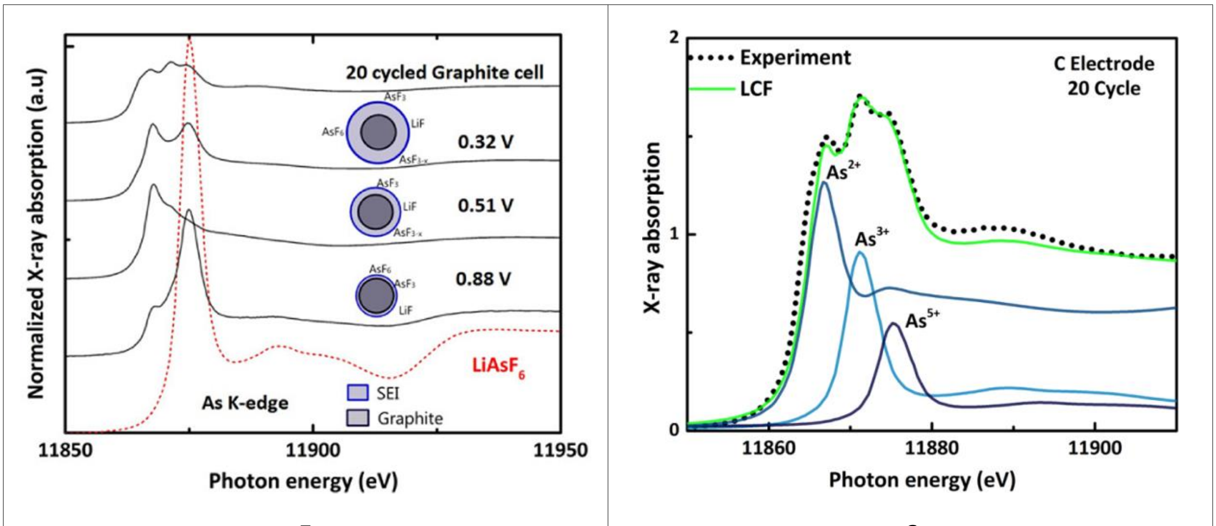

5

6

Figure 46: (5): Normalized XANES spectra of the graphite electrodes along with the electrolyte salt solution LiAsF$_6$ spectra shown as the reference. All of the spectra are normalized to one with a constant offset for better visibility, while the LiAsF$_6$ spectrum is multiplied by a constant (×2). (6): Linear combination fitting (LCF) of the XANES spectrum (graphite electrode 20C). Three reference spectra of As^{5+} (LiAsF$_6$), As^{3+} (As$_2$O$_3$), and As^{2+} (AsS), with typical peak energies of 11874.8, 11871.6, and 11867.5 eV, respectively, were considered. Both figures are reprinted from [Rez-16], with the permission of the American Chemical Society.

7.7 Nanostructures for optical and magnetic applications

Chiara Maurizio Physics and Astronomy Department, University of Padova, Italy

The optical properties of composite nanostructured materials can depend on their structure at the atomic or sub-nm scale level. The photoluminescence (PL) of few-atom metal clusters is an example, as well as the magneto-optical response of nanostructured alloy of a magnetic element with a plasmonic one. To this respect, XAS allows to make the link between these peculiar properties and the structure of the system at the atomic level. Selected case studies of the research performed at the BM08 beamline on this topic are discussed in the following. Moreover, XAS, combined (*in-situ*) with X-ray Diffraction, has also been used to investigate the size-dependent structural transformations of nanostructures induced by heating. BM08 has been demonstrated to be specifically suitable for these investigations, whose crucial points have been: (i) to deal with the sample dilution (down to 1-few at % in a 100-nm thick layer, for the investigation of few-atom clusters in silica); (ii) to combine *in-situ* XAS-XRD analysis (investigation of the dehydrogenation of NbH clusters); (iii) to measure the Ag K-edge and the Au L_3-edge in the same experiment (investigation of sub-nm Au-Ag alloy clusters).

7.7.1. Few-atom metal clusters for Er^{3+} 1.54 μm emission.

The first steps of cluster aggregation in solid matrices are very interesting not only to achieve full control of the cluster size in the nanometer range, but also because the electronic energy levels of few-atom clusters do not exhibit a metallic character and are size dependent. These composite materials are prototypical systems for optoelectronic and photovoltaic applications. Ion implantation into silica has been used to produce Au sub-nanometer metal clusters, whose size can be finely tuned from few-atom to about 1 nm, by acting on the implantation fluence and post-implantation annealing conditions. The structural analyses rely basically on x-ray absorption spectroscopy, that can investigate the metal site independently from long range order considerations. To this respect, since DFT theoretical calculations suggest for few-atom clusters made of Au a power-law dependence of the average nearest neighbor distance on the cluster size, the average cluster size can be retrieved from the first shell distance measured by XAS. These experiments are challenging due to sample dilution (down to 1-few at. % in a ≈100 nm-thick layer). XAS experiments have been performed at BM08 on Au-implanted silica and Au-implanted Er-doped silica. The implantation dose was varied in the range 7×10^{14}-3×10^{15} Au^+/cm^2) [Mau-15]. Au aggregation was promoted by specific annealing treatments (in inert or reducing atmosphere, at selected temperature values in the range 300-800°C). The Au fluorescence signal was collected by a 13-element high-purity Ge detector. The samples were cooled down at 80 K to avoid radiation damage and to reduce as much as possible the thermal vibrations. Due to sample dilution, a couple of (111) Si crystals in sagittal focusing configuration was used, that ensured the photon flux needed for the measurement. Harmonics rejection was achieved by a couple of Pd-coated mirror (incidence angle = 3 mrad). In Figure 47-1 a selection of Au L_3-edge EXAFS spectra measured after annealing at increasing temperature are shown as an example [Mau-15]. The first shell EXAFS analysis was based on the FEFF8 package and allowed to estimate, from the interatomic distance contraction, the average cluster size in different samples. This allowed first to monitor the first steps of the cluster growth upon heating (from few-atom clusters to about 1 nm clusters). As a second point, the cluster size has been related with the energy position of the Vis-IR photoluminescence bands recorded from the Au clusters (a typical PL signal from Au is shown in Figure 47-2) [Ces-14].

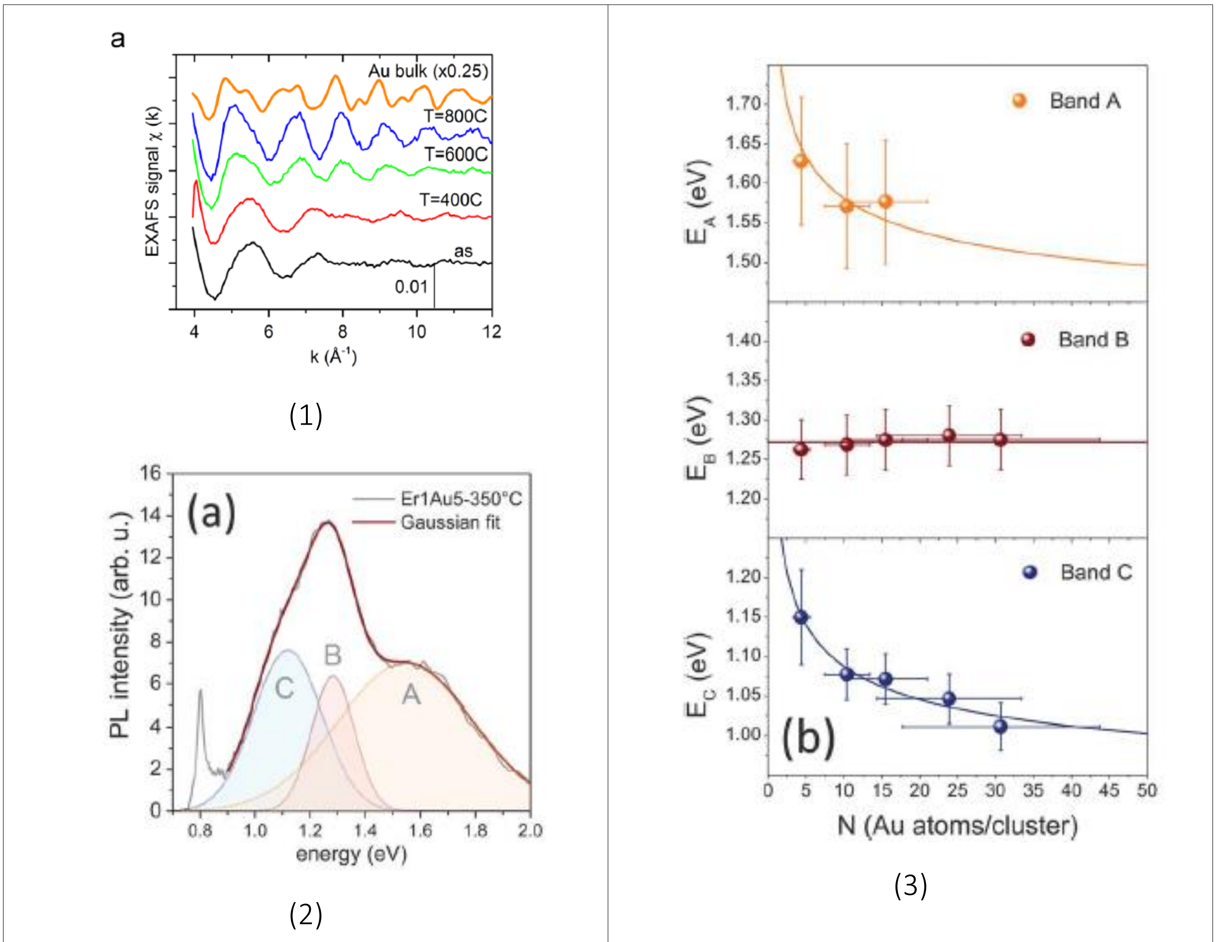

(1)

(2)

(3)

Figure 47: Figure NS-1: EXAFS spectra from Au clusters obtained by ion implantation in Er—doped silica, after inert annealing (1 h) at selected temperatures, compared to the spectrum of metallic Au [Mau-15]. Figure NS-2: 488 nm-excited photoluminescence from Au clusters embedded in Er-doped silica by ion implantation (Au fluence = 3×10^{15} at/cm^2, annealed for 1h at 350 °C in N_2 atmosphere). The three Gaussian bands obtained from the fit are shown [Ces-14]. Figure NS-3: Emission energy corresponding to the maximum of each PL band as a function of the number of Au atoms per Au cluster (N), estimated from the nearest neighbour distance obtained by XAS analysis [Ces-14].

In Figure 47-3, the energy position of each of the three bands is shown as a function of the Au cluster size (from XAS) in different samples. The results indicate for bands A and C a definite dependence of the maximum emission energy on the inverse of the cluster radius, or equivalently $E_{A;C} \approx 1/N^{1/3}$, according to the quantum size effect (intraband and interband electronic transitions). Conversely, no dependence on the Au cluster sizes has been revealed for band B. The physical origin of this band has been ascribed to the local coordination with oxygen of the gold atoms in the outer shell of the Au clusters, i.e. to the luminescence from surface states that is not expected to shift in energy with the cluster size. [Ces-14.1]. XAS analysis supports this idea, showing that, besides the signal from the intermetallic coordination, for small clusters and low annealing temperature a correlation of the dopant with oxygen atoms from the matrix is found, especially upon implantation at low fluence [Mau-15].

By correlating XAS with photoluminescence spectroscopy, it has been previously shown that clusters of a few Au atoms in silica absorb energy in the visible-UV range and can efficiently transfer part of it to nearby Er^{3+} ions, dramatically increasing the rare earth effective excitation cross-section, with promising photonic applications. The systematic XAS analysis (Au-edge) coupled with the PL measurements for a silica matrix doped with Au clusters and Er ions, suggests that the B band, related to cluster surface states, is resonant with the corresponding absorption transition ($^4I_{15/2}$–$^4I_{11/2}$) of Er^{3+} ions in silica, thus being this a preferential channel for the transfer of energy from the ultra-small Au clusters to the Er ions [Ces-14.1, Ces15].

The effectiveness of the energy transfer from small metal clusters to Er ions in silica has been also studied as a function of the metal composition. In particular, multiple implantations of Au and Ag ions in pure silica and Er-doped silica matrices have been performed to promote the formation of small Au–Ag alloy clusters. Upon annealing in N_2 atmosphere at 600 °C the structural investigation based on XAS at Au L_3 and Ag K edges detected the formation of Au–Ag alloy clusters, whose size is likely below 1 nm. The alloy composition is rich in Au; a minor part of Au atoms remains dispersed into the matrix and oxidized. When the implantation is made in the Er-doped silica, the presence of these small alloy aggregates promotes a strong enhancement of the Er^{3+} luminescence, that is more marked with respect to similarly produced layers where only pure Au sub-nanometer clusters were present [Mau-14, Ces-15.1].

7.7.2. Thermally-induced modification of nanostructures.

Experiments at the BM08 beamline allowed to monitor *in-situ* the structural changes of different kind of nanostructures, induced by specific annealing conditions, using both XAS and XRD on the same sample. One example is the investigation of the hydrogen desorption from NbH clusters (NbH->Nb phase transition) upon annealing in vacuum [Mau-15.1]. A second example is the investigation of the growth mechanism of Co_3O_4-based hierarchical nanostructures [Mau-18].

For the first case, the setup to perform a combined XAS-XRD *in-situ* analysis is shown in Figure 48-4. A monochromatic X-ray beam (18 keV, sagittal focusing (311) Si monochromator, a couple of Pt-coated mirrors to reject higher harmonics) impinged on a capillary where the NbH nanoclusters in Mg matrix were placed. The sample temperature was controlled by a gas blower. The powder diffraction spectrum was measured using an imaging plate (exposure time less than 1 min). After that, the x-ray energy was scanned through the Nb K-edge and the XAS spectrum was collected by a photodiode (one-few minutes were required). In Figure 48-5 the lattice parameter of the clusters is shown at different steps of the desorption process. While XRD and XAS find the same results at the beginning of the process (NbH0.9 phase) and at the end (metallic Nb phase), during the desorption the interatomic distances measured by XAS are always lower than those measured by XRD. This is the signature that the kinetics is faster for small NbH clusters (that dominate the XAS signal) than for the largest ones (that dominates the XRD signal) [Mau-15.1].

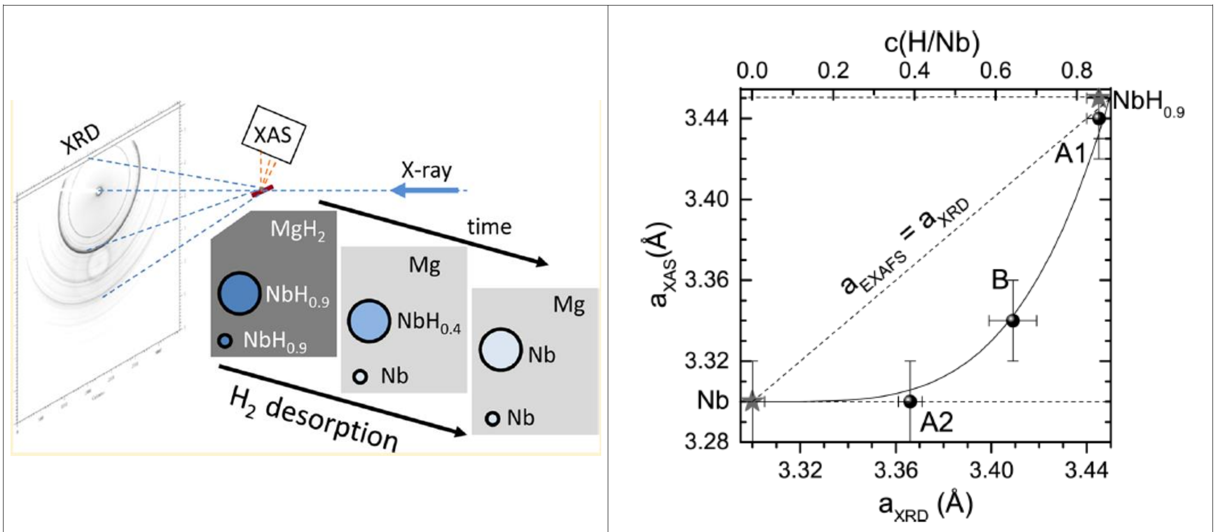

(4)

(5)

Figure 48: (4): Experimental setup for the in-situ XAS–XRD experiment on the dehydrogenation of NbH clusters. As sketched, it is found that the NbH_x cluster composition depends on the cluster size. It is shown for the first time for embedded nanoparticles that faster (and complete) Nb dehydrogenation is favored for small (1.5–4 nm) clusters with respect to larger (~20 nm) ones. [Mau-15.1]. (5). Lattice parameter a of the NbHx bcc phase measured by XAS and XRD during annealing. Data measured at room temperature before and after complete dehydrogenation are also reported (stars); the solid line is a guide for the eye. [Mau-15.1]

For the second (*ex-situ*) example, a XAS experiment on the formation of hierarchical Co_3O_4-based sea-urchin like nanostructures by thermal oxidation of a Co-O-B layer deposited by pulsed laser deposition (PLD), allowed to evidence a two-step growth mechanism [Mau-18], sketched in Figure 49. The as-deposited samples are formed of spheroidal particles on a smooth underneath layer (Figure 49-b). As sketched in Figure 49, the particles can also be separated from the underneath layer and examined by XAS. The experiment has been performed at room temperature at Co K-edge in fluorescence mode. Fourier transform moduli of the EXAFS spectra for the particles and from the full layer are shown in Figure 49-f. XAS results, combined with XRD analysis, allowed to show a crucial role of B for the urchin formation that (i) limits Co oxidation during the deposition process and (ii) induces a chemical reduction of Co, especially in the particle core, in the first step of air annealing (2 h, 500 °C). Then, Co oxidation proceeds and Co atoms out-diffuse from the Co fcc particle core likely through fast diffusion channel present in the shell and form Co_3O_4 nano-needles. [Mau-18]. This investigation shows how diffusion mechanisms and chemical effects can be effectively coupled to obtain hierarchical structures of transition metal oxides. These systems show an enhanced photocatalytic activity for the degradation of methylene blue dye, via a photo-Fenton reaction in presence of H_2O_2 and visible light [Edl-15].

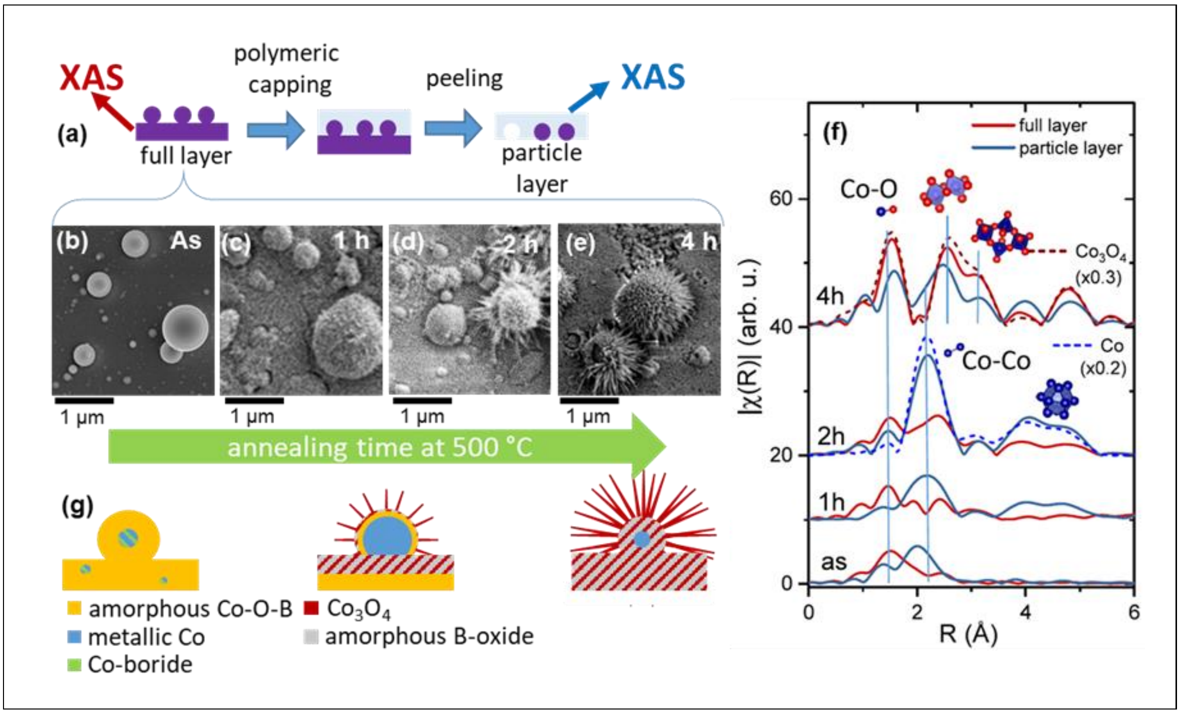

Figure 49: (a) Sketch of the Co-O-B nanostructured samples and of the procedure used to separate the particles from the layer beneath. (b-d) SEM images of the sample after annealing at 500°C for the indicated time. (e)Fourier transform moduli of the EXAFS spectra recorded at Co K-edge from the full layers and particle layers. The spectrum of Co_3O_4 crystalline powder and of metallic Co is also shown. (g) Sketch of the structural evolution of Co-O-B deposited layers upon air annealing at 500 °C, as retrieved by the XAS, XRD and SEM investigations.

7.7.3. Nanostructures of bulk immiscible alloys for magnetoplasmonics

Coupling a plasmonic metal with a magnetic one in thin films and nanostructures is very interesting for the emerging field of magnetoplasmonics. In particular, coupling through alloying is a promising strategy to induce a magnetic moment on the plasmonic metal atoms, in a way that is intimately related to the local structure of the (metastable) alloy material. In this framework, Au-Co bimetallic films have been produced via magnetron co-sputtering deposition, and the local structure has been investigated by XAS at both Au- and Co-edges (Figure 50). The results clearly indicate the formation of a full-metallic layer composed for the major part of a Au-Co mixture, where the Au-Co coordination is relevant [Mau-18.2]. XAS and transmission electron microscopy analyses suggest the presence of a minor fraction of segregated metals. This analysis allowed to correlate the alloy formation to Au magnetic moment measured by an XMCD experiment (ID12-ESRF) on the same samples [Mau-18.2]. This Au-Co magnetic coupling is favored by a high degree of mixing of the two metals in the alloy. In addition, an unexpected hysteretic behavior has been observed, characterized by in-plane anisotropy and crossed branches in the loops measured along the hard magnetization direction. Micromagnetic calculations have been performed to simulate the magnetic response, for a simplified system composed of a AuCo matrix surrounding a Co cluster. The hysteretic features are qualitatively well reproduced provided that the two phases have almost orthogonal anisotropy axes. This requirement can be plausibly fulfilled assuming a dominant magnetoelastic character of the anisotropy in both phases [Chi-17].

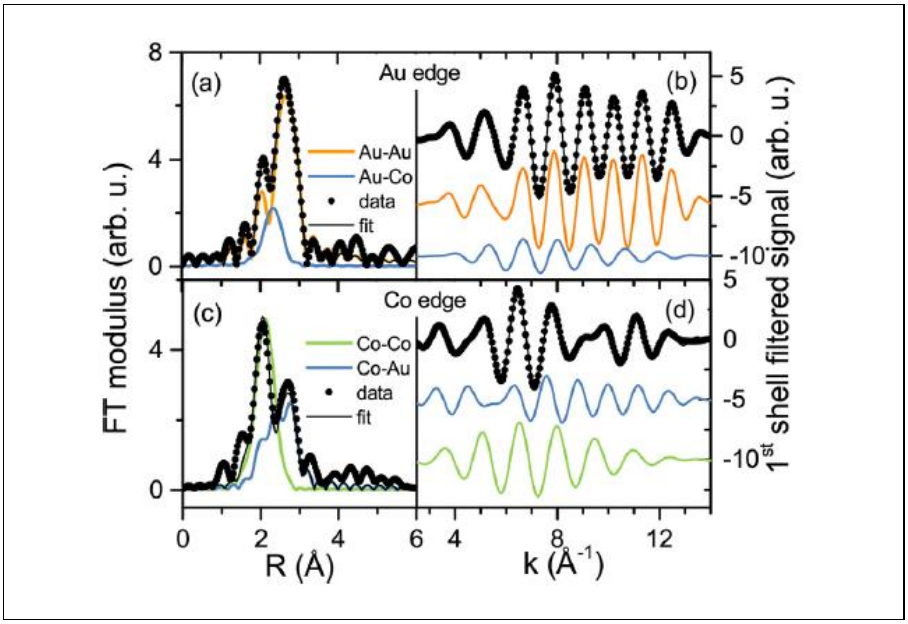

Figure 50: First shell XAS analysis at Au L3-edge (a,b) and Co K-edge of a Au-Co film, 30 nm thick. The multiparameter fits are superimposed to the experimental data in the R-space (a,c) and k-space (b,d). The single scattering contribution to the fit are reported. [Mau-18.2].

7.8 Life Sciences

Alessandro Puri CNR-IOM-OGG, Grenoble (France)

During the period 2014 – 2018 the LISA (BM08) CRG beamline at ESRF has allowed relevant research on nanoparticles and complex molecules of particular interest for biochemistry and medicine, as well as on the association of metals with proteins. In many works X-ray absorption spectroscopy (XAS) has been used in conjunction with other complementary techniques. The studies benefited from the beamline high photon flux which allowed the collection of fluorescence spectra of dilute solutions. Furthermore the availability of two 13- and 12-element HPGe detectors and of a liquid nitrogen bath cryostat which permits to fast load frozen specimens, avoiding sample heating, have been relevant features for the success of the experiments.

7.8.1. Nanoparticles for biological and medical applications.

Laser ablation in liquid (LAL) turned out to be a versatile technique for the synthesis of nanoparticles (NPs) of various structures and compositions. Through several characterization techniques, including fluorescence XAS at Fe K-edge measured at BM08, it has been shown that the addition of phosphonates during laser ablation of iron in water had dramatic effects on the crystallization of the obtained NPs [Fra-18]. The study clarified that phosphonates confined the size of iron oxide domains to only few atoms, resulting in phosphonate grafted iron oxo-clusters polymerized into nanometric particles stably dispersed in water. The result was attributed to the strong ability of phosphonate groups to bind iron oxide clusters and prevent their further growth into crystalline iron oxide. These laser generated poly-oxo-clusters were biocompatible and trackable by magnetic resonance imaging, providing interesting features for use in biological environments, such as nano-vehicles for iron administration.

CeO_2 nanoparticles (CNPs) are under investigation as promising antioxidant agents in the therapy of several diseases involving free radicals or oxidative stress, due to their radical scavenging properties with almost no toxicity. Their scavenging properties have been associated with the equilibrium between the two oxidation states of cerium, Ce(III) and Ce(IV), which is strongly dependent on the external environment/stimuli. The modification of Ce(III)/Ce(IV) ratio in CeO_2 nanoparticles following internalization in human cells has been studied [Fer-17], using X-ray absorption near edge spectroscopy (XANES) at the Ce–L_{III} edge. The spectra were collected at the BM08 beamline in fluorescence mode, using a 13-element Ge detector. The samples, stored at -80 ºC, have been rapidly mounted inside a bath cryostat cooled at 100 K to prevent temperature damage. The XANES analysis on cell pellets revealed a significant increase in Ce(III) for the CNPs incubated for 24 h (Figure 51). Further micro-X-ray fluorescence (µXRF) and Ce L_{III}-edge micro-XANES (µXANES) analysis on individual cells, carried out at ID21 beamline of ESRF, revealed that the Ce(III)/Ce(IV) ratio was also dependent on CNP intracellular localization, with the Ce(IV) more localized in the regions with the highest CNP concentrations and Ce(III) in regions surrounding these areas.

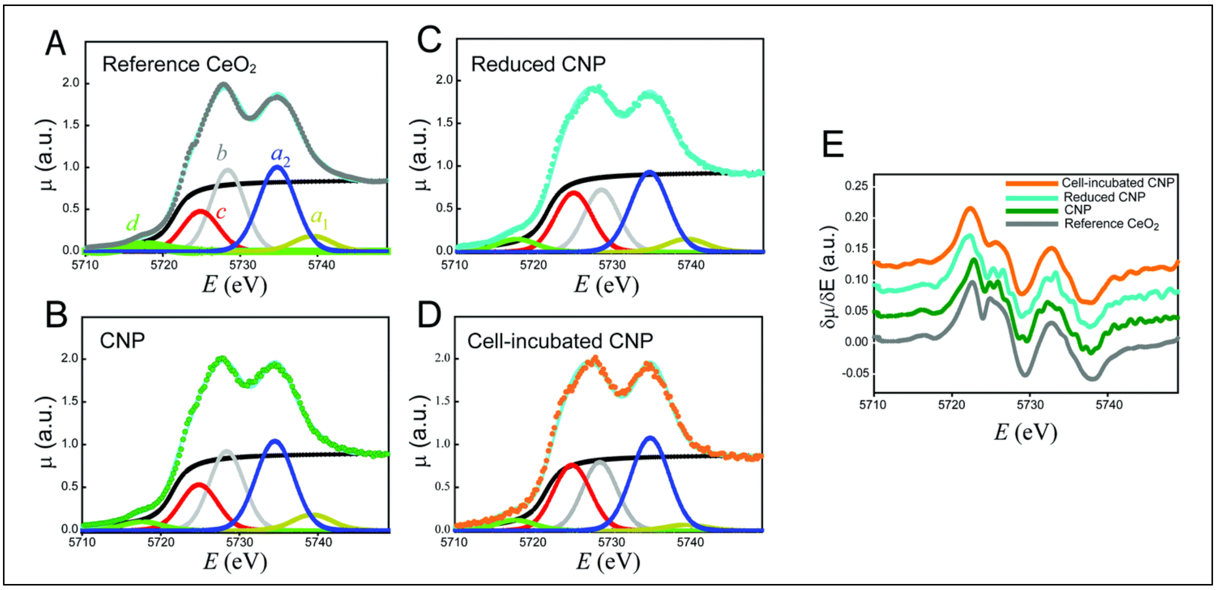

Figure 51: Ce–L$_{III}$ XANES spectra of the reference CeO$_2$ (A), CNPs (B), reduced CNPs (C) and CNPs incubated with cells for 24 h (D). These panels also show the fits relative to the peak components. Panel (E) reports the corresponding derivatives. From [Fer-17]-Published by The Royal Society of Chemistry.

7.8.2. Cu complexes in aqueous solutions

The phosphane Cu(I) complex [Cu(thp)$_4$][PF$_6$], **1** (thp = tris(hydroxymethyl)phosphane), shows notable in vitro antitumour activity against a wide range of solid tumours. XAS and spectrophotometric titrations were utilized to study the speciation of **1** in aqueous solutions at different concentrations, and to determine thermodynamic parameters of **1** and related species [Tis-16], in order to clarify the correlations between the antitumour activity and speciation of **1** in aqueous media. Florescence XAS-EXAFS data collected at BM08 in using a 13-elements high purity Ge detector, revealed that the integrity of the original, four-coordinated [Cu(thp)$_4$]$^+$ cation was lost at micromolar concentrations, through the release of at least one phosphane ligand and formation of the coordinative unsaturated [Cu(thp)$_n$]$^+$ (n = 3 and 2) species.

The chemistry of copper(I) with water-soluble phosphines is an emergent area of study which has the objective of finding ligands that stabilize copper in its lower oxidation state. The ability of PTA (PTA = aminophosphine-1,3,5-triaza-7-phosphaadamantane) to solubilize transition metal complexes in aqueous phase made these compounds ideal candidates for catalysis and medicinal chemistry applications. The [Cu(PTA)$_n$]$^+$ (n = 2 – 4) complex stability and speciation in aqueous medium has been studied by means of UV–visible spectrophotometry and XAS. In particular XAS was used to probe the average coordination environment of Cu [Qua-18]. XAS spectra at the Cu K-edge have been collected at BM08 in fluorescence mode in fluorescence mode using a 13-element hyper-pure Ge detector. The analysis suggested that the $[Cu(PTA)_n]^+$ species were stable in solution, among which $[Cu(PTA)_2]^+$ had a remarkable thermodynamic stability. XAS data showed that Cu(I) in the latter species did not strictly possess a coordination number of 2, since water molecules were partially coordinated to the metal along with the two phosphines.

7.8.3. Metals (Zn, Cu) interaction with water and proteins

The Parkinson's disease (PD) is connected to the presence of abnormal α-synuclein (αS) protein deposits in the brain. It has been suggested that the βS/αS ratio, βS belonging to the same synuclein family, is altered in PD, indicating that a correct balance of these two proteins is implicated in the inhibition of αS aggregation. The interaction of Cu(I) with the N-terminal portion of βS and αS has been investigated by means of NMR, circular dichroism, and X-ray absorption spectroscopies [Der-15]. Cu Kα fluorescence XAS spectra were collected at the BM08 beamline of ESRF, using a Ge 12-element solid-state detector. A glovebox under inert atmosphere was used to load the sample into a plastic cell covered with Kapton windows. The sample cell was then mounted in a cryostat and kept at 100 K during data collection. XAS analysis provided evidence of different Cu(I) chemical environment for the Cu(I)−αS and Cu(I)−βS complexes, indeed the Cu site coordination was found to be 2S2O and 3S1O in αS and βS, respectively (Figure 52).

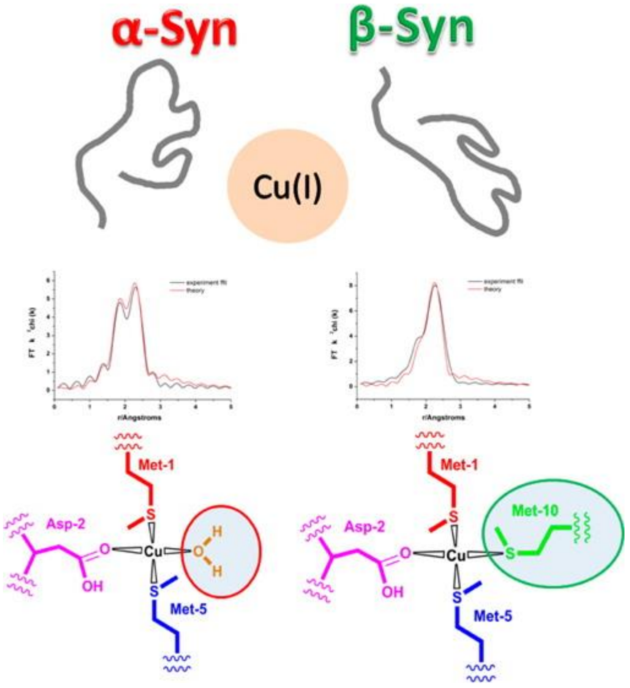

Figure Bio-02

Figure 52: Fourier transforms of the k^2-weighted EXAFS data of Cu(I)−αS (left) and Cu(I)−βS (right) with a schematic view of the Cu binding site. Reprinted with permission from [Der-15]. Copyright 2015 American Chemical Society.

Mussel byssal threads represent an example of protein-based biofibers in which hierarchical organization of protein building blocks coupled via metal complexation leads to notable mechanical behaviors, such as high toughness and self-healing. Using a natural amino acid sequence from byssal thread proteins, Jehle et al. [Jeh-18] created free-standing peptide films with complex hierarchical organization across multiple length scales, which could be controlled by inclusion of metal ions (Zn^{2+} and Cu^{2+}) during the assembly process. The specific histidine metal coordination environment in peptide films containing Zn was investigated by XAS spectroscopy. Zn K-edge fluorescence spectra were collected at BM08 using a 12- element Ge detector. During data collection, the samples were kept at a temperature of 83 K to reduce the thermal molecular vibrations and beam damage. XAS data indicated that Zn was tetrahedrally coordinated by four ligands. Combined XRD, FTIR, Raman and XAS spectroscopy studies evidenced that pepetides spontaneously assembled into hierarchically organized amyloid like β-sheet structures within free-standing films. Moreover film containing Zn ions had both a higher degree of hierarchical order and significantly higher mechanical performance respect to those containing Cu ions, suggesting a possible correlation between these two parameters.

After iron, zinc is the second most abundant transition metal in living organisms. Detailed knowledge of zinc ion chemistry is essential for understanding its role in biology. A multi-scale theoretical approach aimed at calculating from first principles X-ray absorption spectra of liquid solutions and disordered systems has been developed and tested with the case of Zn(II) in water [Ste-18]. The XANES spectrum of Zn(II) in water calculation has been performed from first principles in a completely parameter-free way and compared with the experimental Zn K-edge XANES data collected at BM08 in fluorescence mode on a $ZnCl_2$ salt dissolved in deionized water. The comparison unambiguously showed that among the different a priori possible geometries, Zn(II) in water lives in an octahedral coordination mode.

8. Bibliography

8.1 LISA specific bibliography

[Ach-16] Achilli E., Minguzzi A., Visibile A., Locatelli C., Vertova A., Naldoni A., Rondinini S., Auricchio F., Marconi S., Fracchia M., Ghigna P. - 3D-printed photo-spectroelectrochemical devices for in situ and in operando X-ray absorption spectroscopy investigation Journal of Synchrotron Radiation 23, 622-628 (2016)

[Afi-17] Afify N.D., Mountjoy G., Haworth R. - Selecting reliable interatomic potentials for classical molecular dynamics simulations of glasses: The case of amorphous SiO2 Computational Materials Science 128, 75-80 (2017)

[Alb-17] Alberti A., Cruciani G., Martucci A. - Reconstructive phase transitions induced by temperature in gmelinite-Na zeolite American Mineralogist 102, 1727-1735 (2017)

[Ame-15] Amendola V., Scaramuzza S., Agnoli S., Granozzi G., Meneghetti M., Campo G., Bonanni V., Pineider F., Sangregorio C., Ghigna P., Polizzi S., Riello P., Fiameni S., Nodari L. - Laser generation of iron-doped silver nanotruffles with magnetic and plasmonic properties Nano Research 8, 4007-4023 (2015)

[Bae-18.2] Baekelant, W.; Aghakhani, S.; Coutino-Gonzalez, E.; Grandjean, D.; Kennes, K.; Jonckheere, D.; Fron, E.; d'Acapito, F.; Longo, A.; Lievens, P. ; Roeffaers, M.B.J.; Hofkens, J., Confinement of Highly Luminescent Lead Clusters in Zeolite A, JOURNAL OF PHYSICAL CHEMISTRY C122 (2018) 13953-13961.

[Bae-18] Baekelant W., Aghakhani S., Coutiño-Gonzalez E., Kennes K., Grandjean D., Van der Auweraer M., Lievens P., Roeffaers M.B.J., Hofkens J., Steele J.A. - Shaping the optical properties of silver clusters inside zeolite A via Guest–Host–Guest Interactions Journal of Physical Chemistry Letters 9, 5344-5350 (2018)

[Bal-16] Balerna A., Evangelisti C., Psaro R., Fusini G., Carpita A. - Structural characterization of bimetallic Pd-Cu vapor derived catalysts Journal of Physics : Conference Series 712, 012057-1-012057-4 (2016)

[Bal-17] Balerna A., Evangelisti C., Tiozzo C. - XAFS structural characterization of Cu vapour derived catalysts supported on poly-4-vinylpyridine and carbon X-Ray Spectrometry 46, 82-87 (2017)

[Bar-16.2] Baran T., Wojtyla S., Lenardi C., Vertova A., Ghigna P., Achilli E., Fracchia M., Rondinini S., Minguzzi A. - An efficient CuxO photocathode for hydrogen production at neutral pH: New insights from combined spectroscopy and electrochemistry ACS Applied Materials & Interfaces 8, 21250-21260 (2016)

[Bar-16] Baran T., Fracchia M., Vertova A., Achilli E., Naldoni A., Malara F., Rossi G., Rondinini S., Ghigna P., Minguzzi A., d'Acapito F. - Operando and time-resolved X-ray absorption spectroscopy for the study of photoelectrode architectures Electrochimica Acta 207, 16-21 (2016)

[Bat-14] Battocchio C., Fratoddi I., Fontana L., Bodo E., Porcaro F., Meneghini C., Pis I., Nappini S., Mobilio S., Russo M.V., Polzonetti G. - Silver nanoparticles linked by a Pt-containing organometallic dithiol bridge: Study of local structure and interface by XAFS and SR-XPS Physical Chemistry - Chemical Physics 16, 11719-11728 (2014)

[Ben-15] Benedetti F., Luches P., Spadaro M.C., Gasperi G., D'Addato S., Valeri S., Boscherini F. - Structure and morphology of silver nanoparticles on the (111) surface of cerium oxide Journal of Physical Chemistry C 119, 6024-6032 (2015)

[Ben-16] Benedetti C., Cazzolaro A., Carraro M., Graf R., Landfester K., Gross S., Muñoz-Espí R. - Dual role of zirconium oxoclusters in hybrid nanoparticles: Cross-linkers and catalytic site ACS Applied Materials & Interfaces 8, 26275-26284 (2016)

[Ben-17] Benedetti F., Luches P., D'Addato S., Valeri S., Nicolini V., Pedone A., Menziani M.C., Malavasi G. - Structure of active cerium sites within bioactive glasses Journal of the American Ceramic Society 100, 5086-5095 (2017)

[BenF-16] Benzi F., Giuli G., Della Longa S., Paris E. - Vanadium K-edge XANES in vanadium-bearing model compounds: A full multiple scattering study Journal of Synchrotron Radiation 23, 947-952 (2016)

[Bia-16] Biagioni C., Bonaccorsi E., Lezzerini M., Merlino S. - Thermal behaviour of Al-rich tobermorite European Journal of Mineralogy 28, 23-32 (2016)

[Bia-17] Biagioni C., D'Orazio M., Lepore G.O., d'Acapito F., Vezzoni S. - Thallium-rich rust scales in drinkable water distribution systems: A case study from northern Tuscany, Italy Science of the Total Environment 587-588, 491-501 (2017)

[Bic-17] Bicocchi G., Vaselli O., Ruggieri G., Bonini M., Tassi F., Buccianti A., Di Benedetto F., Montegrossi G. - Chemical alteration and mineral growth under high pCO2 conditions: Insights from the mineral chemistry of carbonate phases in the Caprese Reservoir (Northern Apennines, central Italy) Chemical Geology 450, 81-95 (2017)

[Bon-14] Bonadiman C., Nazzareni S., Coltorti M., Comodi P., Giuli G., Faccini B. - Crystal chemistry of amphiboles: Implications for oxygen fugacity and water activity in lithospheric mantle beneath Victoria Land, Antarctica Contributions to Mineralogy and Petrology 167, 984-1-984-17 (2014)

[Bru-17] Brutti S., Manzi J., Meggiolaro D., Vitucci F.M., Trequattrini F., Paolone A., Palumbo O. - Interplay between local structure and transport properties in iron-doped LiCoPO4 olivines Journal of Materials Chemistry A 5, 14020-14030 (2017)

[Cab-15] Caby B., Brigidi F., Ingerle D., Nolot E., Pepponi G., Streli C., Lutterotti L., André A., Rodríguez G., Gergaud P., Morales M., Chateigner D. - Study of annealing-induced interdiffusion in In2O3/Ag/In2O3 structures by a combined X-ray reflectivity and grazing incidence X-ray fluorescence analysis Spectrochimica Acta B 113, 132-137 (2015)

[Cen-15.1] Centomo P., Meneghini C., Sterchele S., Trapananti A., Aquilanti G., Zecca M. - In situ X-ray absorption fine structure spectroscopy of a palladium catalyst for the direct synthesis ofhydrogen peroxide: Leaching and reduction of the metal phase in the presence of bromide ions ChemCatChem 7, 3712-3718 (2015)

[Cen-15] Centomo P., Meneghini C., Sterchele S., Trapananti A., Aquilanti G., Zecca M. - EXAFS in situ: The effect of bromide on Pd during the catalytic direct synthesis of hydrogen peroxide Catalysis Today 248, 138-141 (2015)

[Ces-14.1] Cesca T., Maurizio C., Kalinic B., Scian C., Trave E., Battaglin G., Mazzoldi P., Mattei G. - Luminescent ultra-small gold nanoparticles obtained by ion implantation in silica Nuclear Instruments and Methods in Physics Research B 326, 7-10 (2014)

[Ces-14] Cesca T., Kalinic B., Maurizio C., Scian C., Battaglin G., Mazzoldi P., Mattei G. - Near-infrared room temperature luminescence of few-atom Au aggregates in silica: A path for the energy-transfer to Er3+ ions Nanoscale 6, 1716-1724 (2014)

[Ces-15.1] Cesca T., Kalinic B., Michieli N., Maurizio C., Trapananti A., Scian C., Battaglin G., Mazzoldi P., Mattei G. - Au-Ag nanoalloy molecule-like clusters for enhanced quantum efficiency emission of Er3+ ions in silica Physical Chemistry - Chemical Physics 17, 28262-28269 (2015)

[Ces-15] Cesca T., Kalinic B., Maurizio C., Scian C., Trave E., Battaglin G., Mazzoldi P., Mattei G. - Correlation between room temperature luminescence and energy-transfer in Er-Au co-implanted silica Nuclear Instruments and Methods in Physics Research B 362, 68-71 (2015)

[Cha-18] Chahal R., Starecki F., Doualan J.L., Němec P., Trapananti A., Prestipino C., Tricot G., Boussard-Pledel C., Michel K., Braud A., Camy P., Adam J.L., Bureau B., Nazabal V. - Nd3+:Ga-Ge-Sb-S glasses and fibers for luminescence in mid-IR: Synthesis, structural characterization and rare earth spectroscopy Optical Materials Express 8, 1650-1-1650-22 (2018)

[Chi-17] Chinni F., Spizzo F., Montoncello F., Mattarello V., Maurizio C., Mattei G., Del Bianco L. - Magnetic hysteresis in nanocomposite films consisting of a ferromagnetic AuCo alloy and ultrafine Co particles Materials 10, 717-1-717-16 (2017)

[Cic-15] Cicconi M.R., Giuli G., Ertel-Ingrisch W., Paris E., Dingwell D.B. - The effect of the [Na/(Na+K)] ratio on Fe speciation in phonolitic glasses American Mineralogist 100, 1610-1619 (2015)

[Com-15] Comotti A., Bracco S., Beretta M., Perego J., Gemmi M., Sozzani P. - Confined polymerization in highly ordered mesoporous organosilicas Chemistry - A European Journal 21, 18209-18217 (2015)

[Cos-14] Costanzo T., Benzi F., Ghigna P., Pin S., Spinolo G., d'Acapito F. - Studying the surface reaction between NiO and Al2O3 via total reflection EXAFS (ReflEXAFS) Journal of Synchrotron Radiation 21, 395-400 (2014)

[Dac-14.1] d'Acapito F., Mazziotti Tagliani S., Di Benedetto F., Gianfagna A. - Local order and valence state of Fe in urban suspended particulate matter Atmospheric Environment 99, 582-586 (2014)

[Dac-14] d'Acapito F., Blanc W., Dussardier B. - Different Er3+ environments in Mg-based nanoparticle-doped optical fibre preforms Journal of Non-Crystalline Solids 401, 50-53 (2014)

[Dac-16.1] d'Acapito F., Souchier E., Noé P., Blaise P., Bernard M., Jousseaume V. - Chemical state of Ag in conducting bridge random access memory cells: A depth resolved X-ray absorption spectroscopy investigation Journal of Physics : Conference Series 712, 012046-1-012046-4 (2016)

[Dac-16.2] d'Acapito F., Souchier E., Noé P., Blaise P., Bernard M., Jousseaume V. - Role of Sb dopant in Ag:GeSx-based conducting bridge random access memories Physica Status Solidi (a) 213, 311-315 (2016)

[Dac-16.3] d'Acapito F., Torrengo S., Xenogiannopoulou E., Tsipas P., Marquez Velasco J., Tsoutsou D., Dimoulas A. - Evidence for Germanene growth on epitaxial hexagonal (h)-AlN on Ag(1 1 1) Journal of Physics Condensed Matter 28, 045002-1-045002-8 (2016)

[Dac-16.4] d'Acapito F., Trapananti A., Puri A. - LISA: The italian CRG beamline for x-ray absorption spectroscopy at ESRF Journal of Physics: Conference Series 712, 012021-1-012021-4 (2016)

[Dac-16] d'Acapito F., Pelli-Cresi S., Blanc W., Benabdesselam M., Mady F., Gredin P., Mortier M. - The incorporation site of Er in nanosized CaF2 Journal of Physics Condensed Matter 28, 485301-1-485301-7 (2016)

[Dac-19] F. d’Acapito, G. O. Lepore, A. Puri, A. Laloni, F. la Manna, E. Dettona, A. de Luisa. A. Martin, The LISA beamline at ESRF, J. Synchrotron Radiat. **26** (2) 2019.

[Der-15] De Ricco R., Valensin D., Dell'Acqua S., Casella L., Gaggelli E., Valensin G., Bubacco L., Mangani S. - Differences in the binding of copper(I) to α- and β-synuclein Inorganic Chemistry 54, 265-272 (2015)

[Dib-14] Di Benedetto F., d'Acapito F., Capacci F., Fornaciai G., Innocenti M., Montegrossi G., Oberhauser W., Pardi L.A., Romanelli M. - Variability of the health effects of crystalline silica: Fe speciation in industrial quartz reagents and suspended dusts—insights from XAS spectroscopy Physics and Chemistry of Minerals 41, 215-225 (2014)

[Dib-15] Di Benedetto F., Cinotti S., d'Acapito F., Vizza F., Foresti M.L., Guerri A., Lavacchi A., Montegrossi G., Romanelli M., Cioffi N., Innocenti M. - Electrodeposited semiconductors at room temperature: An X-ray absorption spectroscopy study of Cu-, Zn-, S-bearing thin films Electrochimica Acta 179, 495-503 (2015)

[Dib-16] Di Benedetto F., Bencistà I., d'Acapito F., Frizzera S., Caneschi A., Innocenti M., Lavacchi A., Montegrossi G., Oberhauser W., Romanelli M., Dittrich H., Pardi L.A., Tippelt G., Amthauer G. - Geomaterials related to photovoltaics: A nanostructured Fe-bearing kuramite, Cu3SnS4 Physics and Chemistry of Minerals 43, 535-544 (2016)

[Edl-15] Edla R., Patel N., Orlandi M., Bazzanella N., Bello V., Maurizio C., Mattei G., Mazzoldi P., Miotello A. - Highly photo-catalytically active hierarchical 3D porous/urchin nanostructured Co3O4 coating synthesized by Pulsed Laser Deposition Applied Catalysis B: Environmental 166-167, 475-484 (2015)

[Eic-15] Eiche E., Bardelli F., Nothstein A.K., Charlet L., Göttlicher J., Steininger R., Dhillon K.S., Sadana U.S. - Selenium distribution and speciation in plant parts of wheat (Triticum aestivum) and Indian mustard (Brassica juncea) from a seleniferous area of Punjab, India Science of the Total Environment 505, 952-961 (2015)

[Eva-17] Evangelisti C., Balerna A., Psaro R., Fusini G., Carpita A., Benfatto M. - Characterization of a poly-4-vinylpyridine-supported CuPd bimetallic catalyst for sonogashira coupling reactions ChemPhysChem 18, 1921-1928 (2017)

[Fen-16] Fenwick O., Coutiño-Gonzalez E., Grandjean D., Baekelant W., Richard F., Bonacchi S., De Vos D., Lievens P., Roeffaers M., Hofkens J., Samorì P. - Tuning the energetics and tailoring the optical properties of silver clusters confined in zeolites Nature Materials 15, 1017-1022 (2016)

[Fer-17] Ferraro D., Tredici I.G., Ghigna P., Castillio-Michel H., Falqui A., Di Benedetto C., Alberti G., Ricci V., Anselmi-Tamburini U., Sommi P. - Dependence of the Ce(III)/Ce(IV) ratio on intracellular localization in ceria nanoparticles internalized by human cells Nanoscale 9, 1527-1538 (2017)

[For-14] Fortes L.M., Gonçalves M.C., Pereira J.C., d'Acapito F. - EXAFS study of Er,Yb doped hollow and dense SiO2 microspheres Journal of Non-Crystalline Solids 402, 244-251 (2014)

[For-15] Fornasini P., Grisenti R. - On EXAFS Debye-Waller factor and recent advances Journal of Synchrotron Radiation 22, 1242-1257 (2015)

[Fra-18] Fracasso G., Ghigna P., Nodari L., Agnoli S., Badocco D., Pastore P., Nicolato E., Marzola P., Mihajlovic D., Markovic M., Colic M., Amendola V. - Nanoaggregates of iron poly-oxo-clusters obtained by laser ablation in aqueous solution of phosphonates Journal of Colloid and Interface Science 522, 208-216 (2018)

[FraM-18] Fracchia M., Visibile A., Ahlberg E., Vertova A., Minguzzi A., Ghigna P., Rondinini S. - α- and γ-FeOOH: Stability, reversibility, and nature of the active phase under hydrogen evolution ACS Applied Energy Materials 1, 1716-1725 (2018)

[Fum-14] Fumagalli P., Poli S., Fischer J., Merlini M., Gemmi M. - The high-pressure stability of chlorite and other hydrates in subduction mélanges: Experiments in the system Cr2O3–MgO–Al2O3–SiO2–H2O Contributions to Mineralogy and Petrology 167, 979-1-979-16 (2014)

[Gao-17] Gao Q., Chen J., Sun Q., Chang D., Huang Q., Wu H., Sanson A., Milazzo R., Zhu H., Li Q., Liu Z., Deng J., Xing X. - Switching between giant positive and negative thermal expansions of a YFe(CN)6-based Prussian blue analogue induced by guest species Angewandte Chemie International Edition 56, 9023-9028 (2017)

[Geo-19] L. George, C. Biagioni, G. O. Lepore, M. Lacalamita, G. Agrosì, G. C. Capitani, E. Bonaccorsi, F. d'Acapito The speciation of thallium in (Tl,Sb,As)-rich pyrite. Ore Geology Reviews 107, 364-380 (2019).

[Gib-16] Gibin G., Lorenzetti A., Callone E., Diré S., Dolcet P., Venzo A., Causin V., Marigo A., Modesti M., Gross S. - Smart and covalently cross-linked: Hybrid shape memory materials reinforced through covalent bonds by zirconium oxoclusters ChemPlusChem 81, 338-350 (2016)

[Giu-15] Giuli G., Trapananti A., Mueller F., Bresser D., d'Acapito F., Passerini S. - Insights into the effect of iron and cobalt doping on the structure of nanosized ZnO Inorganic Chemistry 54, 9393-9400 (2015)

[Giu-18] Giuli G., Eisenmann T., Bresser D., Trapananti A., Asenbauer J., Mueller F., Passerini S. - Structural and electrochemical characterization of Zn1−xFexO—effect of aliovalent doping on the Li+ storage mechanism Materials 11, 49-1-49-13 (2018)

[Gius-14] Giustetto R., Seenivasan K., Belluso E. - Asbestiform sepiolite coated by aliphatic hydrocarbons from Perletoa, Aosta Valley Region (Western Alps, Italy): Characterization, genesis and possible hazards Mineralogical Magazine 78, 919-940 (2014)

[Gra-18] Grandjean D., Coutiño-Gonzalez E., Cuong N.T., Fron E., Baekelant W., Aghakhani S., Schlexer P., d'Acapito F., Banerjee D., Roeffaers M.B.J., Nguyen M.T., Hofkens J., Lievens P. - Origin of the bright photoluminescence of few-atom silver clusters confined in LTA zeolites Science 361, 686-690 (2018)

[Gua-15] Gualtieri M.L., Romagnoli M., Pollastri S., Gualtieri A.F. - Inorganic polymers from laterite using activation with phosphoric acid and alkaline sodium silicate solution: Mechanical and microstructural properties Cement and Concrete Research 67, 259-270 (2015)

[Jac-18] Jacyna I., Klinger D., Pelka J.B., Minikayev R., Dluzewski P., Dynowska E., Jakubowski M., Klepka M.T., Zymierska D., Bartnik A., Kurant Z., Wolska A., Wawro A., Sveklo I., Plaisier J.R., Eichert D., Brigidi F., Makhotkin I., Maziewski A., Sobierajski R. - Study of ultrathin Pt/Co/Pt trilayers modified by nanosecond XUV pulses from laser-driven plasma source Journal of Alloys and Compounds 763, 899-908 (2018)

[Jeh-18] Jehle F., Fratzl P., Harrington M.J. - Metal-tunable self-assembly of hierarchical structure in mussel-inspired peptide films ACS Nano 12, 2160-2168 (2018)

[Jou-18] Jouve A., Nagy G., Somodi F., Tiozzo C., Villa A., Balerna A., Beck A., Evangelisti C., Prati L. - Gold-silver catalysts: Effect of catalyst structure on the selectivity of glycerol oxidation Journal of Catalysis 368, 324-335 (2018)

[Kan-14] Kang M., Bardelli F., Charlet L., Géhin A., Shchukarev A., Chen F., Morel M.C., Ma B., Liu C. - Redox reaction of aqueous selenite with As-rich pyrite from Jiguanshan ore mine (China): Reaction products and pathway Applied Geochemistry 47, 130-140 (2014)

[Kra-14] Krause B., Miljevic B., Aschenbrenner T., Piskorska-Hommel E., Tessarek C., Barchuk M., Buth G., Donfeu Tchana R., Figge S., Gutowski J., Hänschke D., Kalden J., Laurus T., Lazarev S., Magalhães-Paniago R., Sebald K., Wolska A., Hommel D., Falta J., Holý V., Baumbach T. - Influence of a low-temperature capping on the crystalline structure and morphology of InGaN quantum dot structures Journal of Alloys and Compounds 585, 572-579 (2014)

[Lau-14] Laureti S., Brombacher C., Makarov D., Albrecht M., Peddis D., Varvaro G., d'Acapito F. - EXAFS investigation of the role of Cu on the chemical order and lattice distortion in L10 Fe–Pt–Cu thin films Journal of Applied Crystallography 47, 1722-1728 (2014)

[Lea-14] Leardini L., Martucci A., Braschi I., Blasioli S., Quartieri S. - Regeneration of high-silica zeolites after sulfamethoxazole antibiotic adsorption: A combined in situ high-temperature synchrotron X-ray powder diffraction and thermal degradation study Mineralogical Magazine 78, 1141-1159 (2014)

[Lia-18] Liao T.W., Yadav A., Hu K.J., van der Tol J., Cosentino S., d'Acapito F., Palmer R.E., Lenardi C., Ferrando R., Grandjean D., Lievens P. - Unravelling the nucleation mechanism of bimetallic nanoparticles with composition-tunable core–shell arrangement Nanoscale 10, 6684-6694 (2018)

[Liu-18] Liu, S.; Xiao, C.; Du, Z.; Marcelli, A.; Cibin, G.; Baccolo, G.; Zhu, Y.; Puri, A.; Maggi, V.; Xu, W. Iron Speciation in Insoluble Dust from High-Latitude Snow: An X-ray Absorption Spectroscopy Study. Condensed Matter, 3 (2018) 47.

[Liu-19] Liu, S., Xiao, C., Du, Z., Marcelli, A., Cibin, G., Baccolo, G., Zhu, Y., Puri, A., Maggi, V., Xu, W. - Iron Speciation in Insoluble Dust from High-LatitudeSnow: An X-ray Absorption Spectroscopy Study – Condensed Matter 3, 47 (2019).

[Lor-15] Loria R., Meneghini C., Torokhtii K., Tortora L., Pompeo N., Cirillo C., Attanasio C., Silva E. - Robustness of the 0-π transition against compositional and structural ageing in superconductor/ferromagnetic/superconductor heterostructures Physical Review B 92, 184106-1-184106-10 (2015)

[Mar-18] Martinelli, A., Lepore, G. O., Bernardini, F., Giaccherini, A., & Di Benedetto, F.- The puzzling structure of Cu5FeS4 (bornite) at low temperature, Acta Crystallographica Section B: Structural Science, Crystal Engineering and Materials 74.5 (2018).

[Mart-16] Martucci A., Rodeghero E., Cruciani G. - Continuous dehydration of cavansite under dynamic conditions: An in situ synchrotron powder-diffraction study European Journal of Mineralogy 28, 5-13 (2016)

[Mas-14] Massaccesi L., Meneghini C., Comaschi T., D'Amato R., Onofri A., Businelli D. - Ligands involved in Pb immobilization and transport in lettuce, radish, tomato and Italian ryegrass Journal of Plant Nutrition and Soil Science 177, 766-774 (2014)

[Mau-14] Maurizio C., Cesca T., Trapananti A., Kalinic B., Scian C., Mazzoldi P., Battaglin G., Mattei G. - Effect of ultrasmall Au-Ag aggregates formed by ion implantation in Er-implanted silica on the 1.54 µm Er3+ luminescence Nuclear Instruments and Methods in Physics Research B 326, 11-14 (2014)

[Mau-15.1] Maurizio C., Checchetto R., Trapananti A., Rizzo A., Miotello A. - In situ X-ray absorption spectroscopy-X-ray diffraction investigation of Nb-H nanoclusters in MgH2 during hydrogen desorption Journal of Physical Chemistry C 119, 7765-7770 (2015)

[Mau-15] Maurizio C., Cesca T., Kalinic B., Trapananti A., Scian C., Battaglin G., Mazzoldi P., Mattei G. - Gold-based nucleation in implanted silica studied by x-ray absorption spectroscopy Ceramics International 41, 8660-8664 (2015)

[Mau-18.2] Maurizio C., Michieli N., Kalinic B., Mattarello V., Bello V., Wilhelm F., Ollefs K., Mattei G. - Local structure and X-ray magnetic circular dichroism of Au in Au-Co nanoalloys Applied Surface Science 433, 596-601 (2018)

[Mau-18] Maurizio C., Edla R., Michieli N., Orlandi M., Trapananti A., Mattei G., Miotello A. - Two-step growth mechanism of supported Co3O4-based sea-urchin like hierarchical nanostructures Applied Surface Science 439, 876-882 (2018)

[Med-14.1] Medas D., Lattanzi P., Podda F., Meneghini C., Trapananti A., Sprocati A.R., Casu M.A., Musu E., De Giudici G. - The amorphous Zn biomineralization at Naracauli stream, Sardinia: Electron microscopy and X-ray absorption spectroscopy Environmental Science and Pollution Research 21, 6775-6782 (2014)

[Med-14] Medas D., De Giudici G., Podda F., Meneghini C., Lattanzi P. - Apparent energy of hydrated biomineral surface and apparent solubility constant: An investigation of hydrozincite Geochimica et Cosmochimica Acta 140, 349-364 (2014)

[Mil-16] Miller H.A., Lavacchi A., Vizza F., Marelli M., Di Benedetto F., d'Acapito F., Paska Y., Page M., Dekel D.R. - A Pd/C-CeO2 anode catalyst for high-performance platinum-free anion exchange membrane fuel cells Angewandte Chemie International Edition 55, 6004-6007 (2016)

[Min-14] Minguzzi A., Lugaresi O., Achilli E., Locatelli C., Vertova A., Ghigna P., Rondinini S. - Observing the oxidation state turnover in heterogeneous iridium-based water oxidation catalysts Chemical Science 5, 3591-3597 (2014)

[MIn-15] Minguzzi A., Locatelli C., Lugaresi O., Achilli E., Cappelletti G., Scavini M., Coduri M., Masala P., Sacchi B., Vertova A., Ghigna P., Rondinini S. - Easy accommodation of different oxidation states in iridium oxide nanoparticles with different hydration degree as water oxidation electrocatalysts ACS Catalysis 5, 5104-5115 (2015)

[Min-17] Minguzzi A., Naldoni A., Lugaresi O., Achilli E., d'Acapito F., Malara F., Locatelli C., Vertova A., Rondinini S., Ghigna P. - Observation of charge transfer cascades in α-Fe2O3/IrOx photoanodes by operando X-ray absorption spectroscopy Physical Chemistry - Chemical Physics 19, 5715-5720 (2017)

[Miz-17] Mizuguchi Y., Paris E., Wakita T., Jinno G., Puri A., Terashima K., Joseph B., Miura O., Yokoya T., Saini N.L. - Evolution of Eu valence and superconductivity in layered Eu0.5La0.5FBiS2−xSex system Physical Review B 95, 064515-1-064515-6 (2017)

[Moh-14] Mohiddon M.A., Naidu K.L., Krishna M.G., Dalba G., Ahmed S.I., Rocca F. - Chromium oxide as a metal diffusion barrier layer: An x-ray absorption fine structure spectroscopy study Journal of Applied Physics 115, 044315-1-044315-7 (2014)

[Mol-15] Möller M., Urban S., Cop P., Weller T., Ellinghaus R., Kleine-Boymann M., Fiedler C., Sann J., Janek J., Chen L., Klar P.J., Hofmann D.M., Philipps J., Dolcet P., Gross S., Over H., Smarsly B.M. - Synthesis and physicochemical characterization of Ce1-xGdxO2-δ: A case study on the impact of the oxygen storage capacity on the HCl oxidation reaction ChemCatChem 7, 3738-3747 (2015)

[Mon-17] Montegrossi G., Giaccherini A., Berretti E., Di Benedetto F., Innocenti M., d'Acapito F., Lavacchi A. - Computational speciation models: A tool for the interpretation of spectroelectrochemistry for catalytic layers under operative conditions Journal of the Electrochemical Society 164, E3690-E3695 (2017)

[Mor-18] Moretti A., Giuli G., Trapananti A., Passerini S. - Electrochemical and structural investigation of transition metal doped V2O5 sono-aerogel cathodes for lithium metal batteries Solid State Ionics 319, 46-52 (2018)

[Mul-17] Mula G., Printemps T., Licitra C., Sogne E., Gambacorti N., Sestu N., Saba M., Pinna E., Chiriu D., Ricci P.C., Casu A., Quochi F., Mura A., Bongiovanni G., Falqui A. - Doping porous silicon with erbium: Pores filling as a method to limit the Er-clustering effects and increasing its light emission Scientific Reports 7, 5957-1-5957-12 (2017)

[Nie-17] Niedermaier M., Dolcet P., Gheisi A.R., Tippelt G., Lottermoser W., Gross S., Bernardi J., Diwald O. - Stability and local environment of iron in vapor phase grown MgO nanocrystals Journal of Physical Chemistry C 121, 24292-24301 (2017)

[Niu-14] Niu G., Schubert M.A., d'Acapito F., Zoellner M.H., Schroeder T., Boscherini F. - On the local electronic and atomic structure of Ce1−xPrxO2−δ epitaxial films on Si Journal of Applied Physics 116, 123515-1-123515-9 (2014)

[Noe-16] Noé P., Sabbione C., Castellani N., Veux G., Navarro G., Sousa V., Hippert F., d'Acapito F. - Structural change with the resistance drift phenomenon in amorphous GeTe phase change materials' thin films Journal of Physics D 49, 035305-1-035305-6 (2016)

[Ott-17] Ottini R., Tealdi C., Tomasi C., Tredici I.G., Soffientini A., Anselmi-Tamburini U., Ghigna P., Spinolo G. - Feasibility of electron and hole injection in heavily doped strontium barium niobate (SBN50) Sr0.5Ba0.5Nb2O6 for thermoelectric applications Journal of Applied Physics 121, 085104-1-085104-8 (2017)

[Ott-18] Ottini R., Tealdi C., Tomasi C., Tredici I.G., Soffientini A., Burriel R., Palacios E., Castro M., Anselmi-Tamburini U., Ghigna P., Spinolo G. - Local environments and transport properties of heavily doped strontium barium niobates Sr0.5Ba0.5Nb2O6 Journal of Solid State Chemistry 258, 99-107 (2018)

[Pau-16] Paul M.C., Bysakh S., Das S., Dhar A., Pal M., Bhadra S.K., Sahu J.K., Kir'yanov A.V., d'Acapito F. - Recent developments in rare-earths doped nano-engineered glass based optical fibers for high power fiber lasers Transactions of the Indian Ceramic Society 75, 195-208 (2016)

[Pel-17] Pelli Cresi J.S., Spadaro M.C., D'Addato S., Valeri S., Amidani L., Boscherini F., Bertoni G., Deiana D., Luches P. - Contraction, cation oxidation state and size effects in cerium oxide nanoparticles Nanotechnology 28, 495702-1-495702-9 (2017)

[Pet-15] Pethes I., Chahal R., Nazabal V., Prestipino C., Trapananti A., Pantalei C., Beuneu B., Bureau B., Jóvári P. - Short range order in Ge-Ga-Se glasses Journal of Alloys and Compounds 651, 578-584 (2015)

[Pet-18] Pethes I., Chahal R., Nazabal V., Prestipino C., Michalik S., Darpentigny J., Jóvári P. - Chemical order in Ge-Ga-Sb-Se glasses Journal of Non-Crystalline Solids 484, 49-56 (2018).

[Pet-19] Petroselli, C., Moroni, B., Crocchianti, S., Selvaggi, R., Vivani, R., Soggia, F., Grotti, M., d’Acapito, F., Cappelletti, D. - Iron Speciation of Natural and Anthropogenic Dust by Spectroscopic and Chemical Methods. Atmosphere 10, 8 (2019).

[Peth-16] Pethes I., Chahal R., Nazabal V., Prestipino C., Trapananti A., Michalik S., Jóvári P. - Chemical short-range order in selenide and telluride glasses Journal of Physical Chemistry B 120, 9204-9214 (2016)

[Pha-17] Phan T.H.V., Bonnet T., Garambois S., Tisserand D., Bardelli F., Bernier-Latmani R., Charlet L. - Arsenic in shallow aquifers linked to the electrical ground conductivity: The Mekong delta source example Geosciences Research 2, 180-195 (2017)

[Pha-18] Phan, V.T.H., Bardelli, F., Le Pape, P., Couture, R. M., Fernandez-Martinez, A., Tisserand, D., Bernier-Latmani, R., Charlet, L. - Interplay of S and As in Mekong Delta sediments during redox oscillations - Geoscience Frontiers, DOI: 10.1016/j.gsf.2018.03.008 (2018).

[Pha-19] Phan, V. T., Bernier-Latmani, R., Tisserand, D., Bardelli, F., Le Pape, P., Frutschi, M., Gehin, A., Couture, R.M., Charlet, L. - As release under the microbial sulfate reduction during redox oscillations in the upper Mekong delta aquifers, Vietnam: a mechanistic study. Science of the Total Environment 663, 718-730 (2019).

[Pil-16] Pilger F., Testino A., Carino A., Proff C., Kambolis A., Cervellino A., Ludwig C. - Size control of Pt clusters on CeO2 nanoparticles via an incorporation–segregation mechanism and study of segregation kinetics ACS Catalysis 6, 3688-3699 (2016)

[Pir-14] Pirola C., Scavini M., Galli F., Vitali S., Comazzi A., Manenti F., Ghigna P. - Fischer–Tropsch synthesis: EXAFS study of Ru and Pt bimetallic Co based catalysts Fuel 132, 62-70 (2014)

[Pol-15] Pollastri S., d'Acapito F., Trapananti A., Colantoni I., Andreozzi G.B., Gualtieri A.F. - The chemical environment of iron in mineral fibres. A combined X-ray absorption and Mössbauer spectroscopic study Journal of Hazardous Materials 298, 282-293 (2015)

[Pop-18] Popov V.V., Menushenkov A.P., Gaynanov B.R., Ivanov A.A., d'Acapito F., Puri A., Shchetinin I.V., Zheleznyi M.V., Berdnikova M.M., Pisarev A.A., Yastrebtsev A.A., Tsarenko N.A., Arzhatkina L.A., Horozova O.D., Rachenok I.G., Ponkratov K.V. - Formation and evolution of crystal and local structures in nanostructured Ln2Ti2O7 (Ln = Gd–Dy) Journal of Alloys and Compounds 746, 377-390 (2018)

[Por-14] Portale G., Sciortino L., Albonetti C., Giannici F., Martorana A., Bras W., Biscarini F., Longo A. - Influence of metal–support interaction on the surface structure of gold nanoclusters deposited on native SiOx/Si substrates Physical Chemistry - Chemical Physics 16, 6649-6656 (2014)

[Qua-18] Quaretti M., Porchia M., Tisato F., Trapananti A., Aquilanti G., Damjanović M., Marchiò L., Giorgetti M., Tegoni M. - Journal of Inorganic Biochemistry 188, 50-61 (2018)

[Ram-14.1] Ramamoorthy R.K., Bhatnagar A.K., Rocca F., Dalba G., Mattarelli M., Montagna M. - Er3+ local structure and its optical properties in ZnO-PbO tellurite glasses Journal of Non-Crystalline Solids 383, 153-156 (2014)

[Ram-14] Ramamoorthy R.K., Bhatnagar A.K. - Invariant bandwidth of erbium in ZnO-PbO-tellurite glasses: Local probe/model AIP Conference Proceedings 1591, 822-824 (2014)

[Rez-16] Rezvani S.J., Ciambezi M., Gunnella R., Minicucci M., Muñoz M.A., Nobili F., Pasqualini M., Passerini S., Schreiner C., Trapananti A., Witkowska A., Di Cicco A. - Local structure and stability of SEI in graphite and ZFO electrodes probed by as K-edge absorption spectroscopy Journal of Physical Chemistry C 120, 4287-4295 (2016)

[Riz-18] Rizzato S., Moret M., Beghi F., Lo Presti L. - Crystallization and structural properties of a family of isotopological 3D-networks: The case of a 4,4′-bipy ligand–M2+ triflate system CrystEngComm 20, 3784-3795 (2018)

[Ron-16] Rondinini S., Lugaresi O., Achilli E., Locatelli C., Minguzzi A., Vertova A., Ghigna P., Comninellis C. - Fixed energy X-ray absorption voltammetry and extended X-ray absorption fine structure of Ag nanoparticle electrodes Journal of Electroanalytical Chemistry 766, 71-77 (2016)

[Ros-14] Rossi F., Ristori S., Marchettini N., Pantani O.L. - Functionalized clay microparticles as catalysts for chemical oscillators Journal of Physical Chemistry C 118, 24389-24396 (2014)

[Ros-16] Rossi G., d'Acapito F., Amidani L., Boscherini F., Pedio M. - Local environment of metal ions in phthalocyanines: K-edge X-ray absorption spectra Physical Chemistry - Chemical Physics 18, 23686-23694 (2016)

[Sah-14] Sahiner M.A.Bonitz M., Lopez J., Becker K., Thomsen H. - Characterization of local structures in plasma deposited semiconductors by X-ray absorption spectroscopy Complex Plasma Springer Series on Atomic, Optical, and Plasma Physics 82, 299-320 (2014)

[San-16] Sanfilippo D. - One-step hydrogen through water splitting with intrinsic CO2 capture in chemical looping Catalysis Today 272, 58-68 (2016)

[SanA-16] Sanson A. - Displacive phase-transition of cuprite Ag2O revealed by extended x-ray absorption fine structure Journal of Physics and Chemistry of Solids 95, 114-118 (2016)

[Sch-18] Schnohr C.S., Eckner S., Schöppe P., Haubold E., d'Acapito F., Greiner D., Kaufmann C.A. - Reversible correlation between subnanoscale structure and Cu content in co-evaporated Cu(In,Ga)Se2 thin films Acta Materialia 153, 8-14 (2018)

[Sou-15] Souchier E., d'Acapito F., Noé P., Blaise P., Bernard M., Jousseaume V. - The role of the local chemical environment of Ag on the resistive switching mechanism of conductive bridging random access memories Physical Chemistry - Chemical Physics 17, 23931-23937 (2015)

[Sta-16] Stavrinadis A., Pelli Cresi J.S., d'Acapito F., Magén C., Boscherini F., Konstantatos G. - Aliovalent doping in colloidal quantum dots and its manifestation on their optical properties: Surface attachment versus structural incorporation Chemistry of Materials 28, 5384-5393 (2016)

[Sta-17] Stabile P., Giuli G., Cicconi M.R., Paris E., Trapananti A., Behrens H. - The effect of oxygen fugacity and Na/(Na+K) ratio on iron speciation in pantelleritic glasses Journal of Non-Crystalline Solids 478, 65-74 (2017)

[StaP-16] Stabile P. - Pantelleritic magmas: Experimental study on the effect of [Na(Na+K)] and fO2 on iron redox and viscosity Plinius - Italian supplements to European Journal of Mineralogy 42, 101-104 (2016)

[Ste-18] Stellato F., Calandra M., d'Acapito F., De Santis E., La Penna G., Rossi G., Morante S. - Multi-scale theoretical approach to X-ray absorption spectra in disordered systems: an application to the study of Zn(II) in water Physical Chemistry - Chemical Physics 20, 24775-24782 (2018)

[Suc-17] Suchomski C., Weber D.J., Dolcet P., Hofmann A., Voepel P., Yue J., Einert M., Möller M., Werner S., Gross S., Djerdj I., Brezesinski T., Smarsly B.M. - Sustainable and surfactant-free high-throughput synthesis of highly dispersible zirconia nanocrystals Journal of Materials Chemistry A 5, 16296-16306 (2017)

[Tag-14] Taglieri G., Mondelli C., Daniele V., Pusceddu E., Scoccia G. - Synthesis, textural and structural properties of calcium hydroxide nanoparticles in hydro-alcoholic suspension Advances in Materials Physics and Chemistry 4, 50-59 (2014)

[Ted-17] Tedesco C., Brunelli M. - X-ray powder diffraction Reference Module in Chemistry, Molecular Sciences and Chemical Engineering

[Ter-18] Terashima K., Paris E., Simonelli L., Salas-Colera E., Puri A., Wakita T., Yamada Y., Nakano S., Idei H., Kudo K., Nohara M., Muraoka Y., Mizokawa T., Yokoya T., Saini N.L. - Temperature-dependent local structure and superconductivity of BaPd2As2 and SrPd2As2 Physical Review B 98, 94525-1-49525-5 (2018)

[Tis-16] Tisato F., Marzano C., Peruzzo V., Tegoni M., Giorgetti M., Damjanović M., Trapananti A., Bagno A., Santini C., Pellei M., Porchia M., Gandin V. - Insights into the cytotoxic activity of the phosphane copper(I) complex [Cu(thp)4][PF6] Journal of Inorganic Biochemistry 165, 80-91 (2016)

[Tod-17] Todaro M., Sciortino L., Gelardi F.M., Buscarino G. - Determination of geometry arrangement of copper ions in HKUST-1 by XAFS during a prolonged exposure to air Journal of Physical Chemistry C 121, 24853-24860 (2017)

[Tor-15] Torrengo S., Paul M.C., Halder A., Das S., Dhar A., Sahu J.K., Jain S., Kir'yanov A.V., d'Acapito F. - EXAFS studies of the local structure of bismuth centers in multicomponent silica glass based optical fiber preforms Journal of Non-Crystalline Solids 410, 82-87 (2015)

[Urb-16] Urban S., Dolcet P., Möller M., Chen L., Klar P.J., Djerdj I., Gross S., Smarsly B.M., Over H. - Synthesis and full characterization of the phase-pure pyrochlore Ce2Zr2O7 and the κ-Ce2Zr2O8 phases Applied Catalysis B: Environmental 197, 23-34 (2016)

[Vac-16] Vachhani P.S., Sipr O., Bhatnagar A.K., Ramamoorthy R.K., Choudhary R.J., Phase D.M., Dalba G., Kuzmin A., Rocca F. - Local structure and magnetization of ferromagnetic Cu-doped ZnO films: No magnetism at the dopant? Journal of Alloys and Compounds 678, 304-311 (2016)

[Val-17] Valotto G., Cattaruzza E., Bardelli F. - Multi-edge X-ray absorption spectroscopy study of road dust samples from a traffic area of Venice using stoichiometric and environmental references Spectrochimica Acta A 173, 971-978 (2017)

[Van-15] Van T.T.T., Turrell S., Capoen B., Vinh L.Q., Cristini-Robbe O., Bouazaoui M., d'Acapito F., Ferrari M., Ristic D., Lukowiak A., Almeida R., Santos L., Kinowski C. - Erbium-doped tin-silicate sol-gel-derived glass-ceramic thin films: Effect of environment segregation on the Er3+ emission Science of Advanced Materials 7, 301-308 (2015)

[Veb-18] Veber A., Cicconi M.R., Puri A., de Ligny D. - Optical properties and bismuth redox in Bi-doped high-silica Al–Si glasses Journal of Physical Chemistry C 122, 19777-19792 (2018)

[Ven-15] Ventruti G., Della Ventura G., Scordari F., Susta U., Gualtieri A.F. - In situ high-temperature XRD and FTIR investigation of hohmannite, a water-rich Fe-sulfate, and its decomposition products. Journal of Thermal Analysis and Calorimetry 119, 1793-1802 (2015)

[Voe-16] Voepel P., Suchomski C., Hofmann A., Gross S., Dolcet P., Smarsly B.M. - In-depth mesocrystal formation analysis of microwave-assisted synthesis of LiMnPO4 nanostructures in organic solution CrystEngComm 18, 316-327 (2016)

[Wan-15] Wang L., Lavacchi A., Bellini M., d'Acapito F., Di Benedetto F., Innocenti M., Miller H.A., Montegrossi G., Zafferoni C., Vizza F. - Deactivation of palladium electrocatalysts for alcohols oxidation in basic electrolytes Electrochimica Acta 177, 100-106 (2015)

[Wol-17] Wolska A., Sobierajski R., Klinger D., Klepka M.T., Jacyna I., Wawro A., Jakubowski M., Kisielewski J., Kurant Z., Sveklo I., Bartnik A., Maziewski A. - Polarized XAFS study on the ultrathin Pt/Co/Pt trilayers modified with short light pulses Nuclear Instruments and Methods in Physics Research B 411, 112-115 (2017)

[Zha-16] Zhang X., Lourenço-Martins H., Meuret S., Kociak M., Haas B., Rouvière J.L., Jouneau P.H., Bougerol C., Auzelle T., Jalabert D., Biquard X., Gayral B., Daudin B. - InGaN nanowires with high InN molar fraction: Growth, structural and optical properties Nanotechnology 27, 195704-1-195704-10 (2016)

8.2 General Bibliography

[Bel-03] Bellet, D., Gorges, B., Dallery, A., Bernard, P., Pereiro, E. & Baruchel, J. (2003). *J. Appl. Crystallogr.* **36**(2), 366–367.

[Bel-18] Bellotti, G., Butt, A. D., Carminati, M., Fiorini, C., Bombelli, L., Borghi, G., Piemonte, C., Zorzi, N. & Balerna, A. (2018). *IEEE Nucl. Sci.* pp. 1355 – 1364.

[Ben-08] Benzi F, Davoli I, Rovezzi M and d'Acapito F 2008 *Rev. Sci. Instrum.* **79** 103902 URL

http://www.esrf.eu/computing/scientific/CARD/CARD.html

[Dac-03] F. d'Acapito, I. Davoli, P. Ghigna, and S. Mobilio, *Synchrotron Rad.* **10**, 260-264 (2003).

[Dim-14] Dimper, R., Reichert, H., Raimondi, P., Ortiz, L. S., Sette, F. & Susini, J. (2014). ESRF Upgrade Programme Phase II (2015–2022) Technical Design Study, http://www.esrf.fr/Apache_files/Upgrade/ESRF-orange-book.pdf.

[Fil-00] Filipponi, A., Borowski, M., Bowron, D. T., Ansell, S., Cicco, A. D., Panfilis, S. D. & Itie, J. P. (2000). *Rev. Sci. Instrum.* **71**(6), 2422.

[Ish-05] Ishikawa, T., Tamasaku, K. & Yabashi, M. (2005). *Nucl. Instrum. Meth. A*, **547**(1), 42

[Kra-79] Krause, M. O. & Oliver, J. H. (1979). *J. Phys. Chem. Ref. Data*, **8**(2), 329

[LISA-15] Activity report of the Italian CRG beamline at the European synchrotron radiation facility (ESRF) ISSN: 2553-9248, N.3, Dec. 2015.

[LISA-16] Activity report of the Italian CRG beamline at the European synchrotron radiation facility (ESRF) ISSN: 2553-9248, N.4, Dec. 2016.

[LISA-17] Activity report of the Italian CRG beamline at the European synchrotron radiation facility (ESRF) ISSN: 2553-9248, N.5, Apr. 2018.

[LISA-18] Activity report of the Italian CRG beamline at the European synchrotron radiation facility (ESRF) ISSN: 2553-9248, N.6, Dec. 2018.

[LUM-18] LISA Users Manual V4.1. Available at http://www.esrf.eu/files/live/sites/www/files/UsersAndScience/Experiments/CRG/BM08/Users/Manuale%20LISAV4.1.pdf

[Lut-09] Lutzenkirchen-Hecht, D., Wagner, R., Haake, U., Watenphul, A., Frahm, R. (2009). J. Synchrotron Rad. **16**, 264–272.

[Mau-09] C. Maurizio, M. Rovezzi, F. Bardelli, H. G. Pais, and F. D'Acapito, Rev. Sci. Instrum 80, 063904 (2009).

[Oli-77] Olivero, J. & Longbothum, R. (1977). *J. Quant. Spectrosc. Radiat. Transfer*, **17**, 233.

[San-11.1] Sanchez del Rio, M. & Dejus, R. J. (2011). Proc. SPIE, **8141**, 1–5.

[San-11.2] Sanchez del Rio, M., Canestrari, N., Jiang, F. & Cerrina, F. J. Synchrotron Rad. **18**, (2011) 708–716.

9. Appendix 1

Text of the 5 highlight papers.

Contacts

Beamline responsible:	Francesco d'Acapito dacapito@esrf.fr +33 4 7688 2426 , +33 6 8936 4302
Beamline scientists:	Alessandro Puri puri@esrf.fr +33 4 7688 2859
	Giovanni Orazio Lepore lepore@esrf.fr +33 4 7688 2530
Local Contact:	+33 6 8838 6994
Beamline:	+33 4 7688 2085
Laboratory:	+33 4 7688 2743
Skype:	gilda_beamline
Administration:	Fabrizio La Manna lamanna@esrf.fr +33 4 7688 2962
Web page:	http://www.esrf.eu/UsersAndScience/Experiments/CRG/BM08/

Contributors to this special issue

F. d'Acapito, A. Puri, G.O. Lepore (CNR-IOM, Grenoble), A. Balerna (INFN-LNF, Frascati), C. Maurizio (Univ. Padova), A. Minguzzi (Univ. Milano), R. De Donatis (CNR, Genova).